AFIT/GAE/ENY/91D-8

①

FAILURE CHARACTERISTICS OF SCS-6/Ti-24Al-11Nb COMPOSITE WITH A CIRCULAR HOLE AT ROOM AND ELEVATED TEMPERATURES

THESIS

Joseph E. Overbeck, Captain, USAF
AFIT/GAE/ENY/91D-8

Approved for public release; distribution unlimited

REPORT DOCUMENTATION PAGE

Form Approved
OMB No. 0704-0188

1. AGENCY USE ONLY *(Leave blank)*

2. REPORT DATE
December 1991

3. REPORT TYPE AND DATES COVERED
Master's Thesis

4. TITLE AND SUBTITLE
FAILURE CHARACTERISTICS OF SCS-6/Ti-24Al-11Nb
COMPOSITE WITH A CIRCULAR HOLE AT ROOM AND
ELEVATED TEMPERATURES

5. FUNDING NUMBERS

6. AUTHOR(S)
Joseph E. Overbeck, Captain, USAF

7. PERFORMING ORGANIZATION NAME(S) AND ADDRESS(ES)
Air Force Institute of Tecnology
Wright-Patterson AFB, OH 45433-6583

8. PERFORMING ORGANIZATION REPORT NUMBER
AFIT/GAE/ENY/91D-8

9. SPONSORING/MONITORING AGENCY NAME(S) AND ADDRESS(ES)
WL/POTC
Wright-Patterson AFB, OH 45433

10. SPONSORING/MONITORING AGENCY REPORT NUMBER

11. SUPPLEMENTARY NOTES

12a. DISTRIBUTION/AVAILABILITY STATEMENT
Approved for public release;
ditribution unlimited

12b. DISTRIBUTION CODE

13. ABSTRACT *(Maximum 200 words)*

Off-axis loading of eight ply, unidirectional specimens with and without a circular hole determined the ultimate tensile strength of SCS-6/Ti-24Al-11Nb composite at temperatures of 25°C and 650°C and fiber orientations of 0°, 15°, 45°. Longitudinal moduli of the tested orientations compared closely to the rule of mixtures calculated values, and strengths compared closely to those predicted by the Tsai-Wu failure theory. The small diameter hole does not act as a stress concentrator, but merely reduces the material's strength in proportion to area loss. This result differs from those predicted by linear finite element analysis and orthotropic stress concentration theory. Radiography, used to detect damage prior to failure, showed no fiber breakage nor matrix cracking. Microscopic examination of the fracture surfaces indicates a weak fiber/matrix interface bond at both room and elevated temperatures. Brittle fracture of fibers and matrix with little fiber pull out occurs at room temperature, while brittle fiber fracture and ductile matrix fracture with greater fiber pull out occurs at elevated temperatures.

14. SUBJECT TERMS
29 Metal matrix composites; Titanium aluminides; Modulus of elasticity; Tensile strength; Fracture (mechanics)

15. NUMBER OF PAGES
112

16. PRICE CODE

17. SECURITY CLASSIFICATION OF REPORT	18. SECURITY CLASSIFICATION OF THIS PAGE	19. SECURITY CLASSIFICATION OF ABSTRACT	20. LIMITATION OF ABSTRACT
Unclassified	Unclassified	Unclassified	UL

DISCLAIMER NOTICE

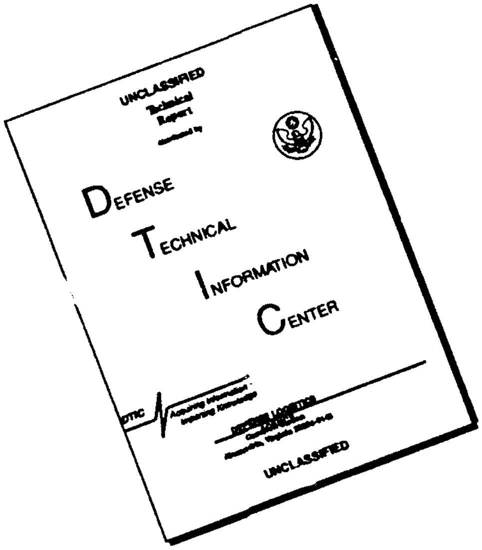

UNCLASSIFIED
Technical
Report

DEFENSE
TECHNICAL
INFORMATION
CENTER

DTIC

UNCLASSIFIED

AFIT/GAE/ENY/91D-8

FAILURE CHARACTERISTICS OF SCS-6/Ti-24Al-11Nb COMPOSITE WITH A CIRCULAR HOLE AT ROOM AND ELEVATED TEMPERATURES

THESIS

Presented to the Faculty of the School of Engineering
of the Air Force Institute of Technology
Air University
In Partial Fulfillment of the
Requirements for the Degree of
Master of Science in Aeronautical Engineering

Joseph E. Overbeck
Captain, USAF

December 1991

Approved for public release; distribution unlimited

Preface

Though this thesis was an individual research effort, it could not have been successfully completed without the additional labor of many people. Dr. Ted Fecke of the Wright Laboratories Materials Directorate sponsored the study and provided the test material. The laboratory technicians, Jay Anderson, Mark Derriso, Andrew Pitts, and Daniel Rioux, helped with everything from strain gauge application through equipment setup to scanning electron microscope operation. Dr. Shankar Mall was especially helpful during test preparations and data analysis. Special thanks goes to Mrs. Rhonda Ryerson for typing this report.

Table of Contents

<u>List of Figures</u>

List of Tables

Abstract

Off-axis loading of eight ply, unidirectional specimens with and without a circular hole determined the ultimate tensile strengths of SCS-6/Ti-24Al-11Nb composite at temperatures of 25°C and 650°C and fiber orientations of 0°, 15°, and 45°. Longitudinal moduli of the tested orientations compared closely to the rule of mixtures calculated values, and strengths compared closely to those predicted by the Tsai-Wu failure theory. The small diameter hole does not act as a stress concentrator, but merely reduces the material's strength in proportion to area loss. This result differs from those predicted by linear finite element analysis and orthotropic stress concentration theory. Radiography, used in an effort to detect damage prior to failure, showed no fiber breakage or matrix cracking. Microscopic examination of the fracture surfaces indicates a weak fiber/matrix interface bond at both room and elevated temperatures. Brittle fracture of fibers and matrix with little fiber pull out occurs at room temperature, while brittle fiber fracture and ductile matrix fracture with greater fiber pull out occurs at elevated temperatures.

FAILURE CHARACTERISTICS OF SCS-6/Ti-24Al-11Nb COMPOSITE WITH A CIRCULAR HOLE AT ROOM AND ELEVATED TEMPERATURES

I. Introduction

The USAF sponsored Integrated High Performance Turbine Engine Technology (IHPTET) program and the National Aerospace Plane (NASP) demand material performance greater than that currently available in conventional aerospace materials. New structural materials are needed if both of these programs are to succeed. A class of composite materials that holds great potential for reaching these high temperature, high performance goals is the metal matrix composite (MMC). Of this general class, titanium aluminide matrix composites appear to be good candidates for fulfilling the requirements of the IHPTET and NASP programs. Titanium aluminides are lightweight, possess good high temperature strength, and show creep and high temperature environmental resistance (Larson, 1991: 363-364).

Previous Studies

Before any new material is put into general use, its properties and suitability for specific applications must be determined. Moduli, tensile strength, fatigue behavior, and creep behavior are necessary for any engineering design.

Larson described the general behavior of silicon carbide fiber reenforced titanium aluminides and compared their properties with available nickel based superalloys (Larson, 1991). Johnson characterized the moduli, strengths, and failure modes of SCS-6/Ti-15V-3Cr in $[0^\circ]_8$, $[90^\circ]_8$, $[0^\circ_2/\pm 45^\circ]_S$, $[0^\circ/90^\circ]_{2S}$, and $[0^\circ/\pm 45^\circ/90^\circ]_S$ layups at room temperature and 482°C (Johnson, 1990). Many studies are dedicated to finding fatigue characteristics of MMC's. Thermal-mechanical fatigue is of particular interest since turbine engine applications would subject any SCS-6/Ti-24Al-11Nb parts to cyclic thermal and mechanical loads (Bartolotta, 1990; Russ, 1991; Kartyna, 1991).

In 1989, Allison Gas Turbine Division of General Motors Corporation completed an extensive study of the SCS-6/Ti-24Al-11Nb MMC. This effort was directed toward the composite manufacturing optimizations made by Textron Speciality Materials and fatigue crack initiation and growth in the composite. Allison tested $[0^\circ]_8$, $[90^\circ]_8$, $[0^\circ/90^\circ]_{2S}$, and $[0^\circ_2/\pm 45^\circ/90^\circ]_S$ layups at selected temperatures between 25°C and 871°C (Gambone 1990a, 1990b).

The Aircraft Engines Division of General Electric has also investigated titanium aluminide composites with emphasis toward manufacturing technologies. Longitudinally and transversely oriented tensile and fatigue tests were conducted using unidirectional composites made from a variety of titanium aluminide matrix alloys and consolidation schemes. Evaluations of these tests are discussed in the GE technical report (General Electric, 1991).

Studies of composites containing holes have been conducted for many years. Greszczuk performed a numerical analysis of unidirectional graphite/epoxy and boron/epoxy composites predicting the effect of anisotropic material properties on the stress concentration around circular holes (Greszczuk, 1972). Whitney performed tests with quasi-isotropic glass/epoxy composites and found that stress concentration theory did not apply to small diameter holes in the material (Whitney, 1974).

More recently, studies have investigated boron/aluminum composites containing holes (Sova, 1978; Johnson, 1983). Fracture processes were examined in these studies. Johnson used radiography to successfully detect fiber breakage and matrix cracking. Interest in titanium aluminide composites has prompted investigations of notch effects in these materials. Naik studied fatigue crack initiation and damage growth in SCS-6/Ti-15V-3Cr specimens that contained circular holes or were edge notched. He concluded that fiber/matrix debonding near the hole reduced the stress concentration factor thus extending the fatigue life of the specimen (Naik, 1989).

Objectives

The Materials Directorate of Wright Laboratories conducts and sponsors ongoing studies of advanced materials for aerospace applications. This investigation of SCS-6/Ti-24Al-11Nb MMC is one such study. Investigation of off-axis loading of unidirectional composite layups provides a more complete characterization of the material. Determining notched behavior is necessary since many designs require holes in load bearing structures for fasteners or interior inspection.

This study investigates the ultimate tensile strengths of unidirectional SCS-6/Ti-24Al-11Nb MMC loaded at various fiber orientations; attempts to find prefailure damage using radiography; and describes the failure mechanism of the material. Three fiber orientations, 0°, 15°, and 45° were tested under uniaxial, tensile loads at 25°C and 650°C. Specimens containing a circular hole were also tested at these fiber orientations and temperatures. Lack of material precluded testing of 90° orientated specimens, however, tensile date of this fiber orientation is available from other sources.

II. Background

Previously developed techniques and methods of analysis were used in the preparation of this report. Those applying directly to this study are reviewed below.

Lamina Material Properties

The apparent stiffness properties of a composite material's lamina are found by following the method discussed by Jones in Mechanics of Composite Materials and summarized here (Jones 1975: 90-96). The mechanics of materials approach to stiffness assumes that strain of a unidirectional composite lamina is the same in both the fiber and matrix. The lamina is assumed to be macroscopically homogeneous, linearly elastic, and initially stress free. In addition, the matrix material and fibers are each assumed to be homogeneous, linearly elastic, and isotropic in their individual compositions.

Using these assumptions, a representative volume element of the composite lamina is generated. This volume element contains a single fiber surrounded by matrix material. The length of the volume element is arbitrary. The width of the volume element is equal to the lamina's fiber spacing. The thickness of the volume element is the lamina's thickness. See Figure 1.

Analysis of the volume element loaded in the longitudinal, transverse, and shear directions determines the rule of mixture expression for E_1, E_2, and G_{12} respectively. The

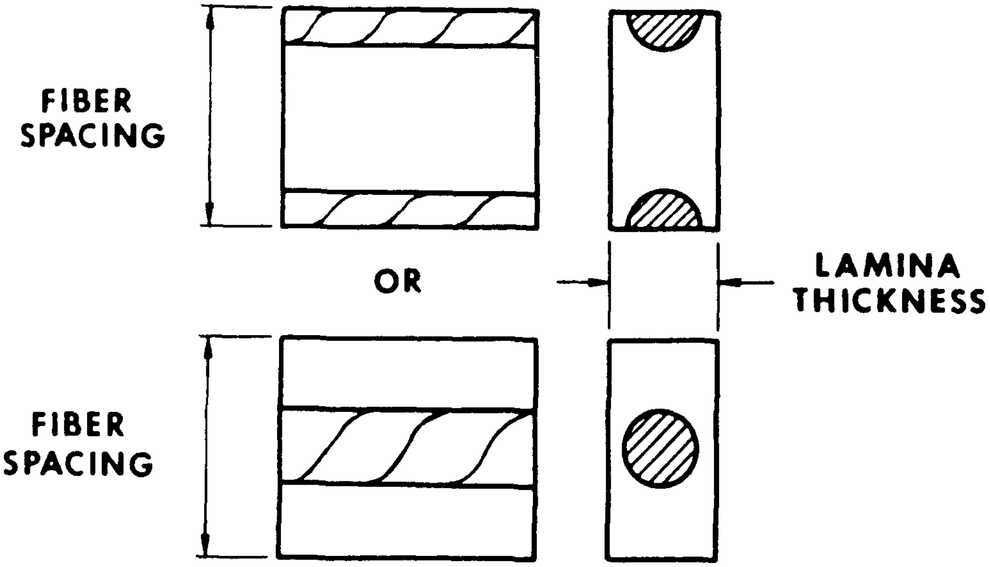

Figure 1. Representative lamina volume element (Jones 1975:88).

apparent longitudinal Young's modulus of a lamina is

$$E_1 = E_f V_f + E_m V_m \tag{1}$$

where

E_f = Young's modulus of the fiber material

E_m = Young's modulus of the matrix material

V_f = volume fraction of fibers in the composite

V_m = volume fraction of matrix in the composite.

The apparent transverse Young's modulus of a lamina is

$$E_2 = \frac{E_f E_m}{V_m E_f + V_f E_m} \qquad \textbf{(2)}$$

using the same values as in equation (1). The in-plane shear modulus of the lamina is

$$G_{12} = \frac{G_m G_f}{V_m G_f + V_f G_m} \qquad \textbf{(3)}$$

where

G_f = shear modulus of the fiber material

G_m = shear modulus of the matrix material.

Finally, the major Poisson's ratio is found by the same argument as E_1 was found. The major Poisson's ratio is

$$\nu_{12} = V_f \nu_f + V_m \nu_m \qquad \textbf{(4)}$$

where

ν_f = Poisson's ratio of the fiber material

ν_m = Poisson's ratio of the matrix material.

Laminate Material Properties

On axis loading. The material used in this study is an eight ply, unidirectional composite. Assuming a perfect bond between the lamina, the composites material properties are the same as those determined for a lamina with equations (1) through (4). The plane stress compliance matrix, $[S_{ij}]$ can be calculated from these engineering constants and used in a single stress-strain relationship (Jones 1975:45-46):

$$\begin{Bmatrix} \epsilon_1 \\ \epsilon_2 \\ \gamma_{12} \end{Bmatrix} = \begin{bmatrix} S_{11} & S_{12} & 0 \\ S_{12} & S_{22} & 0 \\ 0 & 0 & S_{66} \end{bmatrix} \begin{Bmatrix} \sigma_1 \\ \sigma_2 \\ \tau_{12} \end{Bmatrix} \tag{5}$$

where

$$S_{11} = \frac{1}{E_1} \qquad S_{12} = \frac{-\nu_{12}}{E_1}$$
$$S_{22} = \frac{1}{E_2} \qquad S_{66} = \frac{1}{G_{12}} .$$

Off-axis loading. The apparent material properties of an orthotropic material change as an arbitrary axis system is rotated away from the principal axis system. The relation of the two axis systems is shown in Figure 2. In many cases the arbitrary axis system is the one most convenient for the solution of a problem. The set of material properties in the new axis system are found using the following equations (Jones 1975:54):

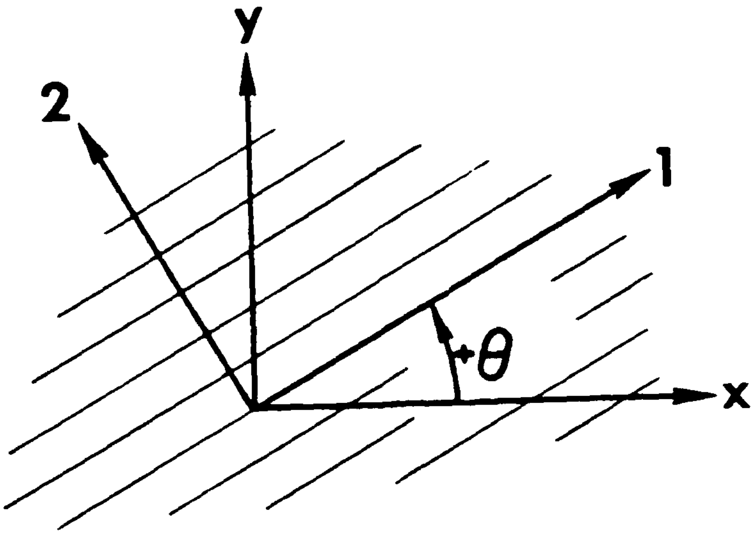

Figure 2. Rotation of principal axis from an arbitrary axis system (Jones 1975:48)

$$E_x = \left[\frac{1}{E_1}\cos^4\theta + \left(\frac{1}{G_{12}} - \frac{2\nu_{12}}{E_1}\right)\sin^2\theta\cos^2\theta + \frac{1}{E_2}\sin^4\theta \right]^{-1} \tag{6}$$

$$E_y = \left[\frac{1}{E_1}\sin^4\theta + \left(\frac{1}{G_{12}} - \frac{2\nu_{12}}{E_1}\right)\sin^2\theta\cos^2\theta + \frac{1}{E_2}\cos^4\theta \right]^{-1} \tag{7}$$

$$G_{xy} = \left[2\left(\frac{2}{E_1} + \frac{2}{E_2} + \frac{4\nu_{12}}{E_1} - \frac{1}{G_{12}}\right)\sin^2\theta\cos^2\theta + \frac{1}{G_{12}}(\sin^4\theta + \cos^4\theta) \right]^{-1} \tag{8}$$

$$\nu_{xy} = E_x \left[\frac{\nu_{12}}{E_1}(\sin^4\theta + \cos^4\theta) - \left(\frac{1}{E_1} + \frac{1}{E_2} - \frac{1}{G_{12}}\right)\sin^2\theta\cos^2\theta \right] \tag{9}$$

$$\eta_{xy,x} = E_x \left[\left(\frac{2}{E_1} + \frac{2\nu_{12}}{E_1} - \frac{1}{G_{12}}\right)\sin\theta\cos^3\theta - \left(\frac{2}{E_2} + \frac{2\nu_{12}}{E_1} - \frac{1}{G_{12}}\right)\sin^3\theta\cos\theta \right] \tag{10}$$

$$\eta_{xy,x} = E_y \left[\left(\frac{2}{E_1} + \frac{2\nu_{12}}{E_1} - \frac{1}{G_{12}} \right) \sin^3\theta \cos\theta - \left(\frac{2}{E_2} + \frac{2\nu_{12}}{E_1} - \frac{1}{G_{12}} \right) \sin\theta \cos^3\theta \right] \qquad (11)$$

E_1, E_2, G_{12}, and ν_{12} are the orthotropic material constants of the principal axis system found by experimentation or by using equations (1) through (4). The angle, θ, is the angle shown in Figure 2. The terms $\eta_{xy,x}$ and $\eta_{xy,y}$ are the coefficients of mutual influence, and they characterize shearing in the xy plane caused by a normal stress in the x and y directions respectively.

An off-axis, plane stress compliance matrix, $[\bar{S}_{ij}]$ can be calculated from these six new engineering constants and used in a single stress-strain relationship for any loading condition (Jones 1975:52-53).

$$\begin{Bmatrix} \epsilon_x \\ \epsilon_y \\ \gamma_{xy} \end{Bmatrix} = \begin{bmatrix} \bar{S}_{11} & \bar{S}_{12} & \bar{S}_{16} \\ \bar{S}_{12} & \bar{S}_{22} & \bar{S}_{26} \\ \bar{S}_{16} & \bar{S}_{26} & \bar{S}_{66} \end{bmatrix} \begin{Bmatrix} \sigma_x \\ \sigma_y \\ \tau_{xy} \end{Bmatrix} \qquad (12)$$

where

$$\begin{aligned} \bar{S}_{11} &= \frac{1}{E_x} & \bar{S}_{16} &= \frac{\eta_{xy,x}}{E_x} \\ \bar{S}_{12} &= \frac{-\nu_{xy}}{E_x} & \bar{S}_{26} &= \frac{\eta_{xy,y}}{E_y} \\ \bar{S}_{22} &= \frac{1}{E_y} & \bar{S}_{66} &= \frac{1}{G_{xy}} \quad . \end{aligned} \qquad (13)$$

Strength and Failure Theory

The ultimate tensile strength (UTS) of various unidirectional fiber orientations was found for this study. These experimental values are compared to predicted failure strengths based upon the strength of the composite in its principal material directions. Close agreement between the experimental and calculated failure strengths permits use of the calculated failure stresses in design problems where the failure strength of the needed fiber orientation had not been experimentally determined.

A failure theory which accounts for interaction between longitudinal, transverse, and shear failure strengths (designated X, Y, and S respectively) is the Tsai-Wu tensor theory. Jones discusses this theory at length in Mechanics of Composite Materials (Jones 1975:80-83). This is an attractive failure theory since it is invariant under rotation of coordinates, it transforms according to tensor transformation laws, and it has symmetry properties similar to the stiffness and compliances.

The three dimensional failure space

$$F_i\sigma_i + F_{ij}\sigma_i\sigma_j = 1 \qquad (14)$$

reduces to

$$F_1\sigma_1 + F_2\sigma_2 + F_6\sigma_6 + F_{11}\sigma_1^2 + F_{22}\sigma_2^2 + F_{66}\sigma_6^2 + 2F_{12}\sigma_1\sigma_2 = 1 \qquad (15)$$

for an orthotropic lamina under plane stress conditions. The various constants are determined as follows:

$$
\begin{aligned}
F_1 &= \frac{1}{X_t} + \frac{1}{X_c} \\
F_{11} &= -\frac{1}{X_t S_c} \\
F_2 &= \frac{1}{Y_t} + \frac{1}{Y_c} \\
F_{22} &= -\frac{1}{Y_t Y_c} \\
F_6 &= 0 \\
F_{66} &= \frac{1}{S^2}
\end{aligned}
\tag{16}
$$

The term F_{12} depends upon both the biaxial tensile failure stress and engineering strengths

$$F_{12} = \frac{1}{2\sigma^2}[1 - (\frac{1}{X_t} + \frac{1}{X_c} + \frac{1}{Y_t} + \frac{1}{Y_c})\sigma + \frac{1}{X_t X_c} + \frac{1}{Y_t Y_c})\sigma^2] \tag{17}$$

The engineering strengths are defined as

X_t = tensile strength in the longitudinal direction

X_c = compressive strength in the longitudinal direction

Y_t = tensile strength in the transverse direction

Y_c = compressive strength in the transverse direction

S = in-plane shear strength.

Two simplifying assumptions will be applied to the Tsai-Wu failure criterion in this study. Since compressive strength data is unavailable, X_c will be assumed equal to $-X_t$. Similarly, Y_c will be assumed equal to $-Y_t$. The second assumption, made in the absence of biaxial failure data, will be that $F_{12} = 0$. Under these assumptions and by substituting the values of equation (14) into equation (13), the Tsai-Wu failure criteria becomes

$$\frac{\sigma_1^2}{X_t^2} + \frac{\sigma_2^2}{Y_t^2} + \frac{\sigma_6^2}{S^2} = 1 \qquad (18)$$

If a uniaxial load, σ_x, is applied at an arbitrary angle θ to the lamina's principal axis then

$$\begin{aligned} \sigma_1 &= \sigma_x \cos^2 \theta \\ \sigma_2 &= \sigma_x \sin^2 \theta \\ \sigma_6 &= -\sigma_x \sin \theta \cos \theta \end{aligned} \qquad (19)$$

Substituting values of equation (19) into equation (18) yields

$$\frac{\cos^4 \theta}{X_t^2} + \frac{\sin^4 \theta}{Y_t^2} + \frac{\sin^2 \theta \cos^2 \theta}{S^2} = \frac{1}{\sigma_x^2} \qquad (20)$$

Stress Concentration Factor

Greszczuk developed a solution determining the circumferential stress at the edge of a circular hole in an anisotropic plate (Greszczuk 1972). This solution also applies to a unidirectional composite plate loaded in a direction other than the principal one. The solution for stress is given by

$$\sigma_{\theta\infty} = \sigma_{\infty}\left\{\frac{(1+\gamma_1)(1+\gamma_2)[1+\gamma_1+\gamma_2-\gamma_1\gamma_2-2\cos 2(\theta-\alpha)]}{[1+\gamma_1^2-2\gamma_1\cos 2(\theta-\alpha)][1+\gamma_2^2-2\gamma_2\cos 2(\theta-\alpha)]}\right. \tag{21}$$

$$\left.-\frac{4[\gamma_1+\gamma_2-(1+\gamma_1\gamma_2)\cos 2(\theta-\alpha)]\sin^2\alpha+4(\gamma_1\gamma_2-1)\sin 2(\theta-\alpha)\sin\alpha\cos\alpha}{[1+\gamma_1^2-2\gamma_1\cos 2(\theta-\alpha)][1+\gamma_2^2-2\gamma_2\cos 2(\theta-\alpha]}\right\}$$

The parameters γ_1 and γ_2 are defined

$$\gamma_1 = \frac{\left[\frac{E_2}{2G_{12}}-\nu_{12}+\sqrt{\left(\frac{E_2}{2G_{12}}-\nu_{12}\right)^2-\frac{E_2}{E_1}}\right]^{1/2}-1}{\left[\frac{E^2}{2G_{12}}-\nu_{12}+\sqrt{\left(\frac{E_2}{2G_{12}}-\nu_{12}\right)-\frac{E_2}{E_1}}\right]^{1/2}+1} \tag{22}$$

$$\gamma_2 = \frac{\left[\frac{E_2}{2G_{12}}-\nu_{12}-\sqrt{\left(\frac{E_2}{2G_{12}}-\nu_{12}\right)^2-\frac{E_2}{E_1}}\right]^{1/2}-1}{\left[\frac{E^2}{2G_{12}}-\nu_{12}-\sqrt{\left(\frac{E_2}{2G_{12}}-\nu_{12}\right)^2-\frac{E_2}{E_1}}\right]^{1/2}+1}$$

The angle α is the orientation of the fibers to the loading axis, and θ is the angle between the loading axis and the point of interest on the edge of the hole.

The stress concentration factor, K_T^{∞}, is calculated

$$K_T^{\infty} = \frac{\sigma_{\theta\alpha}}{\sigma_{\alpha}} \tag{23}$$

where $\sigma_{\theta\alpha}$ is evaluated at $\theta = 90°$. The Greszczuk stress concentration factor is

$$K_T^{\infty} = \left\{ \frac{(1+\gamma_1)\ (1+\gamma_2)\ [1+\gamma_1+\gamma_2-\gamma_1\gamma_2+2\ \cos\ 2\alpha]}{[1+\gamma_1^2+2\gamma_1\ \cos\ 2\alpha]\ [1+\gamma_2^2+2\gamma_2\ \cos\ 2\alpha]} \right. \tag{24}$$

$$\left. - \frac{4\ [\gamma_1+\gamma_2+(1+\gamma_1\gamma_2)\cos 2\alpha]\ \sin^2\alpha+4\ (\gamma_1\gamma_2-1)\ \sin 2\alpha \sin\alpha\ \cos\alpha}{[1+\gamma_1^2+2\gamma_1\ \cos 2\alpha]\ [1+\gamma_2^2+2\gamma_2\ \cos 2\alpha]} \right\}$$

Tan developed a less complicated formula for the stress concentration factor in an orthotropic plate containing an elliptical hole that produces results similar to Greszczuk's equations (Tan 1987). Tan related stress concentration to the off-axis material constants

$$K_T^{\infty} = 1 + \frac{1}{\lambda}\sqrt{2\left(\sqrt{\frac{E_y}{E_x}} - \nu_{xy}\right) + \frac{E_y}{G_{xy}}}\ . \tag{25}$$

For a circular hole $\lambda = 1$.

Tan also developed a correction to the stress concentration factor for a plate of finite width (Tan 1988). The ratio of infinite width stress concentration factor to finite width stress concentration factor is

$$\frac{K_T^\infty}{K_T} = [2 - (2a/W)^2 - (2a/W)^4]/2 + (2a/W)^6 (K_t^\infty - 3)[1 - (2a/W)^2]/2 \qquad (26)$$

where

2a = diameter of the hole

W = width of the plate.

III. Experimental Equipment and Procedure

Mechanical tests performed for this investigation were all uniaxial tensile tests of notched and unnotched specimens done in laboratory air at constant temperature. Testing was conducted in the materials testing laboratory of the Aeronautical Laboratories, School of Engineering, Air Force Institute of Technology. Nondestructive evaluations of test specimens were completed using the facilities of the Materials Directorate, Wright Laboratory, located at Wright-Patterson AFB, Ohio.

Test Equipment

The test equipment consisted of the following major components:

1) Material Testing System (MTS) Series 810 490 kN servohydraulic machine;

2) MTS 458 Microprofiler controller and data display;

3) MTS Model 632.11B extensometer;

4) Measurements Group 2310 signal conditioning amplifiers;

5) QuaTech analog to digital conversion board;

6) Zenith Z-248 personal computer;

7) Fixed position ten-power microscope.

Additional equipment used for the elevated temperature testing included:

1) Optra Laser Extensometer 3000;

2) Micricon 82300 temperature control system;

3) Two locally manufactured quartz lamp heaters;

4) Cooling water system.

The complete test system consisted of the mechanical loading device, strain measurement equipment, a magnified optical system for subjective visual observations, and a temperature control system for the elevated temperature tests. The cooling water system prevented overheating of the MTS 810 machine's grips and quartz lamp housings. The personal computer used a data acquisition program to record strain and load as a function of time.

Test Specimen Preparation

All tensile test specimens were cut from two identical eight-ply, unidirectional plates of SCS-6/Ti-24Al-11Nb manufactured by Textron-Speciality Materials Division. The plates consist of 35% volume fraction SCS-6 silicon carbide fiber woven with molybdenum wire to maintain fiber spacing and straightness, and 65% volume fraction Ti-24Al-11Nb (atomic percentage) cross-rolled foil. The eight plies of the composite plates were consolidated by the hot isostatic pressing method developed by Textron and then aged to relieve some of the consolidation induced mechanical stresses. The sample plates' dimensions were nominally 175 mm x 175 mm x 2 mm.

Prior to cutting any test specimens, the sample plates were inspected for defects using ultrasonic (C-scan) and X-ray techniques. Figure 3 clearly shows the fibers in the consolidated matrix. The thin lines running perpendicular to the fibers are the molybdenum cross-weave wires. Neither method discovered defects that would affect testing.

After completing the NDI, twenty-four tensile specimens were cut from the two plates with a diamond wheel saw. The sets of eight $[15^\circ]_8$ and $[45^\circ]_8$ specimens were cut

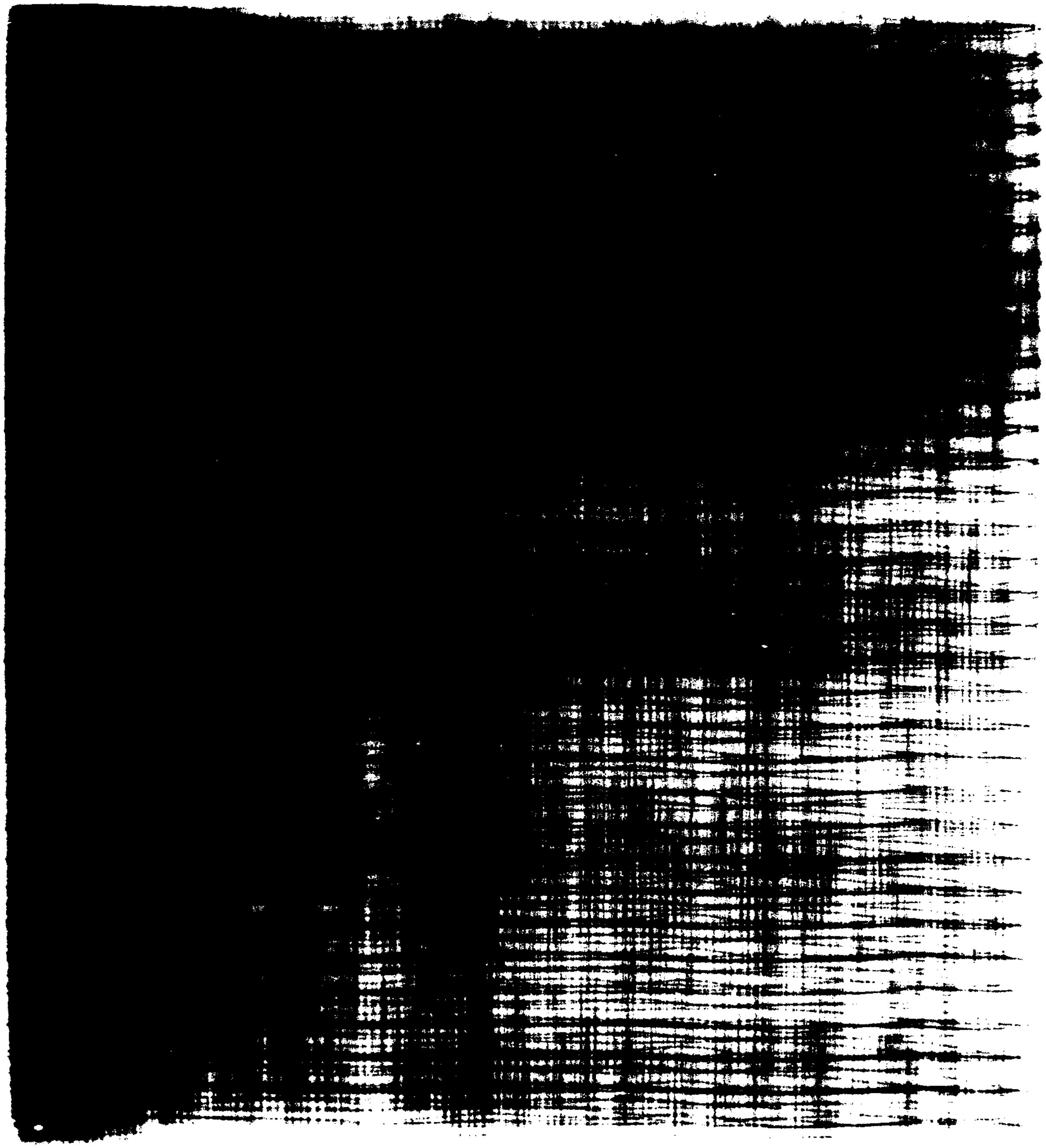

Figure 3. Radiograph of SCS-6/Ti-24Al-11Nb sample plate.

from separate plates while half the set of eight $[0^{\circ}]_8$ specimens was cut from each plate. This cutting plan maximized the number of available test specimens. Twelve specimens for the notched tests were cut 152 mm long and 12.7 mm wide. Twelve specimens for the unnotched tests were cut 95 mm long and 6.4 mm wide. The cut edges were sanded smooth and required no further finishing.

A centrally located hole, 2.54 mm in diameter, was ultrasonically drilled through each of the larger test specimens. Prior to drilling, the specimens were sandwiched between plates of glass to prevent spalling of the outer matrix layer when the drill exited the specimen. This technique combined with the ultrasonic drill forms very clean holes. Fibers are not torn nor pulled from the matrix, the specimen faces are burr-free, and the hole surface polished. Figure 4 is an overall view of the drilled hole, and Figure 5 shows the hole surface.

Kevlar tabs, 25 mm long and 2 mm thick, were epoxied to the ends of each room temperature specimen. See Figure 6. For the high temperature test specimens, titanium tabs were used. These titanium tabs were bead welded to the specimen along the edges and end. See Figure 7. The tabs prevented specimen damage caused by the coarse teeth of the servohydraulic machine's grips.

Test Procedures

The procedures followed during room temperature and elevated temperature testing were similar in tensile loading rate and placement of strain-measuring devices. These efforts produced consistent results between individual tests and tests conducted at different temperatures. Table 1 summarizes the tests conducted for this study.

Figure 4. Centrally located hole in test specimen.

Figure 5. View of hole's inner surface.

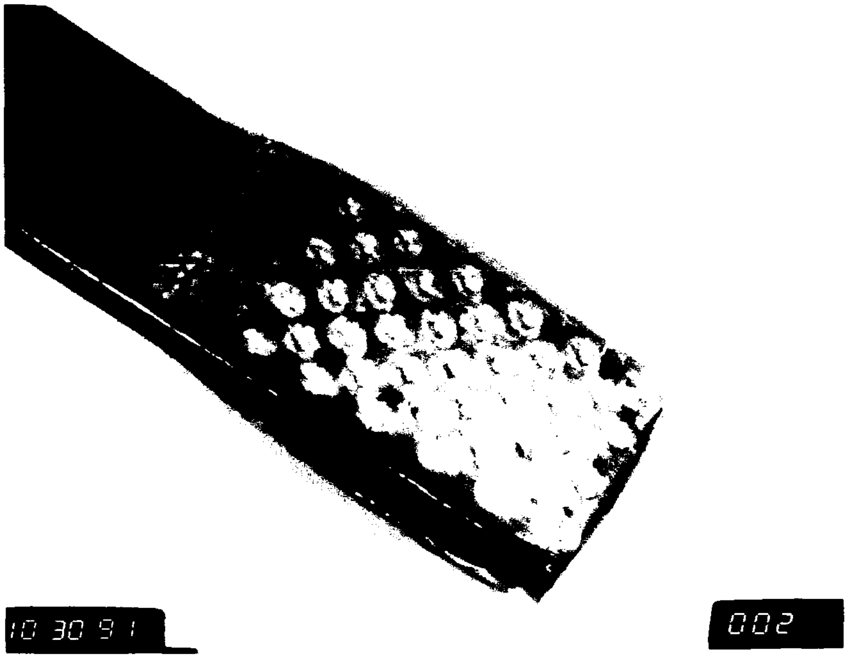

Figure 6. Kevlar tabs attached to specimen end.

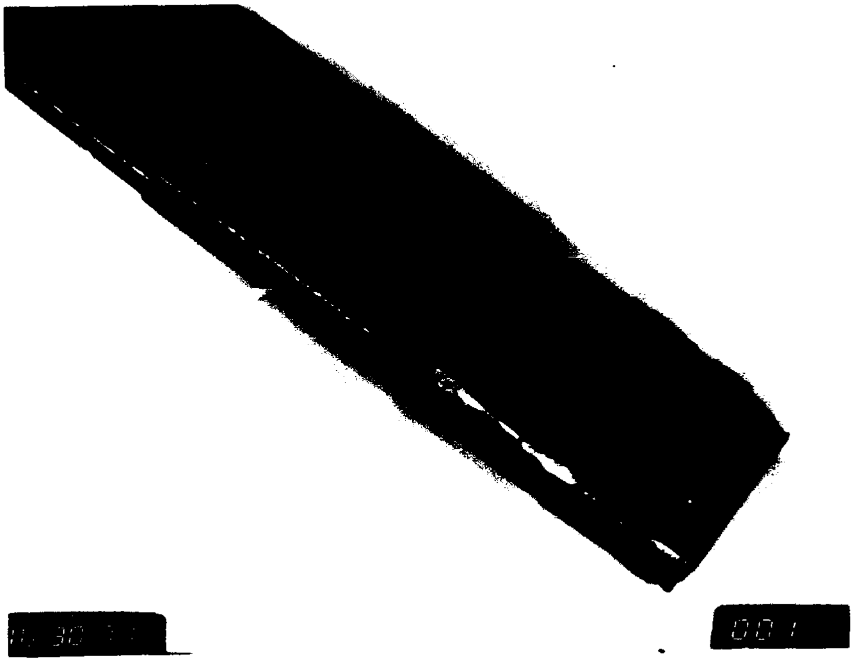

Figure 7. Titanium tabs welded to specimen end.

Specimen Layup	Temperature	With Hole	Tensile Loading
$[0°]_8$	25°C	no	S
$[15°]_8$	25°C	no	S
$[45°]_8$	25°C	no	S
$[0°]_8$	25°C	yes	S,I
$[15°]_8$	25°C	yes	S,I
$[45°]_8$	25°C	yes	S,I
$[0°]_8$	650°C	no	S
$[15°]_8$	650°C	no	S
$[45°]_8$	650°C	no	S
$[0°]_8$	650°C	yes	S
$[15°]_8$	650°C	yes	S
$[45°]_8$	650°C	yes	S

S = single loading to failure
I = incremental loading to failure

Table 1. Test matrix.

Room Temperature Testing. Room temperature tests were conducted in laboratory air at 25°C. Each test specimen was loaded into the servohydraulic machine's grips using a level to ensure that its longitudinal axis was parallel to the machine's loading direction. A clip on extensometer was attached to the notched specimens so the hole was centered in the 25.4 mm gauge length, and a strain gauge was attached to the specimen away from the hole. A second strain gauge was attached very close to the hole in an effort to detect the high localized stresses. A suitable placement technique could not be found for the few tests of this study. Data collected from this strain gauge was erratic and therefore rejected as unreliable. This setup is shown in Figure 8. A single strain gauge was attached to the unnotched specimens prior to testing.

The MTS microprofiler was programmed to apply a monotonically increasing load of 17.8 N/sec. On the large specimens this was a stress rate of 0.070 MPa/sec, and on the smaller specimens was a stress rate of 0.14MPa/sec. The slow loading rate allowed an opportunity to visually observe and record any damage occurring to the specimen. All the unnotched specimens were loaded to failure. The first notched specimen of each fiber orientation was also loaded to failure, while being observed for damage. Load and strain data were recorded by the Zenith personal computer during each test.

The second notched specimen of each fiber orientation was incrementally loaded to the finite element model load that predicted yielding, then to the first point of nonlinearity measured by the extensometer in the previous test, then 95% of the notched UTS, then 99% of the notched UTS, and finally to failure. When each of these loads (except the last) was reached, diiodomethane, a pentrant dye visible to X-rays, was applied inside the hole and to the specimen surface. The specimen was then removed from the test machine and X-rayed to detect any fiber or matrix damage that may have developed. The radiographs were produced by a Phillips 160 kVP industrial X-ray unit with the voltage set at 75 kV and exposing the specimens at 5 mA for 4 minutes. Load and strain data were recorded by the personal computer during each of the incremental loadings.

Elevated Temperature Testing. Gripping the test specimen for the elevated temperature test was done as it was for the room temperature tests. A single type K thermocouple was attached to each face of specimen. In the case of the notched

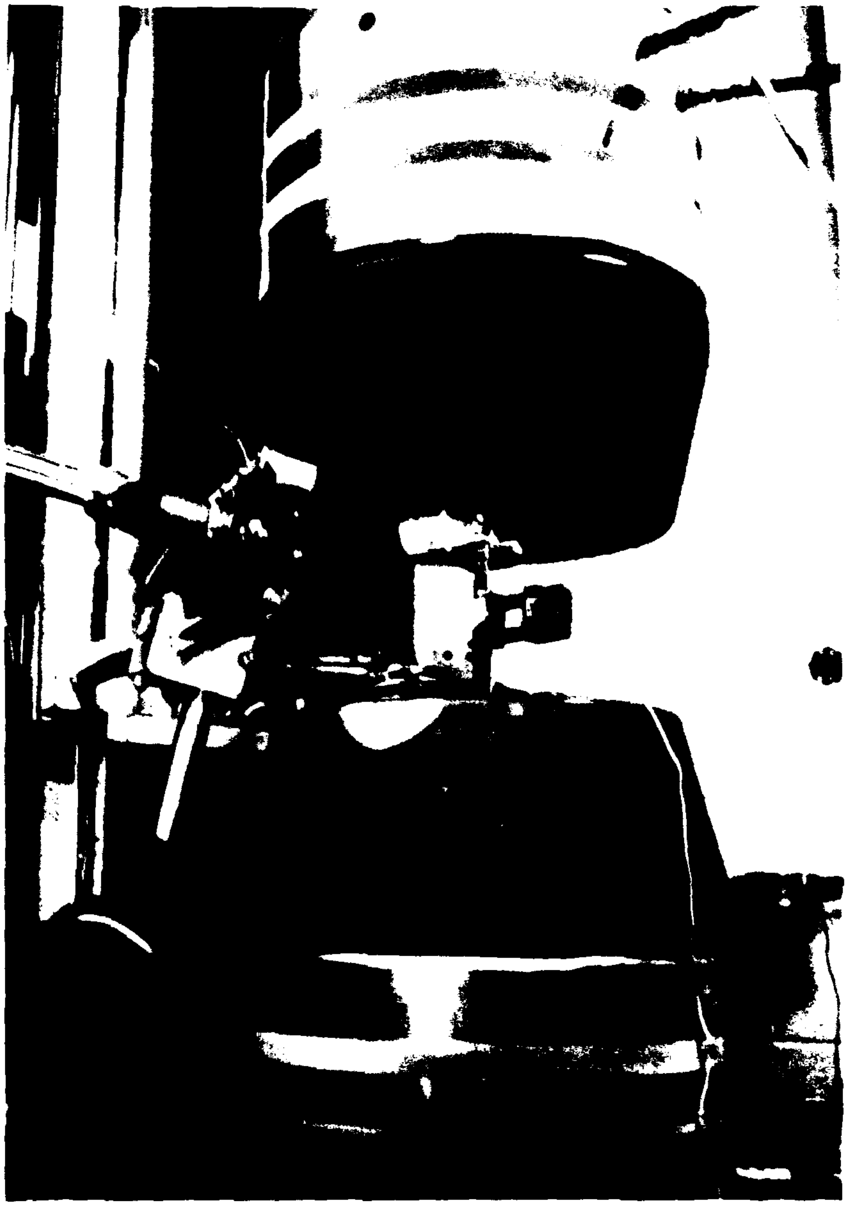

Figure 8. Room temperature test setup.

specimens, the thermocouples were also placed on opposite sides of the hole. These thermocouples provided feedback to the Micricon temperature controller driving the quartz lamps that heated each side of the test specimen. The Optra laser extensometer was mounted to a platform attached to the servohydraulic test machine so the hole of the notched specimens was centered in the 25.4 mm gauge length. Figure 9 shows this elevated temperature setup. Because of their small size, the unnotched specimens were tested to failure on a 98 kN MTS servohydraulic machine. A 12.7 mm gauge length, quartz rod extensometer measured strain. Figure 10 illustrates this setup. One heating lamp has been removed to show the specimen.

A standard heating profile was followed for each of the tests. Each specimen was heated from room temperature to 650°C in five minutes and then held at 650°C for the remainder of the test. No mechanical load was applied while the specimen was heated to 650°C. After a five-minute thermal stabilization period at 650°C, the test specimen was loaded to failure. The loading rate used for room temperature testing was also used in this series of tests. The Zenith personal computer recorded load and strain data during each test.

Close visual inspection of the test specimen for damage was not possible because of the short distance between the heater lamps and the specimen's surface. Incremental loading was not perfomed to avoid any effects of thermal cycling. X-ray inspection of these elevated temperature specimens was not attempted since facilities for high temperature NDI were unavailable.

Figure 9. Elevated temperature test setup.

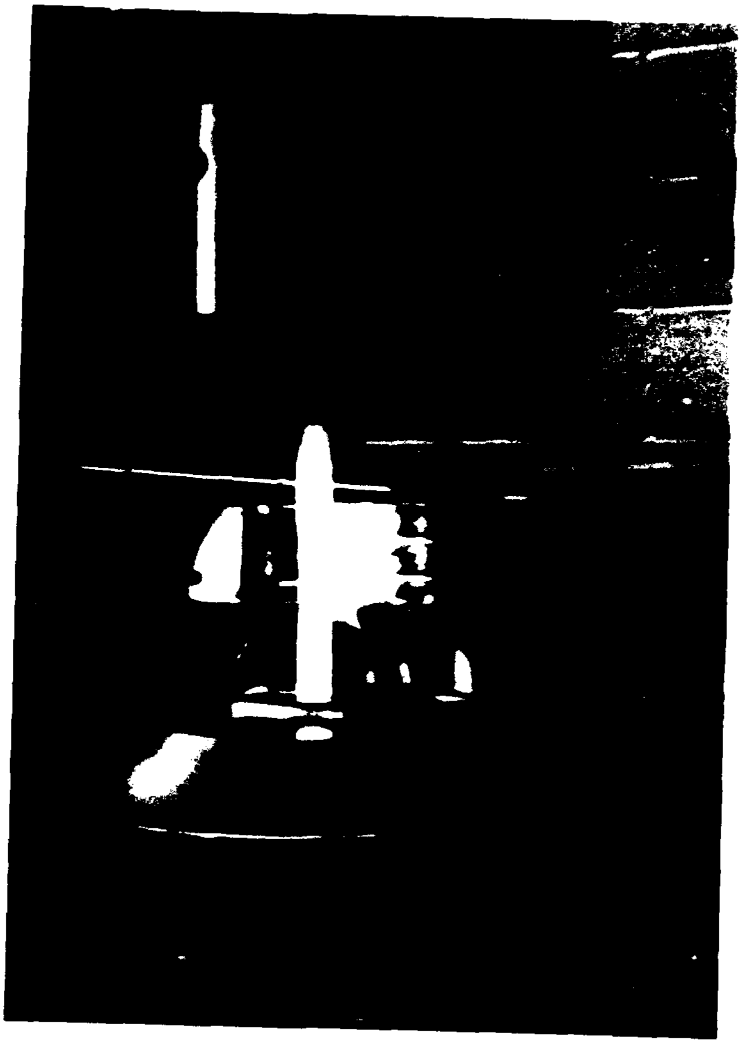

Figure 10. Small specimen, elevated temperature test setup.

IV. Finite Element Model

A finite element model of the notched test specimen was developed as an analytical tool for this study. SDRC I-DEAS V, computer-aided design program, was used to construct the finite element model and produce the graphic outputs in this study. MSC/NASTRAN version 66A analyzed the linear static problems input form I-DEAS. (Version 66A of NASTRAN does not have the capability to perform nonlinear analysis of orthotropic materials.)

A state of plane stress was assumed for this study since the test specimen is thin compared to its length and width. Taking advance of this assumption, the finite element model was built with thin shell (two dimensional) elements. In addition, the two-component, eight-ply composite of the test specimen was treated as a monolithic, homogeneous, orthotropic material in the model. Plate thickness is required for stress calculations, so an average specimen thickness of 2 mm was applied to each model.

Model Development

The model was drawn and its mesh refined by treating it as a thin plate made of an isotropic material. An exact solution for stress at the edge of a circular hole exists for this case. Two points were chosen to quickly verify the accuracy of the model and its solutions. The first point was at the edge of the hole 30° from the loading axis. The circumferential stress, $\sigma_{\theta\theta}$, at this point is zero. (Dally 1978:81). The second point was at the edge of the hole 90° from the loading axis. Here $\sigma_{\theta\theta}$ is 3.14 times the applied stress, that is, the stress concentration factor, K_T, is 3.14 for a d/W ratio of 0.2.

(Peterson 1974:150). With a uniformly applied edge stress of 207 MPa, the stresses at points one and two are 0 MPa and 649.5 MPa respectively.

With this in mind, a quarter plate, symmetrically restrained coarse mesh model was constructed of linear, thin-shell elements following the example problem of MSC/NASTRAN handbook (MSC/NASTRAN 1985:6.6138D-1-3). MSC/NASTRAN analysis showed this mesh to be far too coarse for the dimensions of this model. The MSC/NASTRAN solution was more than 25% smaller than the exact solution at point two.

Whitney gives a clue for explaining this large error. Figure 11 shows the change in stress gradient as the size of the hole decreases (Whitney 1974:253). A coarse mesh masks this rapid decrease in stress by computing an element's strain energy over a wide area of the model. Refining the mesh increased the number of elements along the quarter circle edge of the hole to ten from five and limited the element's width to one tenth of the hole radius. Now the MSC/NASTRAN solution, 646.7 MPa, was within 1% of the exact solution at point two.

This refined quarter plate model was expanded to a complete model of the test specimen. The same element size and distribution was carried over to the new model. MSC/NASTRAN computed $\sigma_{\theta\theta}$ at point two as 624.0 MPa, a -3.5% error, and it computed $\sigma_{\theta\theta}$ at point one as 2.0 MPa (a negligible value compared to the applied stress).

Orthotropic Plate Model

The final refined model, with applied loads (right end) and restraints (left end), used for analysis is shown in Figure 12. The region near the hole is magnified in

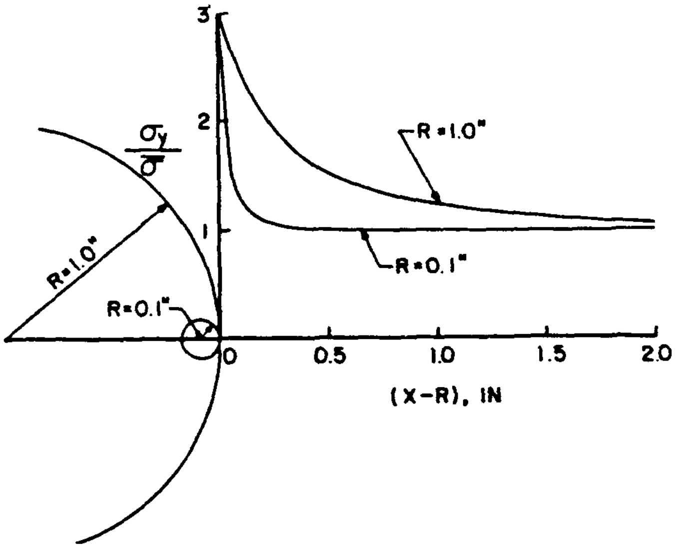

Figure 11. Stress distribution for a hole in an infinite isotropic plate.

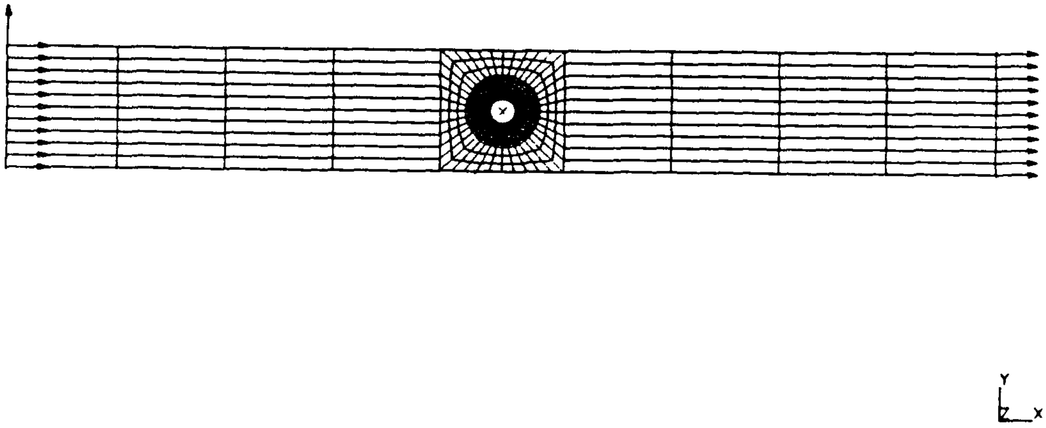

Figure 12. Finite element model for analysis.

Figure 13 to show the element arrangement and nodal numbering. In all, the refined mesh consists of 800 elements connecting 848 grid points with 5069 total degrees of freedom.

The Allison experimentally determined material properties E_1, E_2, and G_{12} and the rule of mixtures calculated ν_{12} were used as the orthotropic material properties for the finite element model of the $[0°]_8$ specimen layup (Gambone 1990b:12). Transforming these values with equations 6 through 9 produces the orthotropic material properties used for the models of the $[15°]_8$ and $[45°]_8$ specimen layups. In all, six sets of material properties were used to model the various specimen layups and test temperatures, and these values are summarized in Table 2.

The load applied to the finite element model for calculations was varied with each fiber orientation and temperature, as shown in Table 3, so that the maximum MSC/NASTRAN calculated stress was approximately equal to each specimen's yieldstress.

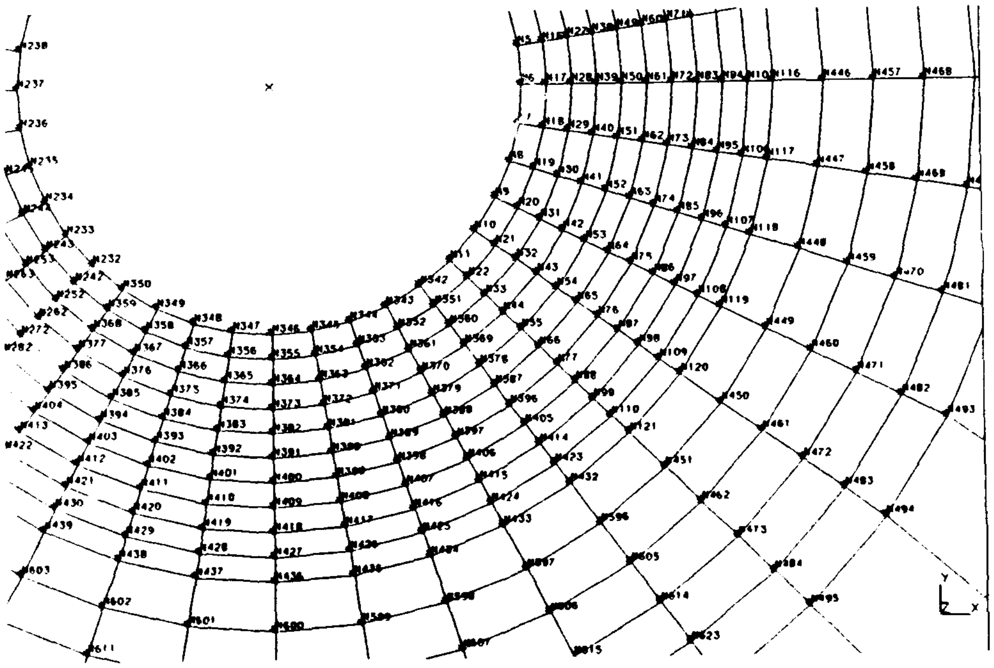

Figure 13. Nodal numbering near hole.

Specimen Layup	Room Temp 25°C	Elevated Temp 650°C
$[0°]_8$	E_1 = 182.3 GPa E_2 = 118.6 GPa G_{12} = 32.8 GPa ν_{12} = 0.272	E_1 = 156.3 GPa E_2 = 67.3 GPa G_{12} = 19.5 GPa ν_{12} = 0.272
$[15°]_8$	E_x = 153.1 GPa E_y = 110.3 GPa G_{xy} = 37.0 GPa ν_{xy} = 0.358	E_x = 113.8 GPa E_y = 62.7 GPa G_{xy} = 22.4 GPa ν_{xy} = 0.386
$[45°]_8$	E_x = 96.6 GPa E_y = 96.6 GPa G_{xy} = 59.1 GPa ν_{xy} = 0.472	E_x = 57.9 GPa E_y = 57.9 GPa G_{xy} = 40.5 GPa ν_{xy} = 0.485

Table 2. Material properties applied to finite element model.

Fiber Orientation	Room Temperature Load/Node	Elevated Temperature Load/Node
0°	658 N	560 N
15°	489 N	240 N
45°	231 N	62 N

Table 3. Loads applied to finite element model.

V. Results and Discussion

Material Properties

The SCS-6/Ti-24Al-11Nb composite has been studied in developmental strength investigations, creep investigations, and fatigue investigations. Each of the investigations has produced a summary of material properties relating to its area of interest. These material properties are typically aligned with the principal axes of unidirectional layups but can be transformed by equations (6) through (9) to give the apparent properties of various fiber orientations. This study investigated off-axis loading of unidirectional SCS-6/Ti-24Al-11Nb, thus a direct comparison of the experimental Young's modulus, E_x, and the predicted values is possible. Table 4 summarizes the Young's modulus and Poisson's ratio values for the fiber and matrix used in the rule of mixture calculations.

	Room Temp 25°C	Elevated Temp 650°C
SCS6 Fiber	$E = 414$ GPa $\nu = 0.22$	$E = 414$ GPa $\nu = 0.22$
Ti-24Al-11Nb Matrix	$E = 84.1$ GPa $\nu = 0.30$	$E = 48.1$ GPa $\nu = 0.30$

Table 4. Fiber and matrix material properties (Coker 1991).

These values were combined using the rule of mixture equations (1) through (4) to produce the apparent orthotropic material properties for a lamina. Since the eight-ply laminate of this study is a unidirectional one, the lamina material constants are also the laminate material constants. Table 5 summarizes the orthotropic material constants calculated by the rule of mixtures.

	Room Temp 25°C	Elevated Temp 650°C
E_1	199.6 GPa	176.2 GPa
E_2	116.6 GPa	69.6 GPa
G_{12}	45.1 GPa	26.9 GPa
ν_{12}	0.272	0.272

Table 5. Rule of mixtures orthotropic material constants.

Allison conducted extensive tensile tests of eight ply SCS-6/Ti-24Al-11Nb composite during the material's initial development phase. The longitudinal and transverse Young's moduli are reported directly, while the shear modulus could be calculated from data presented for the quasi-isotropic layup, $[0°/\pm45°/90°]_S$. The major Poisson's ratio, ν_{12}, was not reported. Table 6 summarizes the Allison experimental data.

The tensile tests performed for this study provide direct experimental data for the off-axis Young's modulus, E_x, of the $[15°]_8$ and $[45°]_8$ layups and another set of experimental data for the $[0°]_8$ layups. The modulus, E_x, was taken from the stress-strain curve of the unnotched tensile specimen. These moduli are compared to the E_x values calculated by transforming the rule of mixtures data and Allison experimental data in Table 7.

	Room Temp 25°C	Elevated Temp 650°C
E_1	182.3 GPa	156.3 GPa
E_2	118.6 GPa	67.3 GPa
G_{12}	32.8 GPa	19.5 GPa

Table 6. Allison experimental orthotropic material constants (Gambone 1990b:8-9).

	Room Temp (25°C) Modulus -- GPa			Elevated Temp (650°C) Modulus -- GPa		
	$[0°]_8$	$[15°]_8$	$[45°]_8$	$[0°]_8$	$[15°]_8$	$[45°]_8$
Rule of mixtures (transformed)	199.6	178.1	121.1	176.2	140.1	73.9
Allison experimental (transformed)	182.3	153.1	96.6	156.3	113.8	57.9
present experiment	186.0	143.0	112.0	172.0	111.0	54.6

Table 7. Young's modulus, E_x, comparison.

The direct experimental moduli compare closely to the moduli of the transformed Allison experimental data. The differences between the experimental moduli values and the rule of mixtures values are approximately the same at each fiber orientation, with the experimental values about 10% less than the theoretical ones. At elevated temperature, the differences between the experimental moduli and rule of mixtures moduli is larger, approaching 20%. These differences most probably arise due to the assumptions made for the rule of mixture calculations. The assumptions cannot be strictly enforced throughout a manufacturing process, and they greatly simplify the actual behavior of the composite. The rule of mixtures value does serve as an upper bound for the material's stiffness. The close comparison of predicted and experimental values demonstrates a consistent, reliable composite consolidation process used by Textron.

Tensile Strength

The ultimate tensile strength of a unidirectional composite material is very dependent on fiber orientation. Typically, a unidirectional composite exhibits the greatest strength and stiffness when loaded parallel to the fibers. Both strength and stiffness decrease rapidly toward their transverse values as the angle between the fibers and the loading axis increases. The SCS-6/Ti-24Al-11Nb MMC system follows this pattern.

Unnotched Tensile Strength. The room temperature ultimate tensile strength of SCS-6/Ti-24Al-11Nb varies from a maximum of 1185 MPa for the $[0°]_8$ layup to 225 MPa for the $[90°]_8$ layup. The elevated temperature ultimate tensile strength varied from 928 MPa for the $[0°]_8$ layup to 126 MPa for the $[90°]_8$ layup. These results are shown graphically in Figure 14.

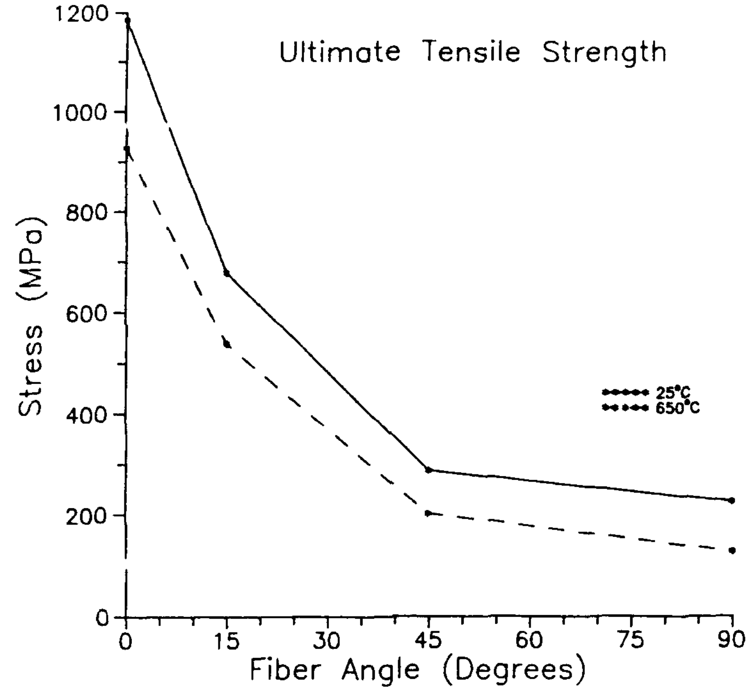

Figure 14. Tensile strength of SCS-6/Ti-24Al-11Nb.

The Tsai-Wu failure theory was applied to the material by computing an ultimate tensile strength curve with equation (20). The strength values used in this computation are listed in Table 8. The longitudinal strength, X_t, is the one found during this investigation. The transverse strength, Y_t, is taken from the Allison study (Gambone 1990b:8), since the $[90°]_8$ layup was not tested for this study. The in-plane shear strength, S, is the shear strength of the matrix alone (Gambone 1990a:12), since shear tests of the composite have not been conducted. Choosing this value for S assumed the shear strength of the fiber/matrix interface is greater than or equal to the shear strength of the matrix alone.

A comparison of the experimental strength curves and the strength curves

	Room Temp 25°C	Elevated Temp 650°C
X_t	1185 MPa	928 MPa
Y_t	225 MPa	126 MPa
S	225 MPa	182 MPa

Table 8. Principal strengths for Tsai-Wu failure theory.

generated by the Tsai-Wu failure theory is shown in Figure 15 and Figure 16. The experimental failure strengths closely match the theoretical failure strengths at both room and elevated temperatures. The small variations between the theoretical and experimental curves might be diminished by accurately measuring the shear strength of the composite and by determining the value of the Tsai-Wu interactive term, F_{12}.

Notched Tensile Strength. The failure strengths of the notched and unnotched SCS-6/Ti-24Al-11Nb at room temperature and at elevated temperature are plotted against fiber angle in Figure 17 and Figure 18. As expected, the strengths of the specimens containing a hole are consistently less than the strengths of the unnotched specimens. Closer investigation of the notched failure strength reveals an interesting finding. If the notched failure strength is normalized by dividing by 0.8 (the ratio of notched area to unnotched area), the values of failure strength very nearly match the unnotched failure strengths. See Figure 19 and Figure 20. At room temperature, the hole is not acting as a stress concentrator, but merely reduces a specimen's strength in proportion to the lost area. At elevated temperature

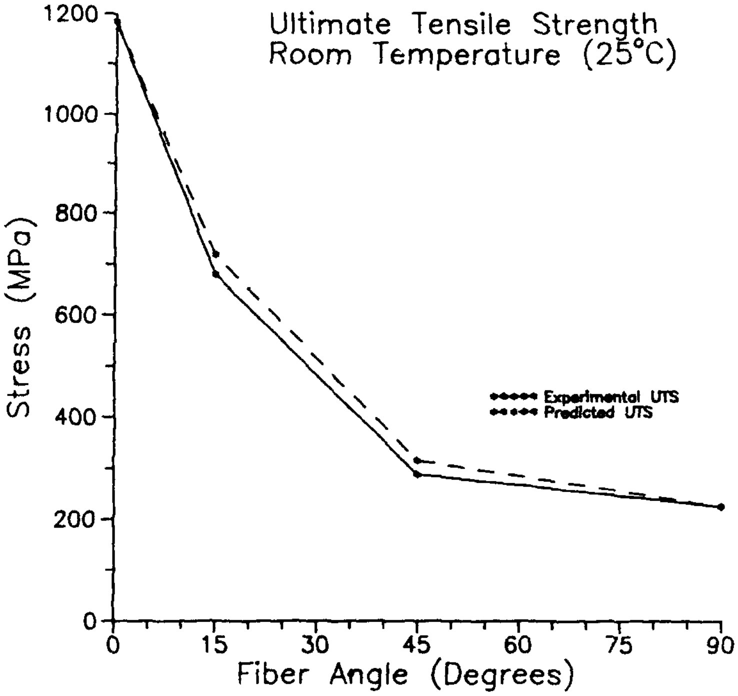

Figure 15. Experimental and predicted tensile strength at 25°C.

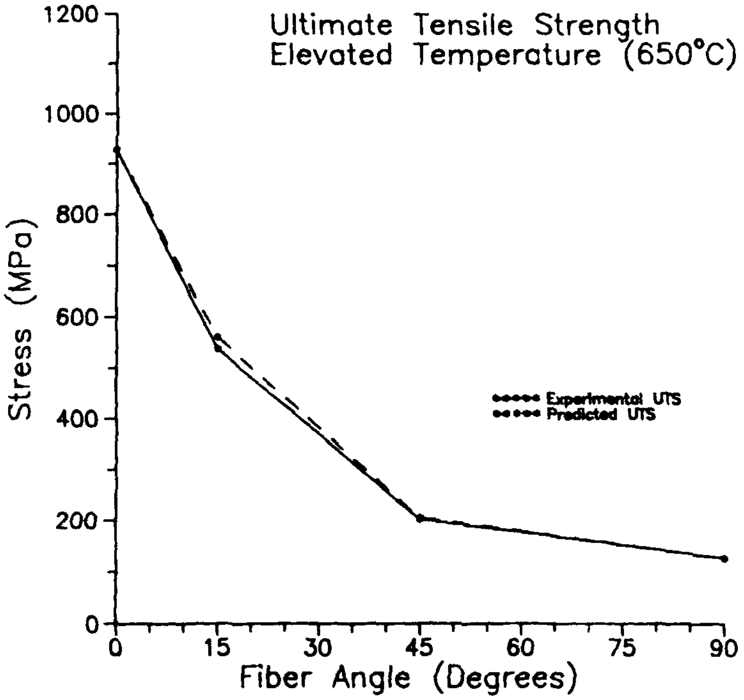

Figure 16. Experimental and predicted tensile strengh at 650°C.

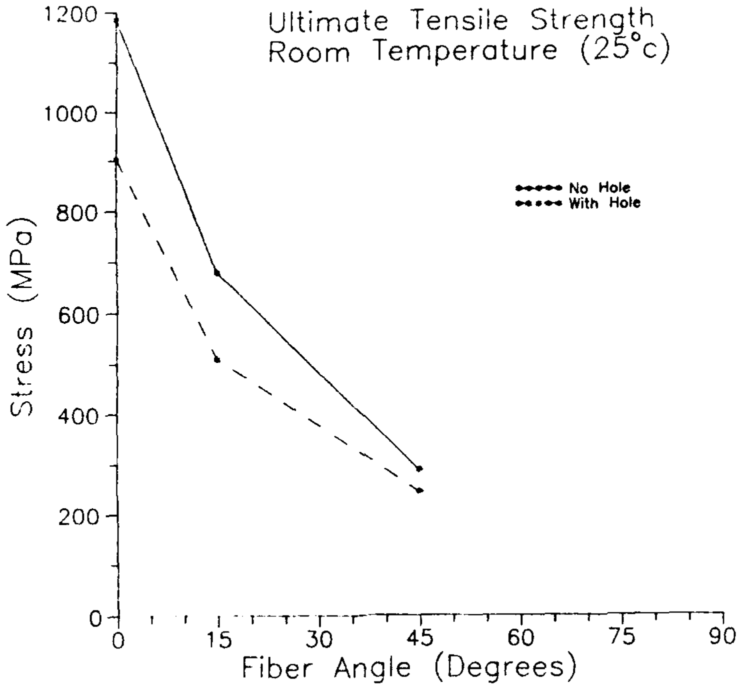

Figure 17. Tensile strength of notched and unnotched SCS-6/Ti-24Al-11Nb at 25°C.

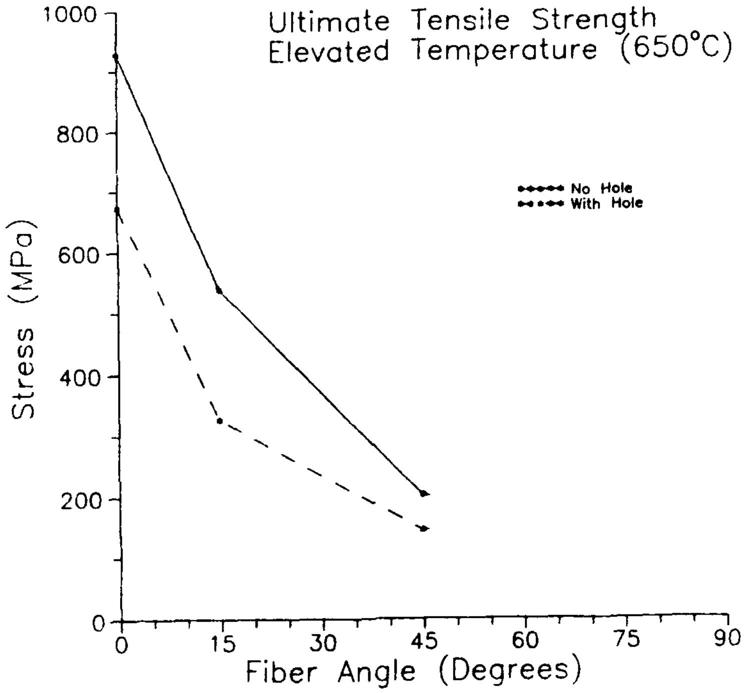

Figure 18. Tensile strength of notched and unnotched SCS-6/Ti-24Al-11Nb at 650°C.

Figure 10. Small specimen, elevated temperature test setup.

the normalized strengths of the notched specimens are still about 10% less than the unnotched strength for the 0° and 15° fiber orientations. The hole is having an effect other than subtracting load bearing area, but one not nearly as large as predicted by the stress concentration theories. Whitney discussed this phenomenon as it occurred in glass/epoxy composites (Whitney 1974). He demonstrated a direct relationship between hole size and failure strength for hole diameters less than 25.4 mm. Further investigation of the relationship between failure strength and hole size in SCS-6/Ti-24Al-11Nb is worth consideration.

Stress Concentration Factor

Though the SCS-6/Ti-24Al-11Nb failure strength appeared to be insensitive to the hole, stress concentration factors were calculated using the Greszczuk and Tan equations (24) and (25) and the finite element model described in part IV of this report. The Allison experimental material constants were used for all these calculations. The orthotropic stress concentration factors for an infinitely wide plate at room temperature are summarized in Table 9. The stress concentration factors for this same plate at elevated temperature are summarized in Table 10.

Applying the finite width correction of equation (26) to the values of Table 9 and Table 10 yields a stress concentration factor appropriate to the orientation and 2a/W ratio of this study's test specimens. Table 11 and Table 12 summarize the predicted stress concentration factors of the $[0°]_8$, $[15°]_8$, $[45°]_8$ specimen layups. Included in these tables are the stress concentration factors derived from the finite element model solutions.

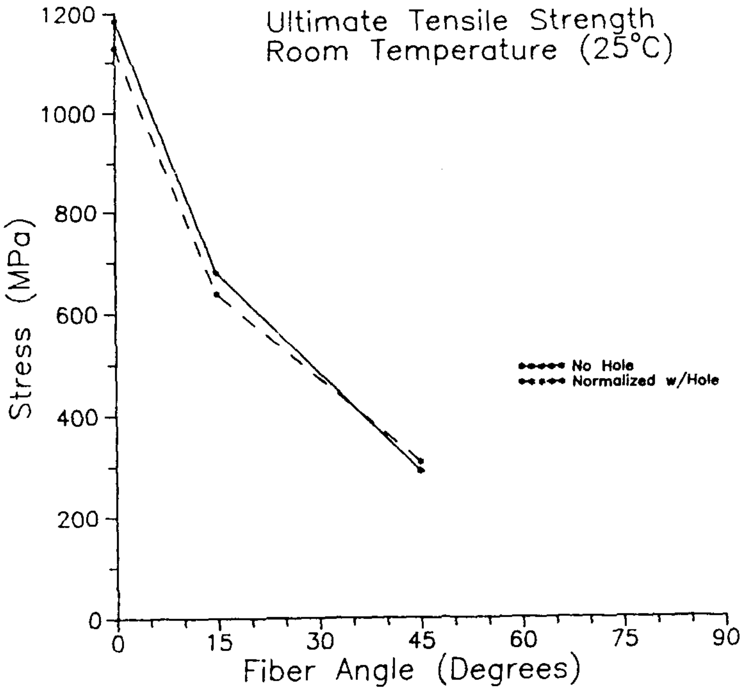

Figure 19. Normalized tensile strengths at 25°C.

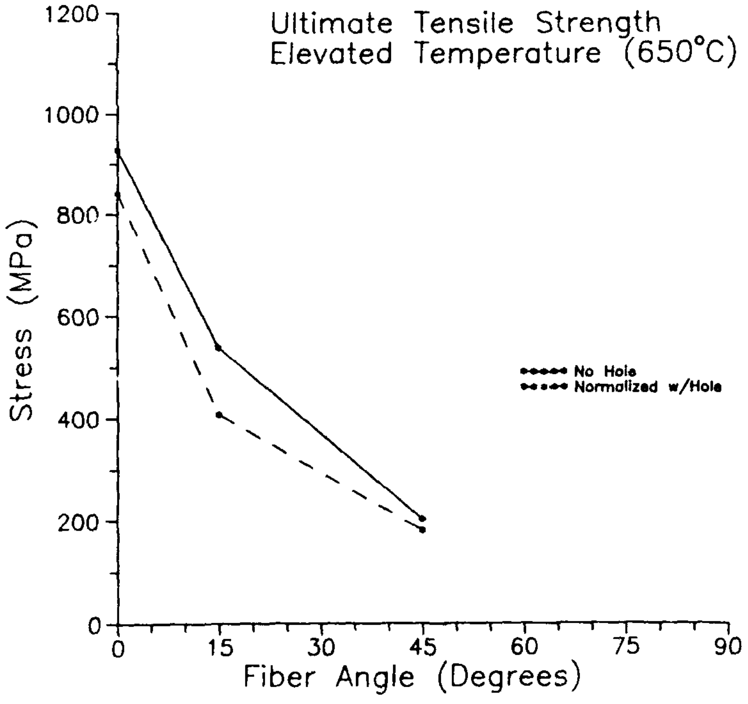

Figure 20. Normalized tensile strengths at 650°C.

Method	Material Orientation		
	$[0°]_8$	$[15°]_8$	$[45°]_8$
Greszczuk	3.68	3.32	2.65
Tan	3.16	2.99	2.64

Table 9. Room Temperature stress concentration factors for an infinitely wide plate.

Method	Material Orientation		
	$[0°]_8$	$[15°]_8$	$[45°]_8$
Greszczuk	4.13	3.48	2.57
Tan	3.05	2.87	2.56

Table 10. Elevated temperature stress concentration factors for an infinitely wide plate.

Method	Material Orientation		
	$[0°]_8$	$[15°]_8$	$[45°]_8$
Greszczuk	3.75	3.39	2.71
Tan	3.27	3.09	2.70
FEM	3.51	3.31	2.74

Table 11. Room temperature stress concentration factors for a finite width plate.

Method	Material Orientation		
	$[0^\circ]_8$	$[15^\circ]_8$	$[45^\circ]_8$
Greszczuk	4.22	3.55	2.62
Tan	3.11	2.93	2.61
FEM	3.82	3.47	2.58

Table 12. Elevated temperature stress concentration factor for a finite width plate.

The Tan solution predicts lower stress concentration factors than either the Greszczuk solution or the finite element model solution. The solutions converge toward a common value as the fiber orientation approaches 45°. Here the values of E_x and E_y are equal and the material appears close to isotropic when entering parameters into equations (24) and (25). (If true isotropic material parameters were entered into these equations, an infinite width stress concentration factor of three is obtained). The orthotropic stress concentration factors are lower because the orthotropic shear modulus, G_{xy}, is approximately twice the isotropically calculated value $G=E/2(1+\nu)$.

None of the mathematical solutions seems to predict the actual behavior of the SCS-6/Ti-24Al-11Nb test specimens. As previously stated, the material appears to be insensitive to the hole. Visual examination of the specimens during loading and X-ray examination confirm this. No cracking, delamination, fiber/matrix separation, or plastic regions develop exclusively near the hole. The traditional design method of reducing the applied load by the stress concentration factor to prevent material damage underestimates the actual strength of the material.

Damage Prior to Failure

Using the finite element model to predict stress concentration factors was one part of the effort to locate damage in the SCS-6/Ti-24Al-11Nb composite prior to failure. The finite element model's stress distribution indicated the shape of the area near the hole where damage might occur due to high stresses. The room temperature stress plots of the three fiber orientations have similar shapes and gradients, though the actual stress value of a given contour level varies. See Figures 21, 22, and 23. The maximum stress depicted for each fiber orientation is approximately the value of yield stress found from the stress-strain plot generated during tests of an unnotched specimen of the same orientation. These stress-strain plots are shown in Appendix A. Only the room temperature specimens were examined for damage prior to failure.

The finite element model accurately predicted the edge strains that were measured by the extensometer when the model predicted yielding at the hole. See Table 13. The measured strain values, taken from the stress-strain plots of notched specimens of each fiber orientation, are those that result from an applied stress equal to the remotely applied stress of the finite element model. The model predicted edge strains were taken from the axial strain plots of each fiber orientation and temperature shown in Appendix B.

Visual Observations. A specimen of each fiber orientation was observed through a ten-power optical microscope during loading in an attempt to find damage that might occur.

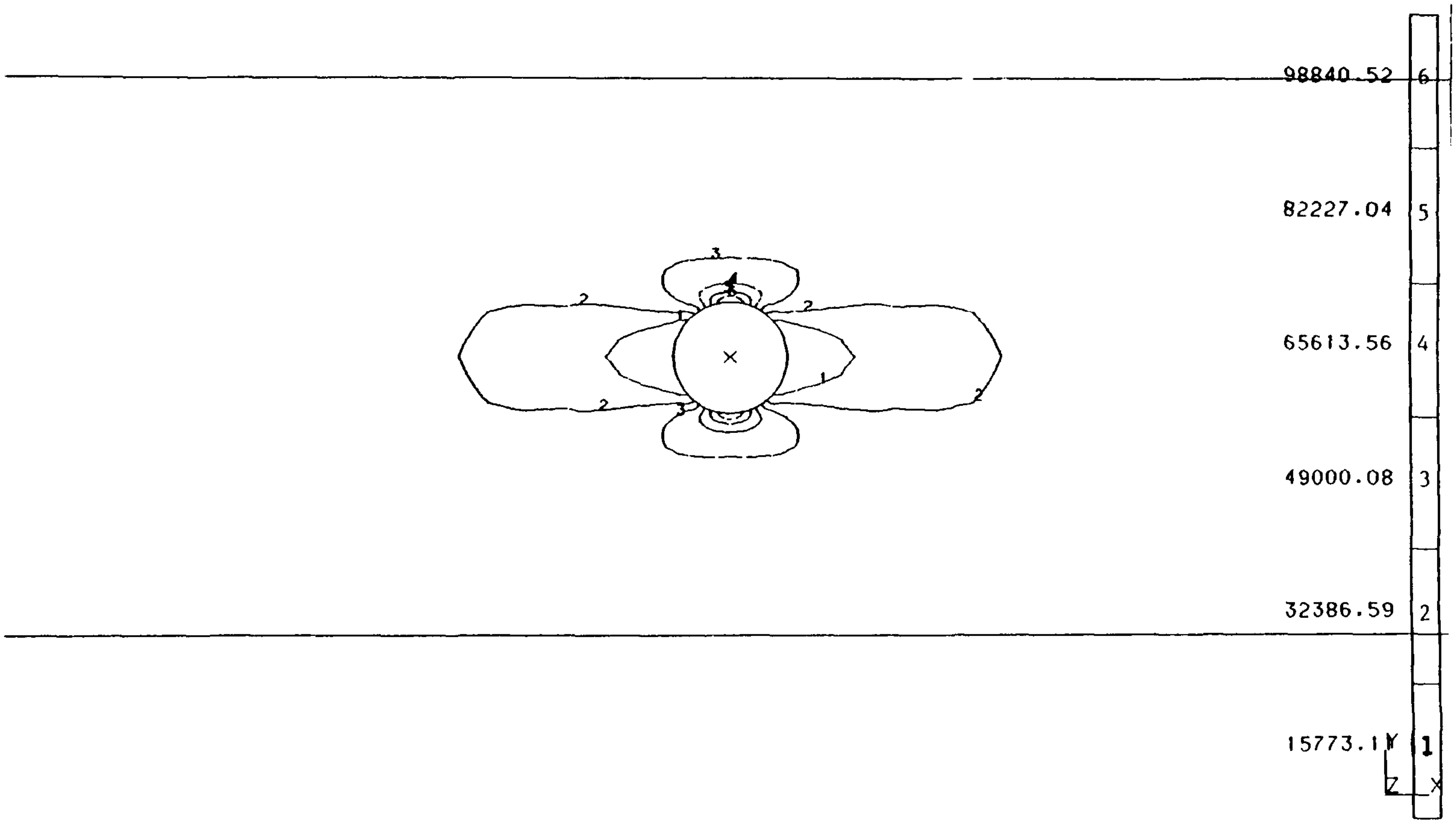

Figure 21. Axial stress in $[0^\circ]_8$ layup (values in ksi).

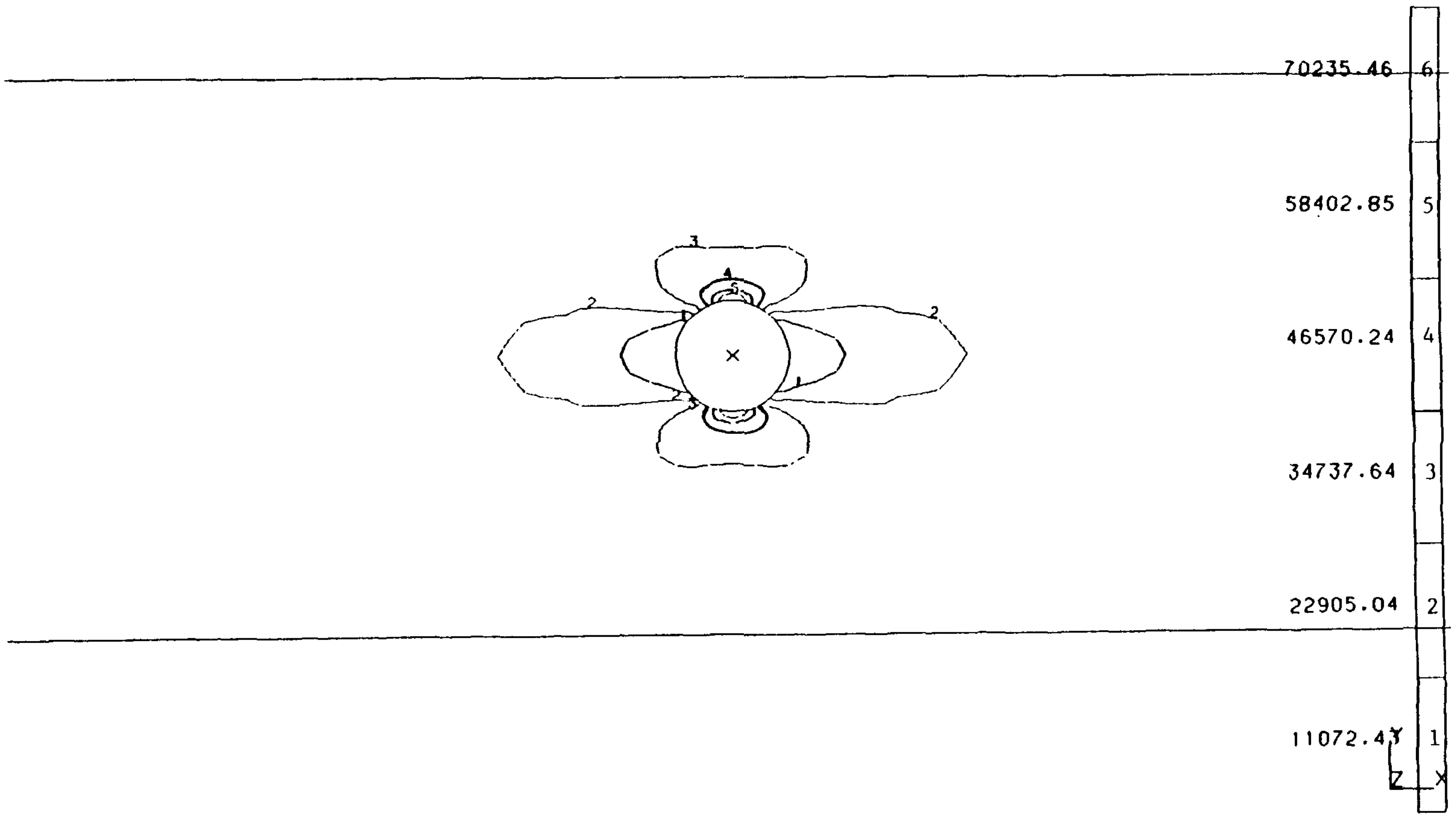

Figure 22. Axial Stress in $[15°]_8$ layup (values in ksi).

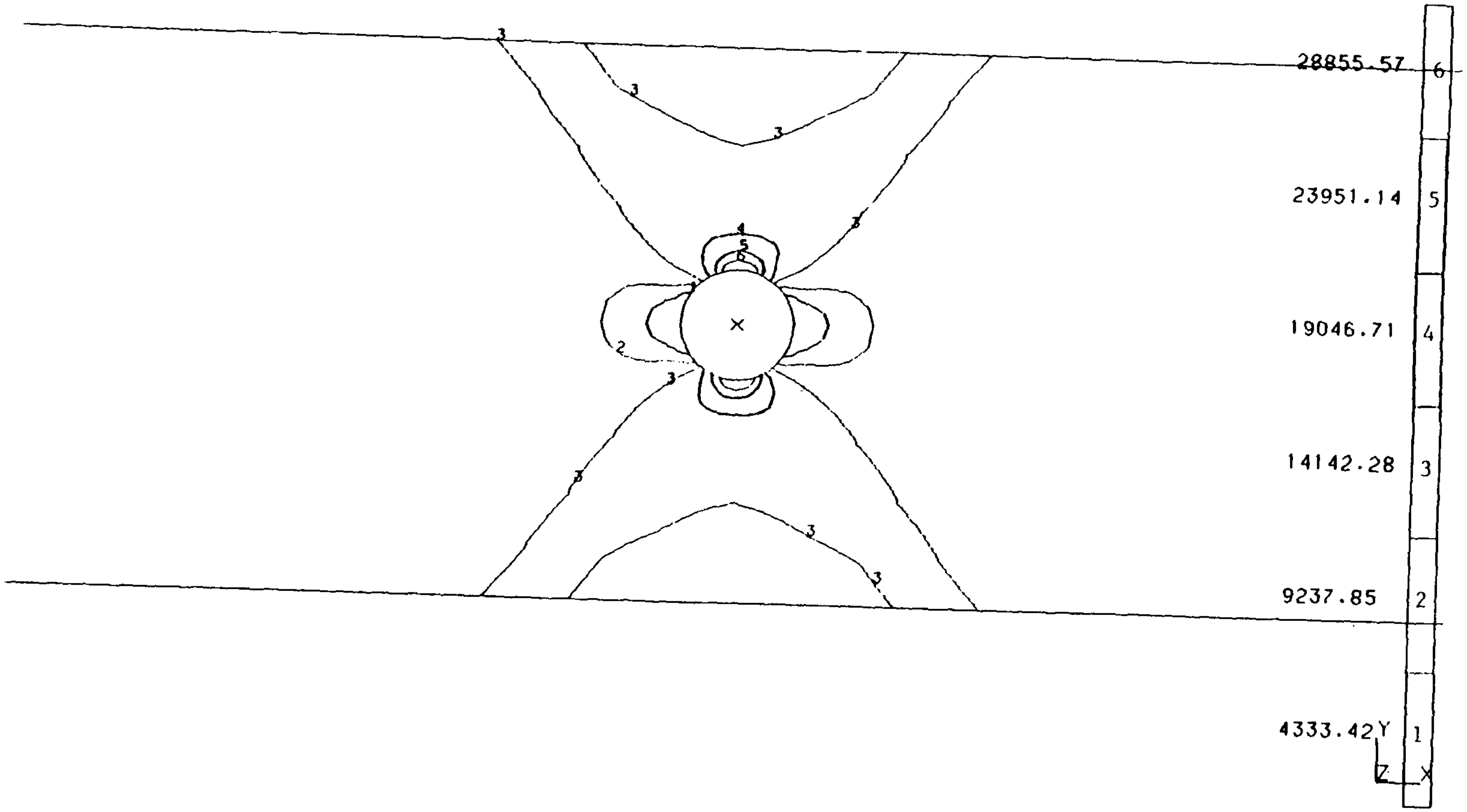

Figure 23. Axial stress in $[45°]_8$ layup (values in ksi).

Layup	Remote Stress	Temperature	Model Strain	Measured Strain
$[0°]_8$	255 MPa	25°C	1650 μm/m	1600 μm/m
$[15°]_8$	190 MPa	25°C	1230 μm/m	1250 μm/m
$[45°]_8$	89.6 MPa	25°C	610 μm/m	700 μm/m
$[0°]_8$	217 MPa	650°C	1925 μm/m	1700 μm/m
$[15°]_8$	93.1 MPa	650°C	870 μm/m	750 μm/m
$[45°]_8$	24.1 MPa	650°C	260 μm/m	250 μm/m

Table 13. Predicted and experimental edge strains.

Loads of interest were the finite element model load that predicted yielding, the first point of nonlinearity measured by the extensometer, 95% of the ultimate tensile strength, and 99% of the ultimate tensile strength. The five loading cycles did not affect the specimen's failure strength.

Zero degree fiber orientation. This specimen was the first loaded to 255 MPa and then to 414 MPa, the point of nonlinearity measured by the extensometer. No surface damage was noted. As the third loading cycle neared 855 MPa, the 95% UTS point, a very small crack appeared on the surface near the edge of the hole. This crack, oriented perpendicular to the loading direction, did not close when the load was reduced prior to unloading the specimen for X-rays. Three more very small cracks appeared near the edge of the hole between 95% and 99% UTS. These very fine cracks were each less than 1/10 of the hole diameter and did not seem to grow after they appeared. See Figure 24. No further damage was observed prior to failure.

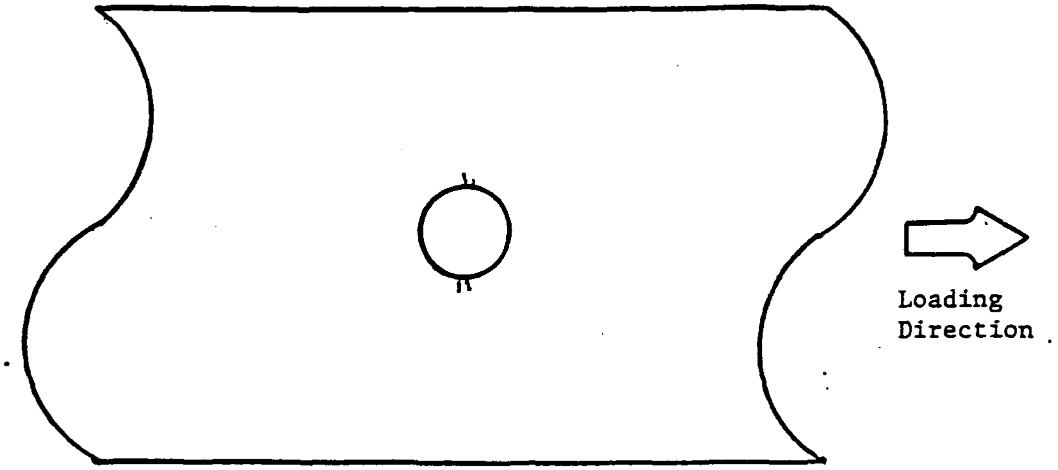

Figure 24. Cracks appearing on surface of $[0^\circ]_8$ specimen.

Fifteen degree fiber orientation. No damage appeared during loading to 190 MPa where the finite element model predicted yielding at the hole. Further loading revealed no damage until near the extensometer nonlinearity of 400 MPa. At this load a series of thin crack-like lines developed on the specimen's surface. See Figure 25. These cracks were approximately 1.5 mm long and parallel to the fiber direction of the specimen. They did not close when the load was reduced to zero. More of these crack lines appeared when the load was increased above 400 MPa toward 480 MPa (95% UTS), but they did not grow longer. The specimen failed at 498 MPa, prior to the 99% UTS load of 503 MPa.

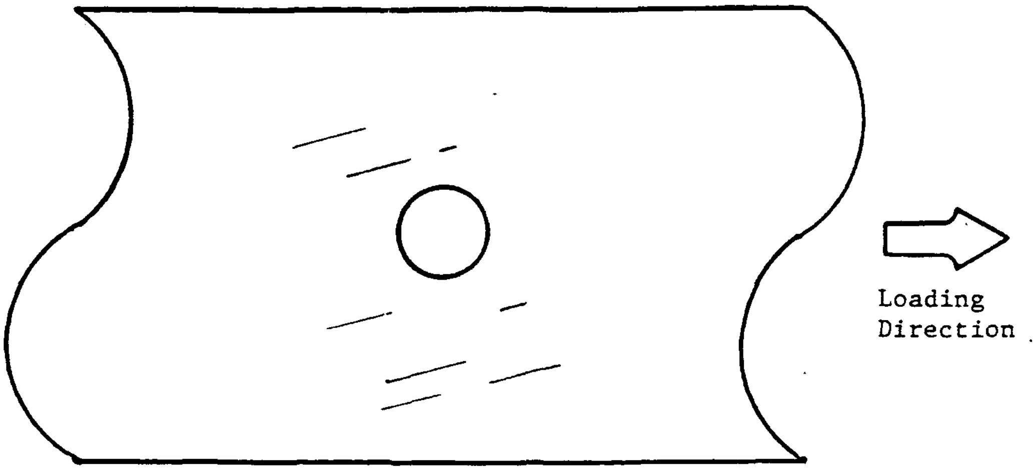

Figure 25. Cracks appearing on surface of $[15°]_8$ specimen.

Forty-five degree fiber orientation. No surface damage appeared throughout the loading cycles of this specimen. The extensometer nonlinearity occurred at 227 MPa, very near the 95% UTS value of 232 MPa, so these observations were combined as one loading cycle. This specimen failed at the 99% UTS value of 243 MPa.

Radiographic Observations. Radiographic inspection of the $[0°]_8$, $[15°]_8$, and $[45°]_8$ test specimens showed no internal damage at any point during loading. The photographs produced from the radiographs and included here are representative of all the radiographs produced after loading to the stresses indicated previously. The resolution of the radiograph is much greater than these photographs show, so even small defects if present could have been detected. Figure 26 shows the specimens prior to loading; Figure

27 shows the specimens after they had been loaded to the point of extensometer nonlinearity; and Figure 28 shows the specimens after they had been loaded to 95% of failure strength.

Failure Characteristics

The failure surfaces of all the tested composite layups can be divided into two groups by temperature. The elevated temperature fracture surfaces share characteristics not found in the room temperature fracture surfaces. Within each thermal group, the off-axis specimens show similarities not found in the specimens loaded parallel to the fibers. In general, the room temperature fracture surfaces display brittle fracture of both the fibers and matrix, with very little fiber pull out and a slight amount of necking. The $[0^\circ]_8$ specimens' fracture surface is perpendicular to the fibers, while the $[15^\circ]_8$ and $[45^\circ]_8$ specimens' fracture surface is parallel to the fibers. The elevated temperature fracture surfaces, on the other hand, display brittle fracture of the fibers and ductile fracture of the matrix, with extensive fiber pull out, fiber matrix separation, and obvious necking. The orientation of the fracture surface to the fiber direction is the same at elevated temperature as it was at room temperature.

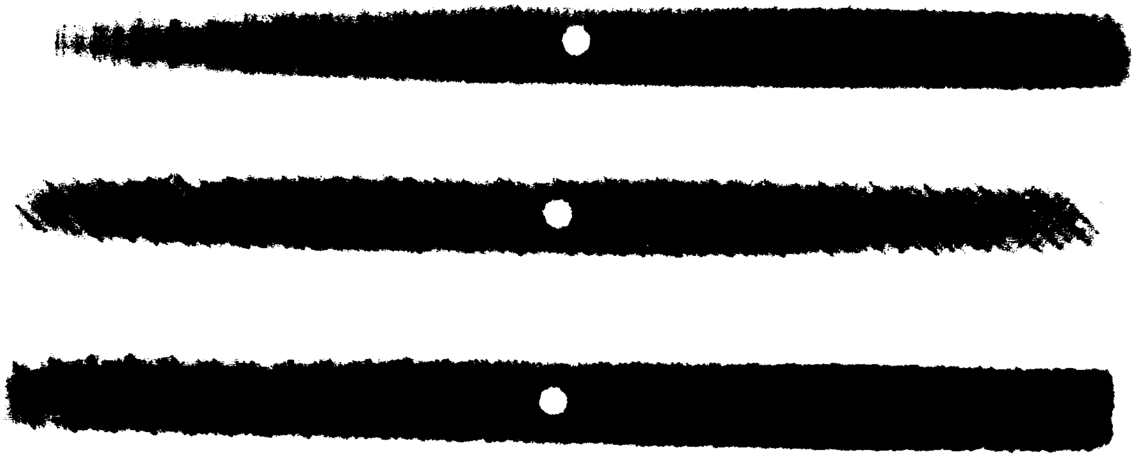

Figure 26. Radiograph of specimens prior to loading.

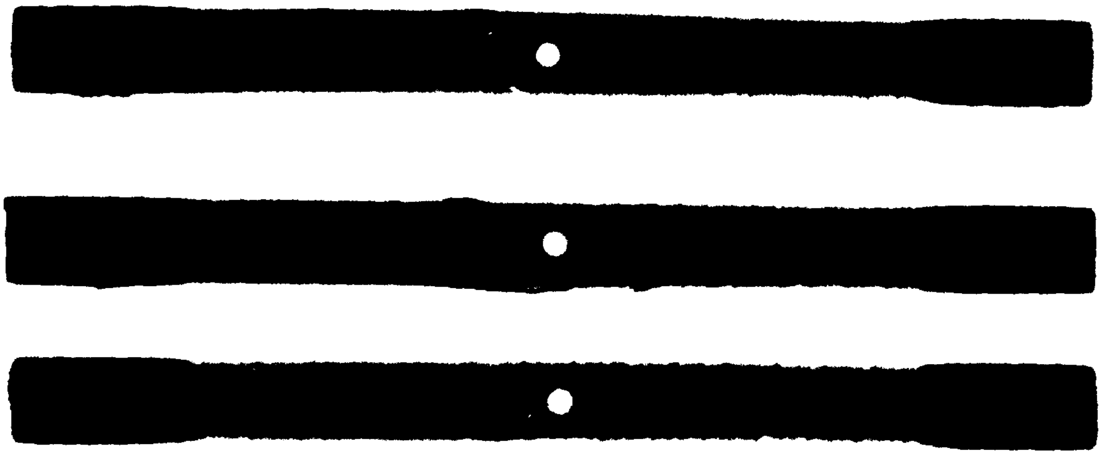

Figure 27. Radiograph of specimens after loading to extensometer nonlinearity.

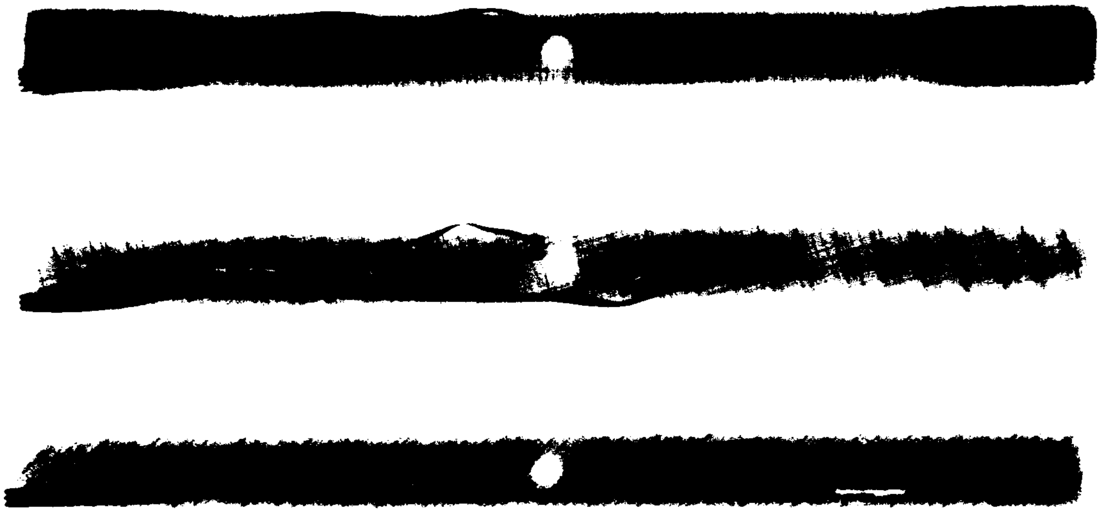

Figure 28. Radiograph of specimens after loading to 95% of failure strength.

Room Temperature Failure.

Zero degree fiber orientation. Failure of the $[0^\circ]_8$ layup is strain dominated. Examination of the stress-strain curves, Figure 29, reveals that the strain at failure is the same for both the notched and unnotched specimens. This strain is the maximum fiber strain and is limited to approximately 1% (Gambone 1990b:13).

A macroscopic view of the notched and unnotched fracture is shown in Figure 30. Little necking is evident and the fracture surface is perpendicular to the fibers. Examining the fracture surface with a scanning electron microscope (SEM) revealed a brittle fracture of the fibers and matrix with little fiber pull out. Figure 31 shows two views of the unnotched specimen, while Figures 32 and 33 show views of the notched specimen's

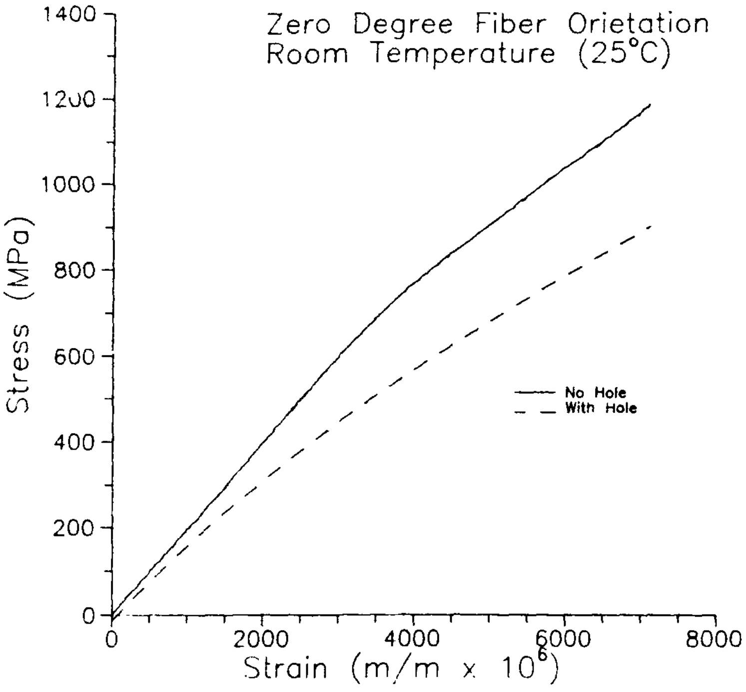

Figure 29. Stress-strain plot of $[0°]_8$ layup at 25°C.

fracture surface near the hole and away from it. No differences exist between the fracture surface near the hole and away from it.

Fifteen degree fiber orientation. Maximum strain failure criteria cannot be applied to specimens loaded off axis. Here a maximum stress approach is appropriate with strain limited by it. The stress-strain plots of unnotched and notched specimens are shown in Figure 34. A macroscopic view of the notched and unnotched fracture is shown in Figure 35. The matrix is fractured in a stair-step fashion that follows the fiber orientation. In addition the fracture starts approximately 75° from the loading axis rather

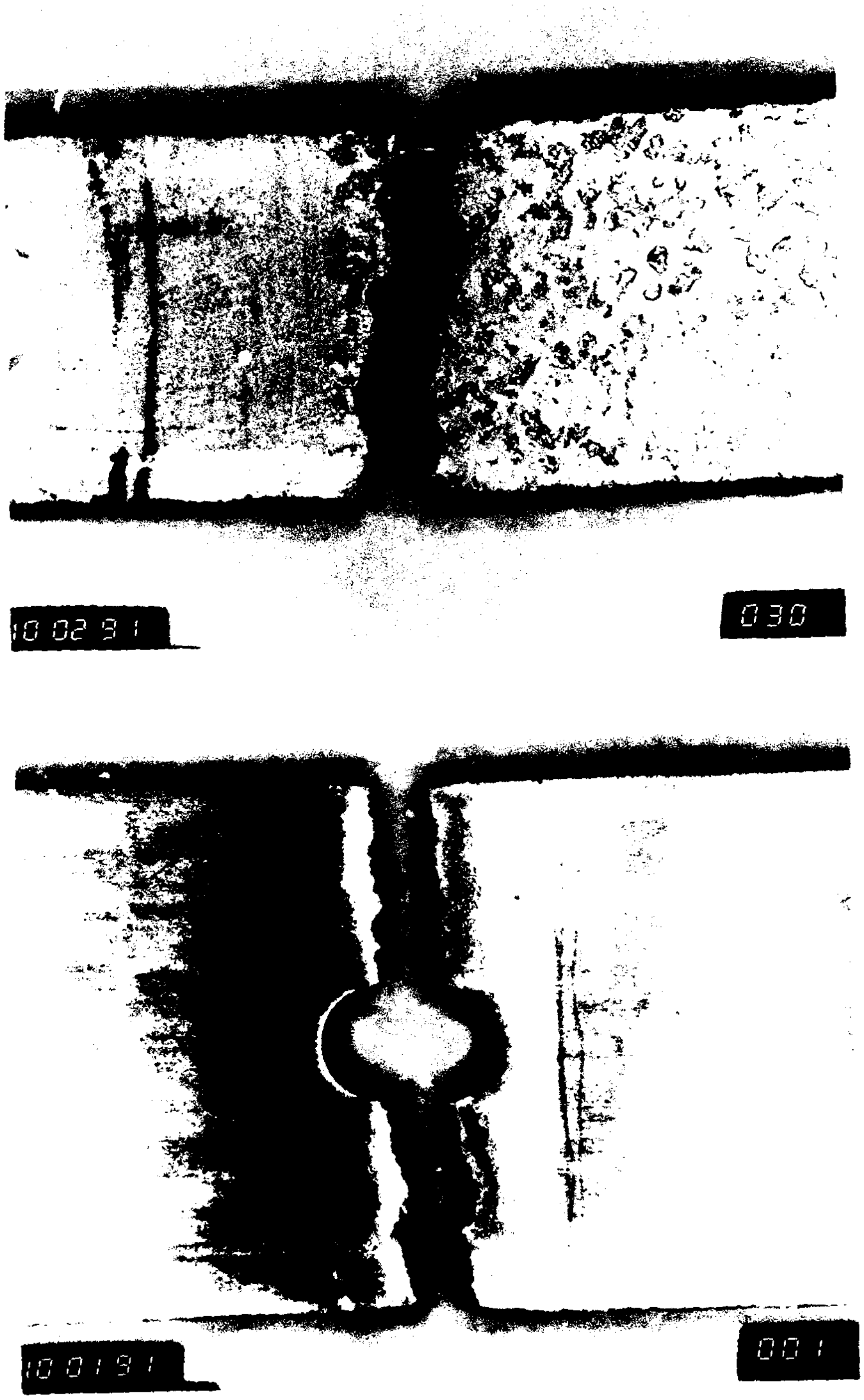

Figure 30. Fracture of $[0^\circ]_8$ specimens (top) unnotched (bottom) notched.

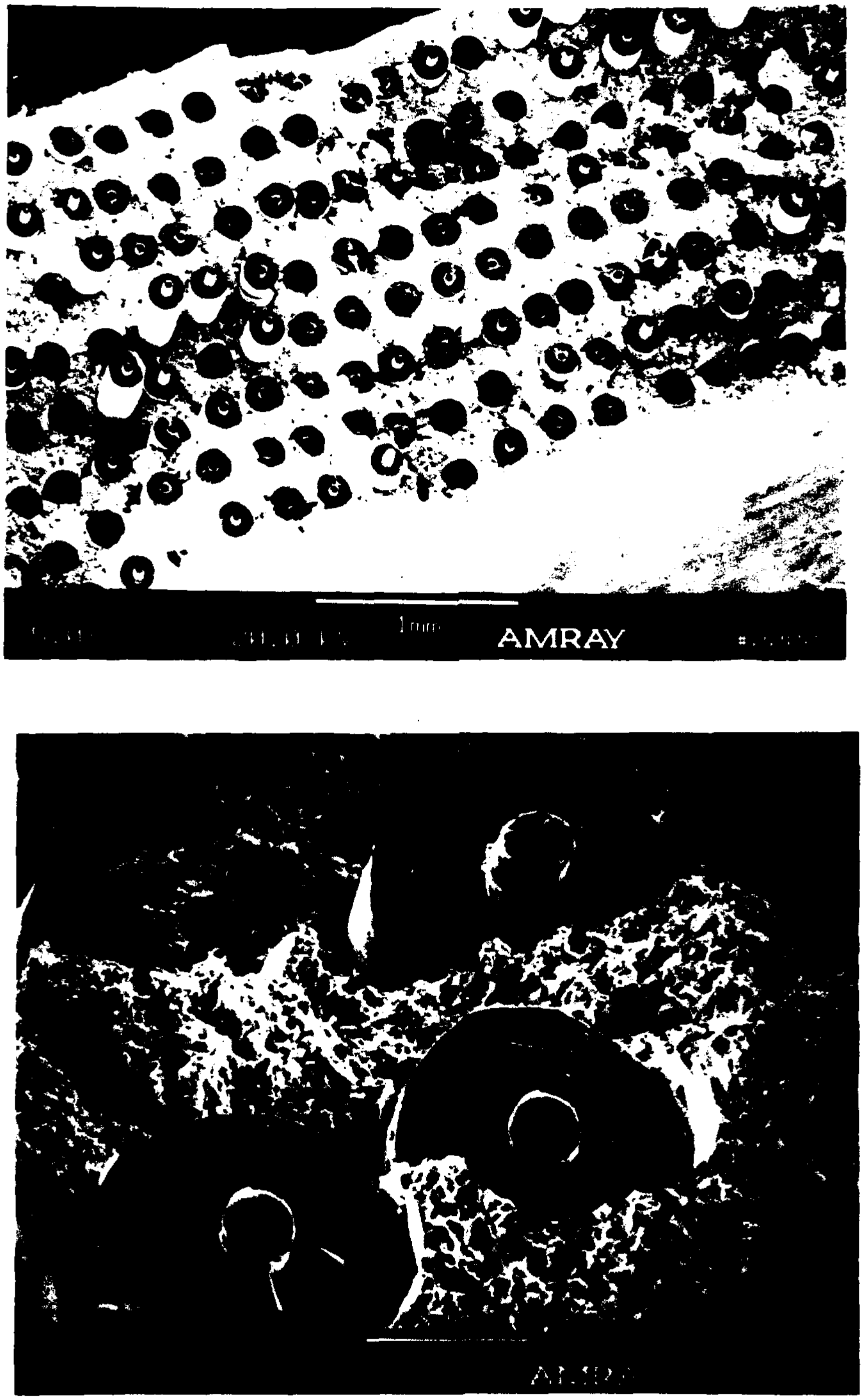

Figure 31. Fracture surface of unnotched $[0^\circ]_8$ specimen.

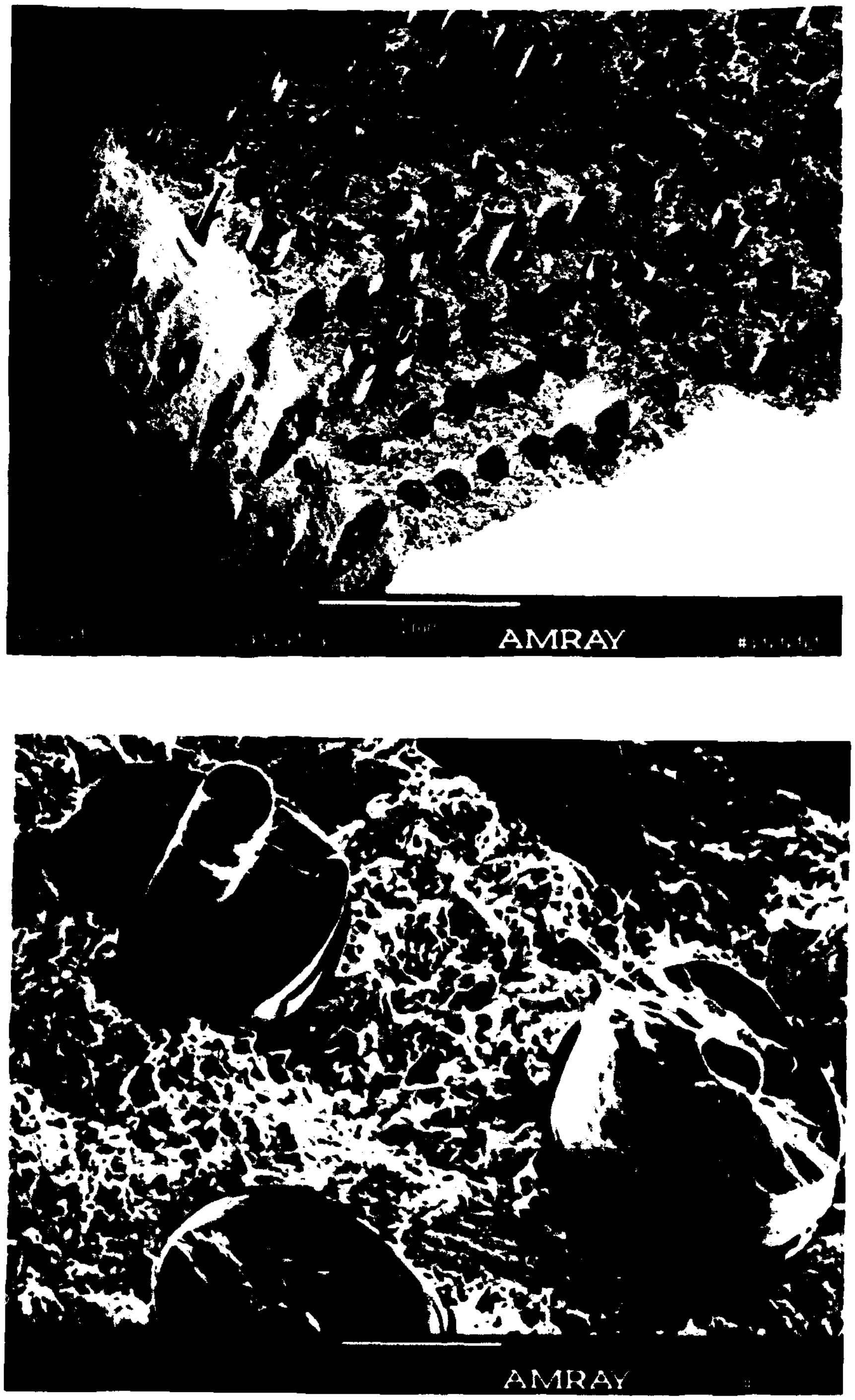

Figure 32. Fracture surface of notched [0°]$_8$ specimen near hole.

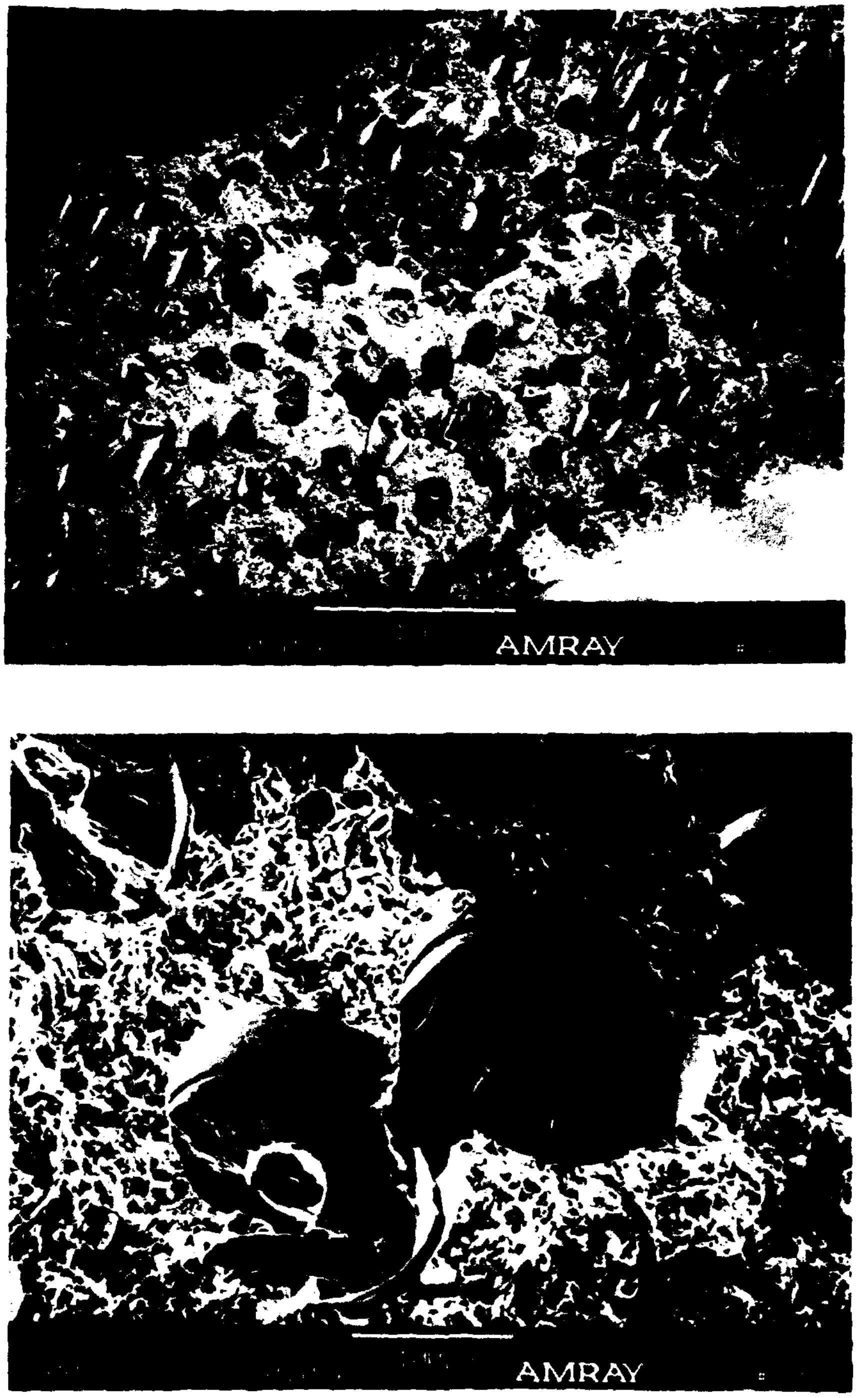

Figure 33. Fracture surface of notched $[0°]_8$ specimen away from hole.

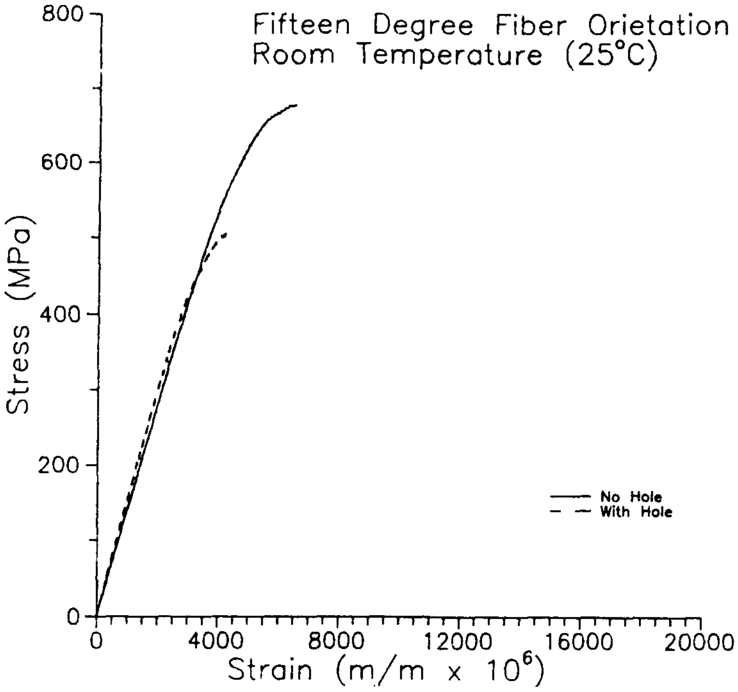

Figure 34. Stress-strain plot of $[15°]_8$ layup at 25°.

than 90° from it. The SEM magnified views of the fracture surfaces suggest a brittle fracture of the matrix after the fiber matrix interface has failed. The steps occur when a fiber breaks and the matrix can cleave perpendicular to the loading axis. This is particularly evident in Figures 36 and 37, which show the fracture surface of the unnotched and notched specimens respectively. The fibers and matrix separate very cleanly as seen in Figure 38. The fiber surfaces are virtually undamaged as are the channels in the matrix. The fibers at the left of Figure 36 (top) are held in place by the matrix at only a few points. No differences exist between the notched and unnotched fracture surfaces, and little fiber pull out is evident.

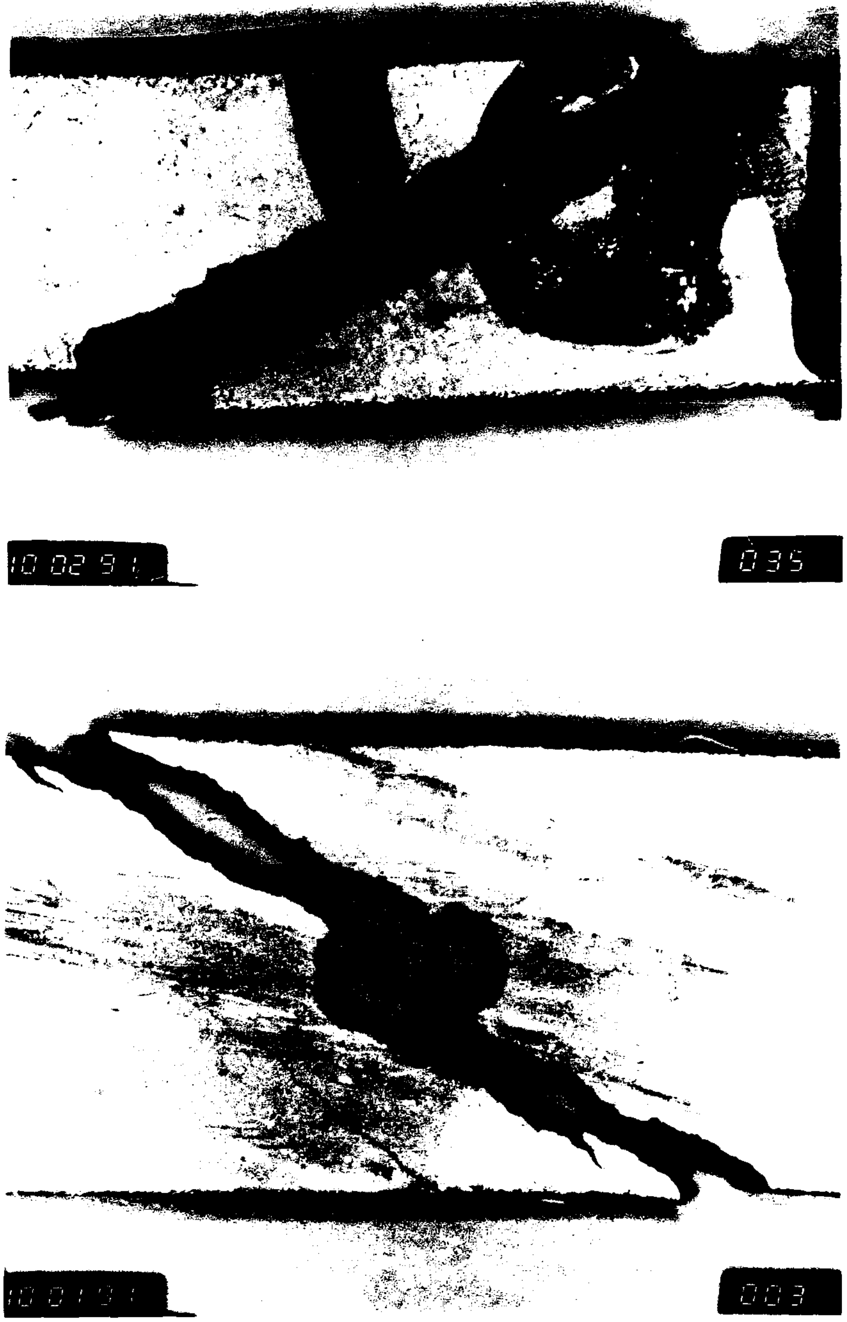

Figure 35. Fracture of $[15^\circ]_8$ specimens (top) unnotched (bottom) notched.

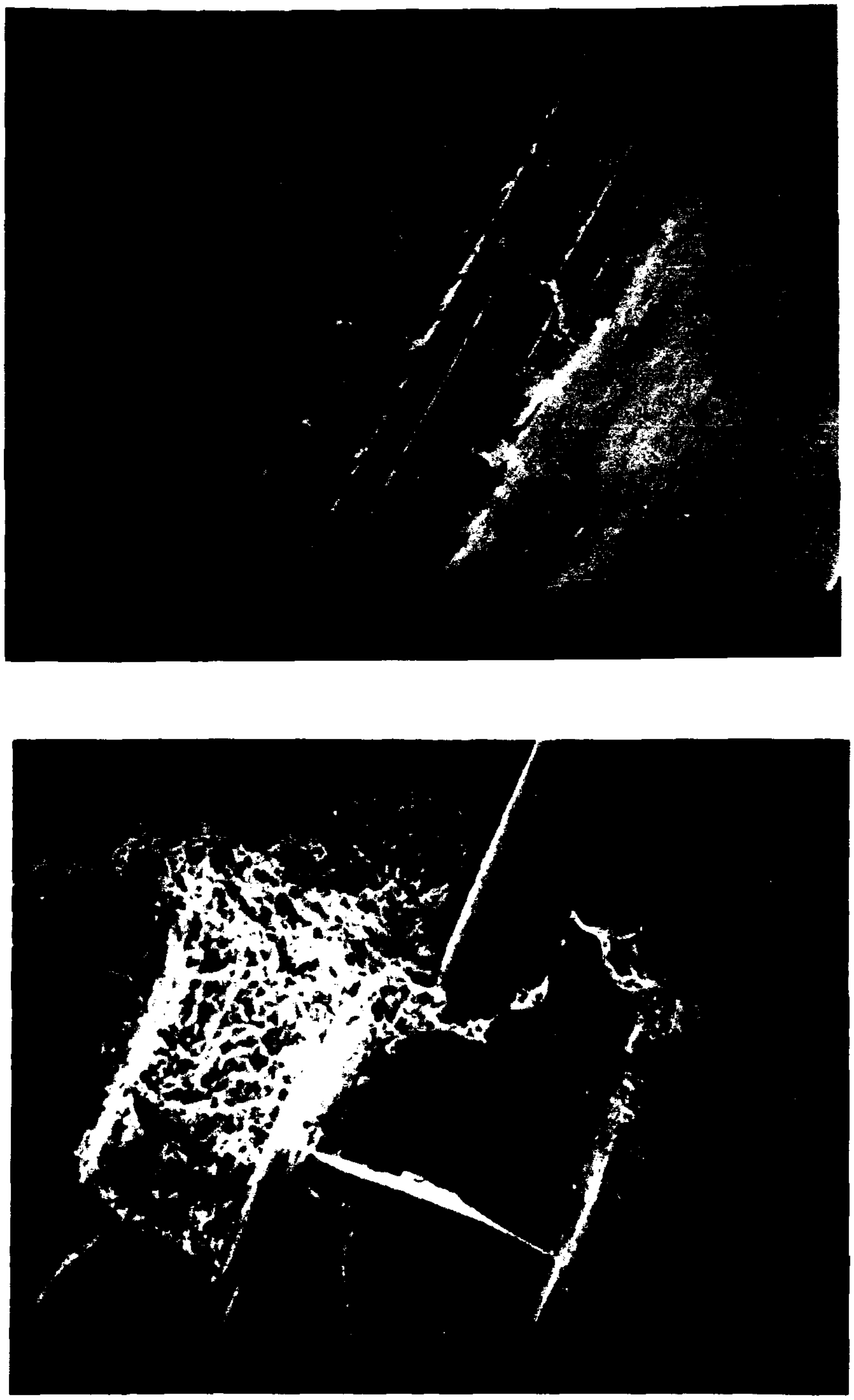

Figure 36. Fracture surface of unnotched [15°]$_8$ specimen.

Figure 37. Fracture surface of notched $[15^\circ]_8$ specimen near hole.

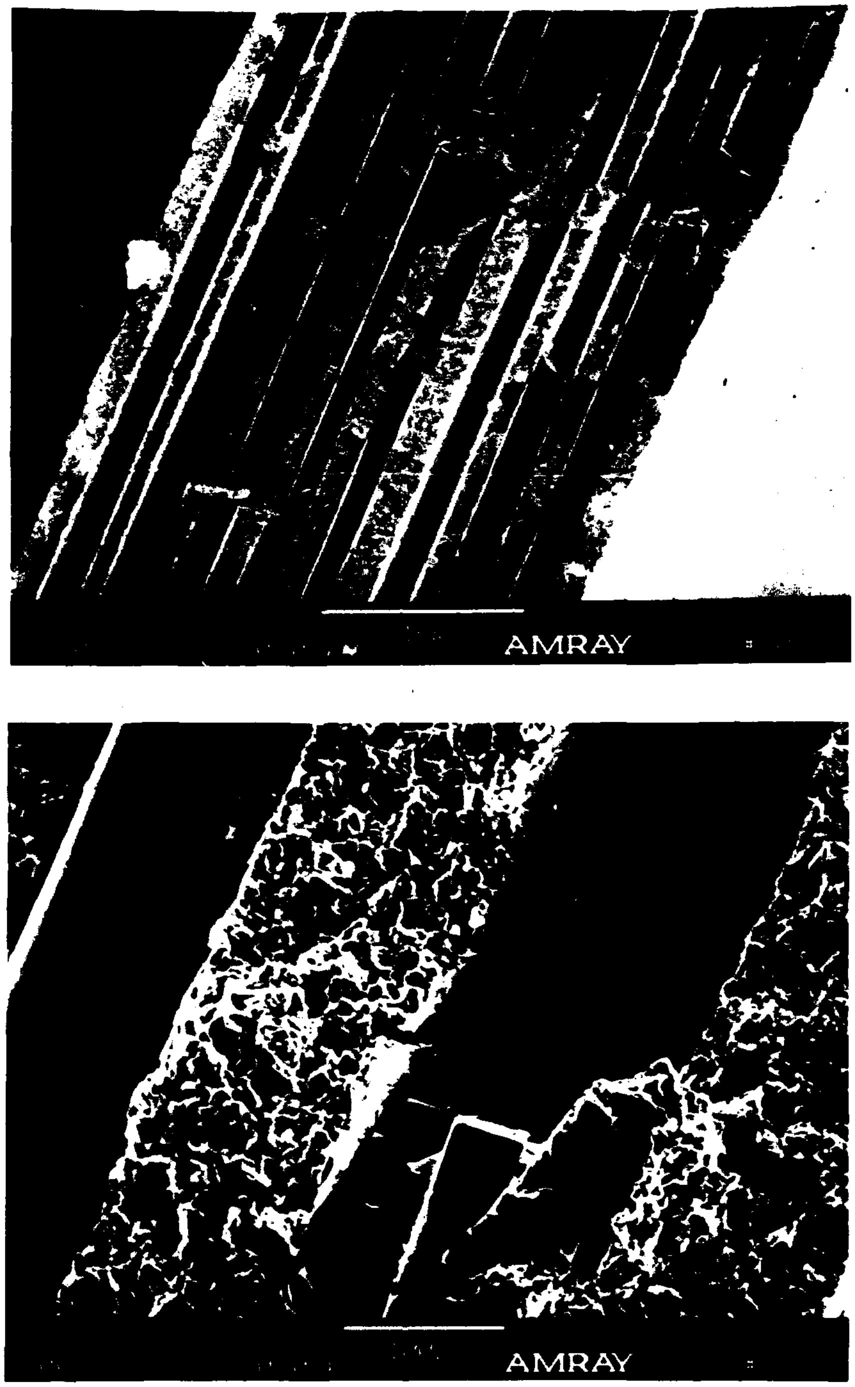

Figure 38. Fracture surface of notched [15°]$_8$ specimen away from hole.

Forty-five degree fiber orientation. The failure of the $[45^\circ]_8$ layup is similar to the failure of the $[15^\circ]_8$ layup. A maximum stress approach is appropriate for predicting failure, with strain limited by it. The stress-strain plots of unnotched and notched specimens are shown in Figure 39. Figure 40 is a macroscopic view of the notched and unnotched fractures. As in the $[15^\circ]_8$ specimens, the matrix showed a stair-step pattern in its fracture. These steps are much finer than those of the previous fiber orientation, and the fracture surface is generally confined to a single column of fibers across the specimen's width. Again the fiber/matrix interface fails first followed by brittle fracture of the matrix. The fiber surfaces are clean and undamaged, while the troughs in the matrix show only minor cracking. The SEM magnified views of Figures 41, 42, and 43 show no differences between the notched and unnotched specimens' fracture surfaces.

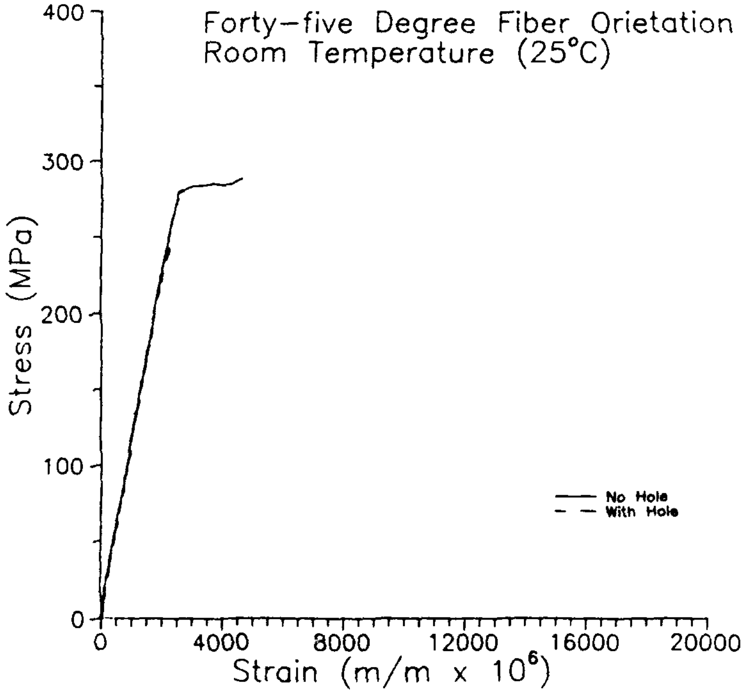

Figure 39. Stress-strain plot of $[45^\circ]_8$ layup at 25°C.

Figure 40. Fracture of $[45^{\circ}]_8$ specimens (top) unnotched (bottom) notched.

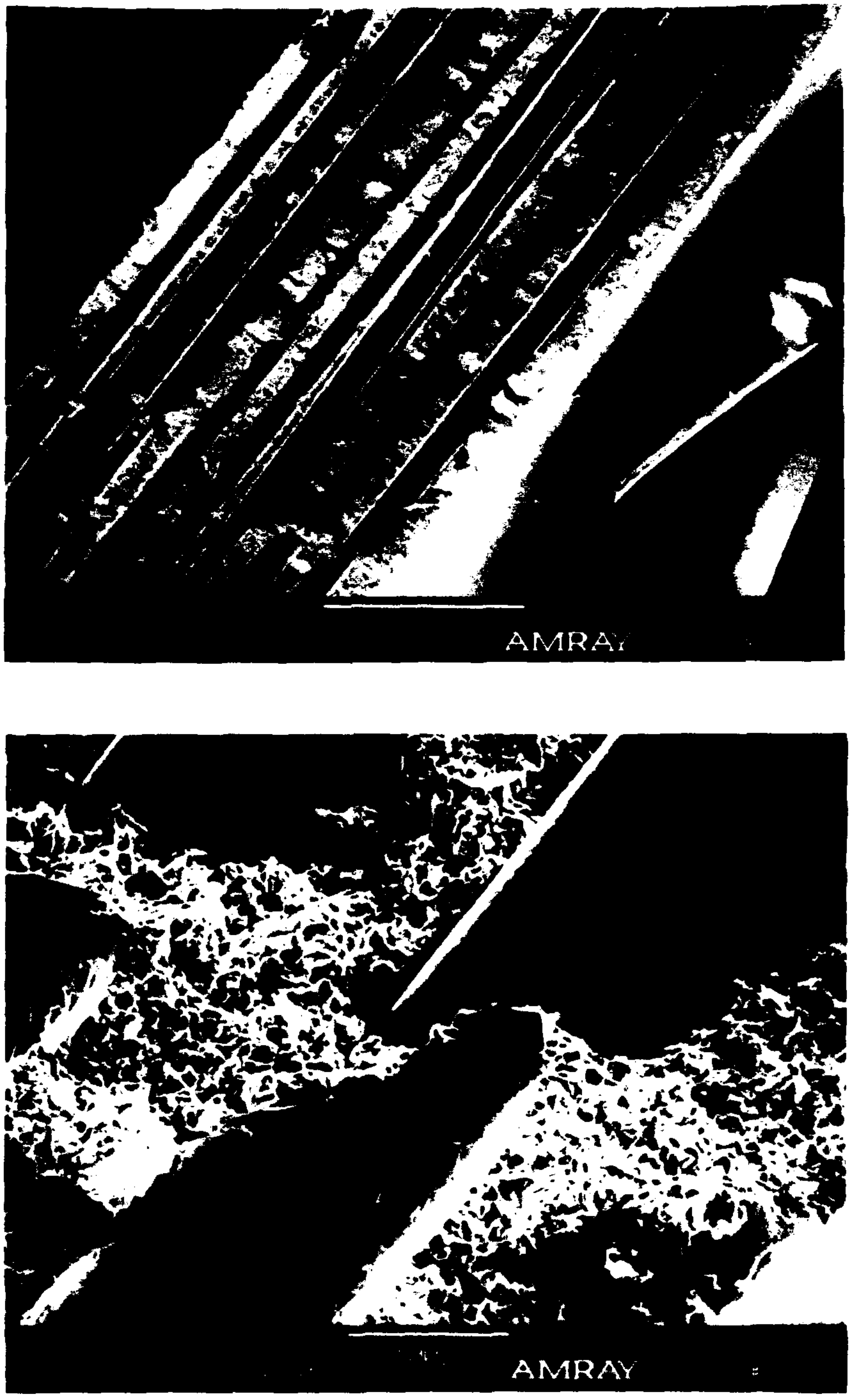

Figure 41. Fracture surface of unnotched $[45^\circ]_8$ specimen.

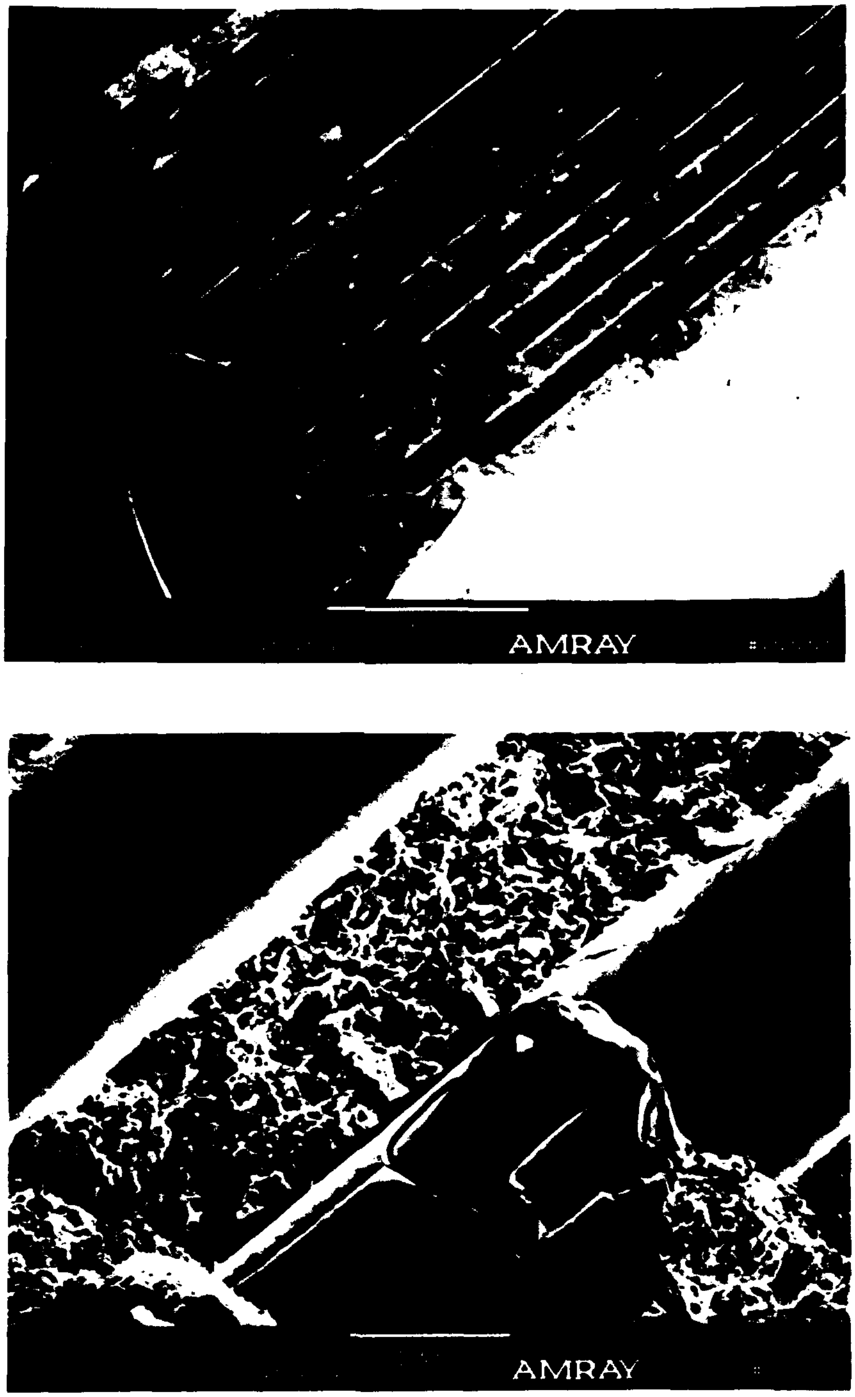

Figure 42. Fracture surface of notched $[45^\circ]_8$ specimen near hole.

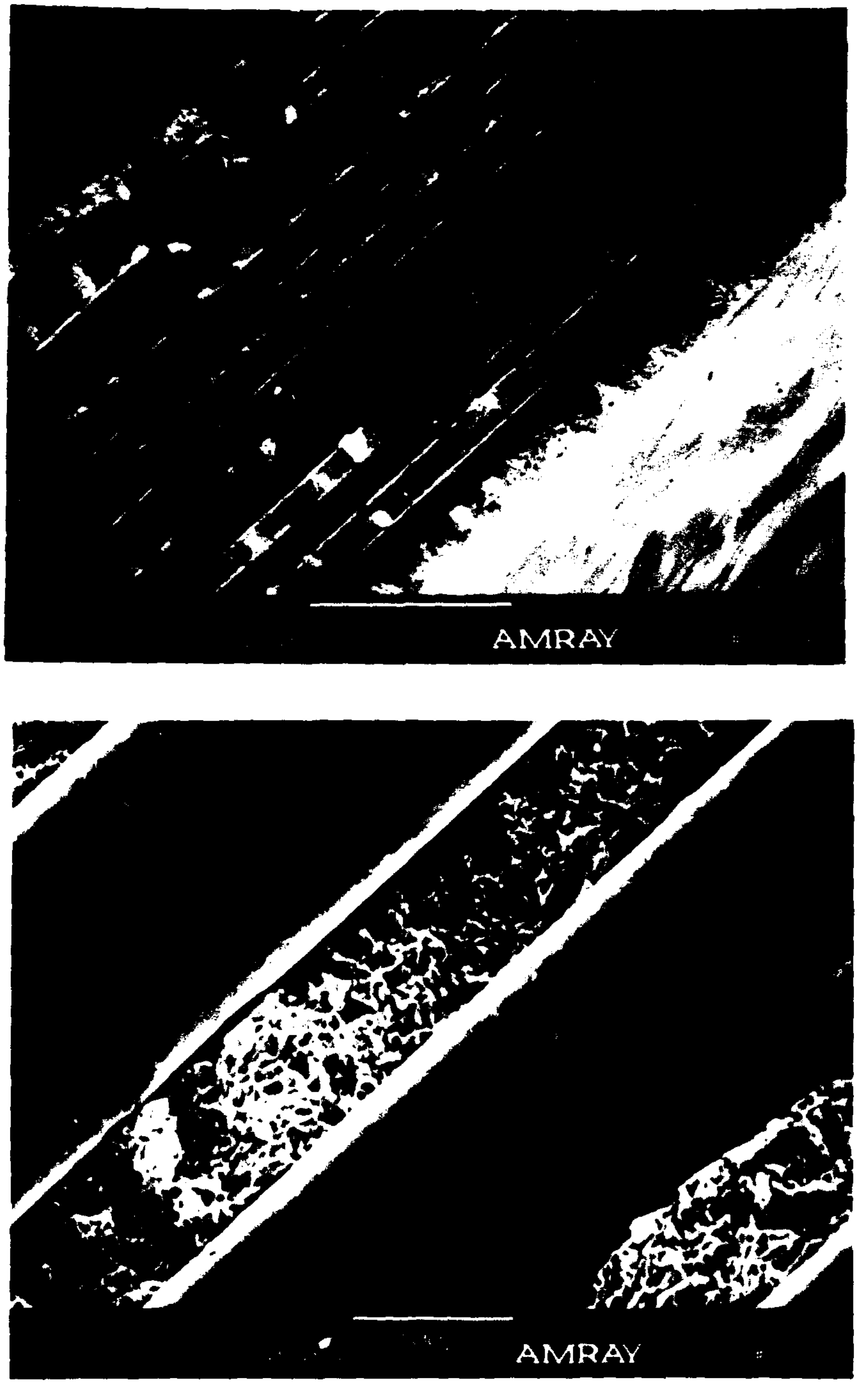

Figure 43. Fracture surface of notched $[45^\circ]_8$ specimen away from hole.

Elevated Temperature Failure.

Zero degree fiber orientation. Failure of the $[0°]_8$ layup is strain dominated as the room temperature failure was. Examining the stress-strain plots of the zero degree fiber orientation, Figure 44, reveals that the notched and unnotched specimens both failed at 6150 μm/m strain. The maximum strain at elevated temperature is 900 μm/m less than the maximum strain at room temperature, and this is similar to the difference in strains reported by Allison (Gambone 1990b:8). A macroscopic view of the notched and unnotched fracture is shown in Figure 45. Necking and fiber pull out are apparent, and the fracture surface is perpendicular to the fibers. Examining the fracture surface with the SEM reveals brittle fracture of the fibers, but ductile fracture of the matrix. Necking of the matrix has pulled the matrix away from the fibers, and there is extensive fiber pull out. Figures 46, 47, and 48 show the unnotched and notched fracture surfaces. Extensive cracking is visible in the exposed fiber channels of the notched specimen. See the bottom photos of Figures 47 and 48. This probably occurred during the almost perfectly plastic deformation between 5700 μm/m strain and failure at 6200 μm/m. No differences exist between the fracture surface near the hole and way from it.

Fifteen degree fiber orientation. Strain of both the notched and unnotched specimens exceeded 20,000 μm/m, the maximum measurable strain of the data acquisition system used in this study. Both notched and unnotched stress-strain plots have extensive plastic regions of large deformations with little increase in stress. See Figure 49. A macroscopic view of the notched and unnotched fracture is shown in Figure 50. In this

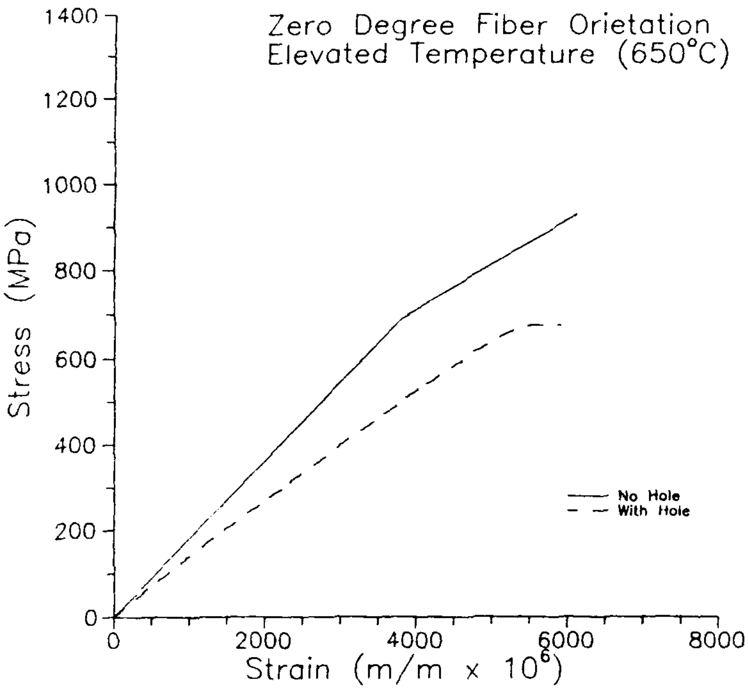

Figure 44. Stress-strain plot of $[0°]_8$ layup at 650°C.

figure, necking and fiber pull out are clearly visible. Except at the edges where delamination occurred, the matrix fracture followed a single column of fibers across the width of the specimen. In addition, the fracture starts approximately 75° from the loading axis rather than 90° from it. The magnified views of the fracture surfaces, Figures 51, 52, and 53, show an almost complete separation of the fibers and matrix at the fracture and a ductile fracture of the matrix. The fiber surfaces are clean and undamaged indicating a weak fiber matrix interface bond. Fiber pull out is visible in Figure 51; the fiber ends extend past the edge of the matrix and into the hole. The fiber channels of both the notched and unnotched specimens show the extensive cracking of large plastic deformation prior to failure. No differences exist between the notched and unnotched fracture surfaces.

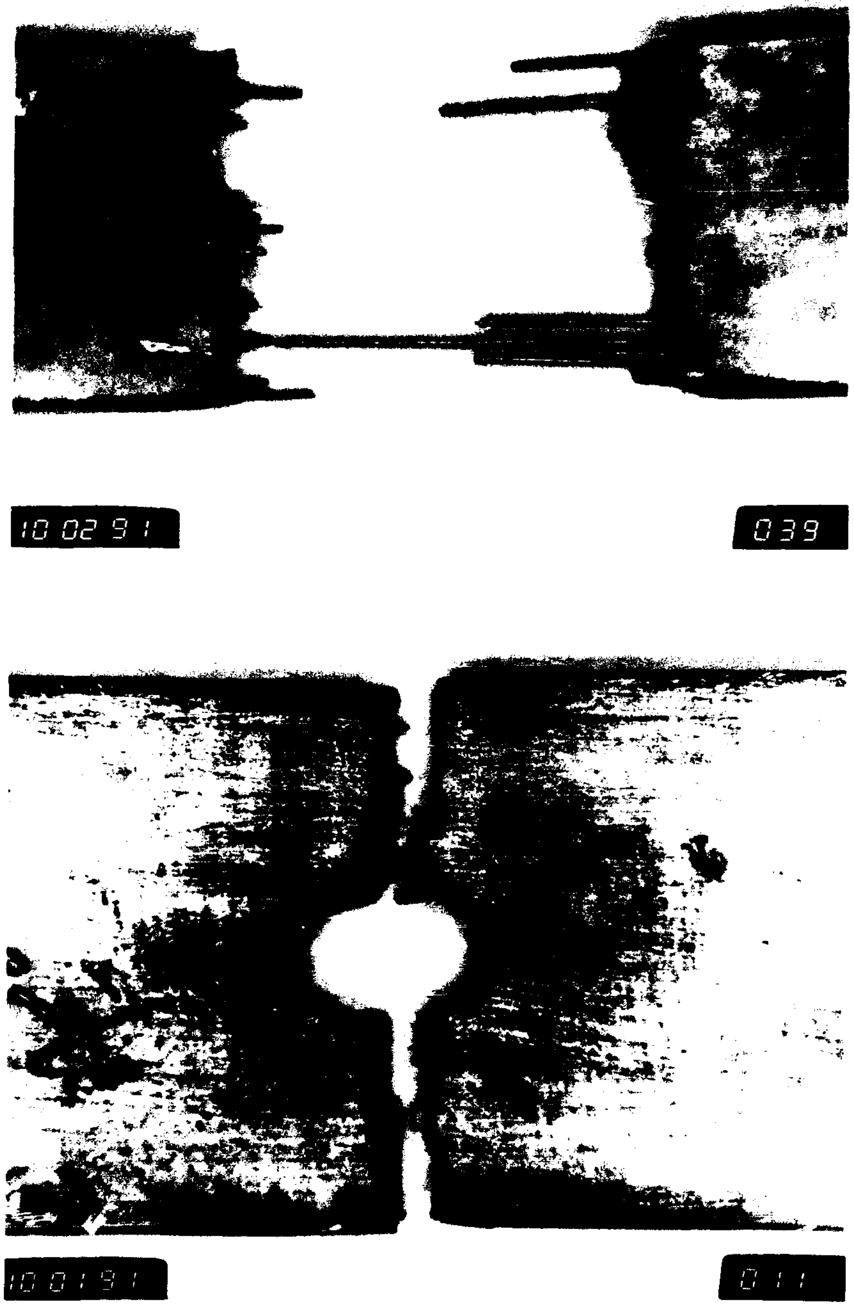

Figure 45. Fracture of $[0^\circ]_8$ specimens (top) unnotched (bottom) notched.

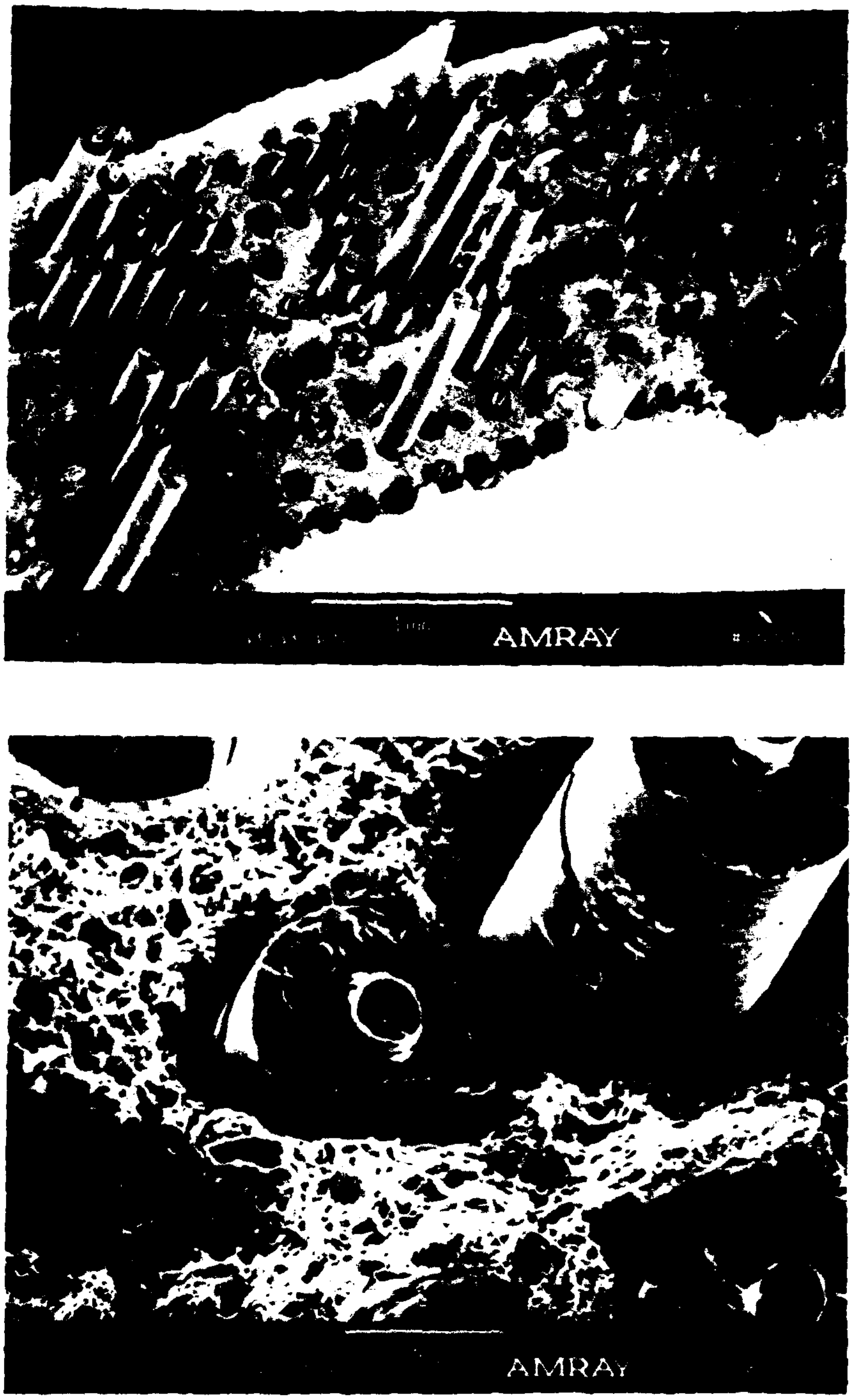

Figure 46. Fracture surface of unnotched $[0^{\circ}]_8$ specimen.

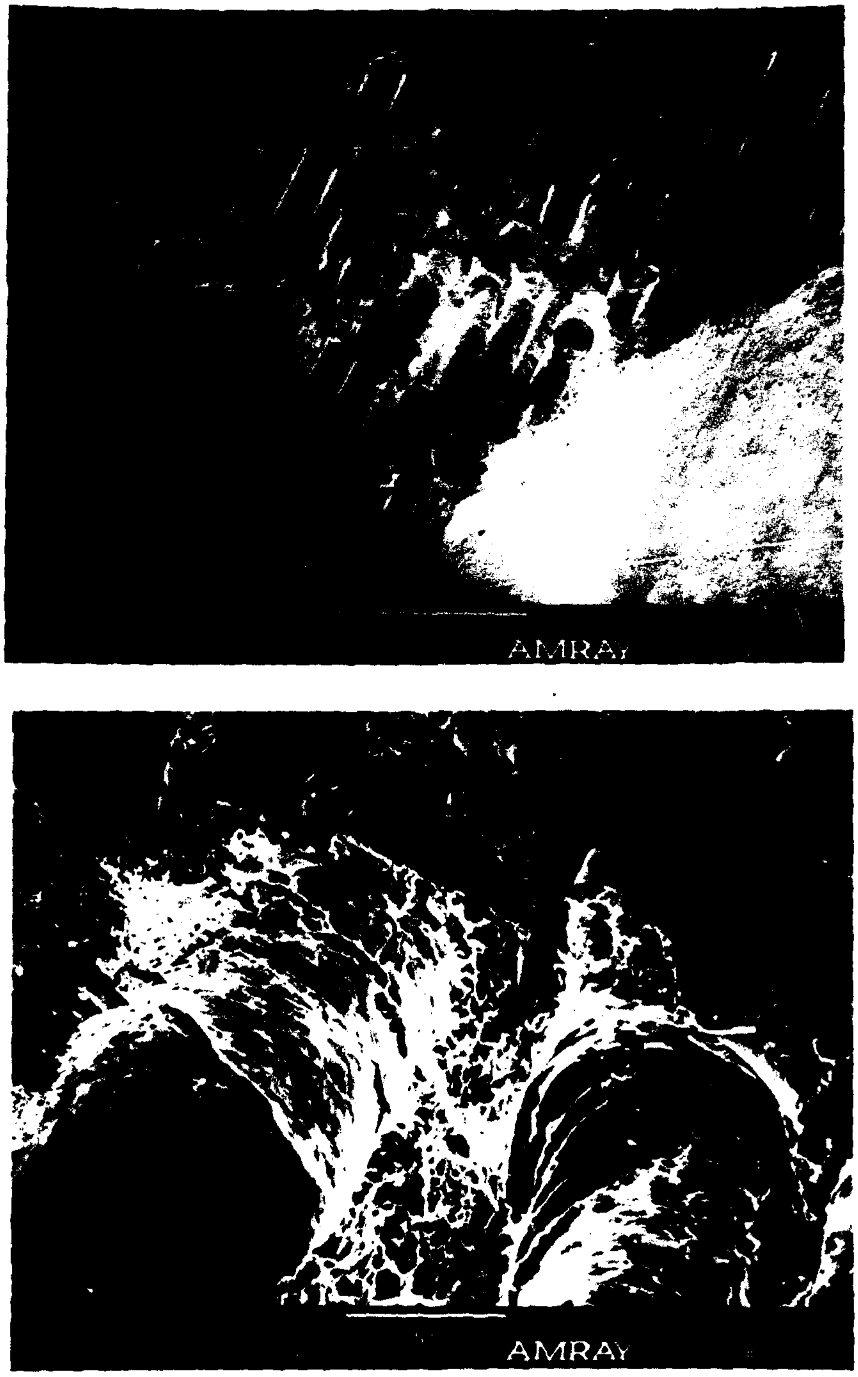

Figure 47. Fracture surface of notched $[0^\circ]_8$ specimen near hole.

Figure 35. Fracture of [15°]$_8$ specimens (top) unnotched (bottom) notched.

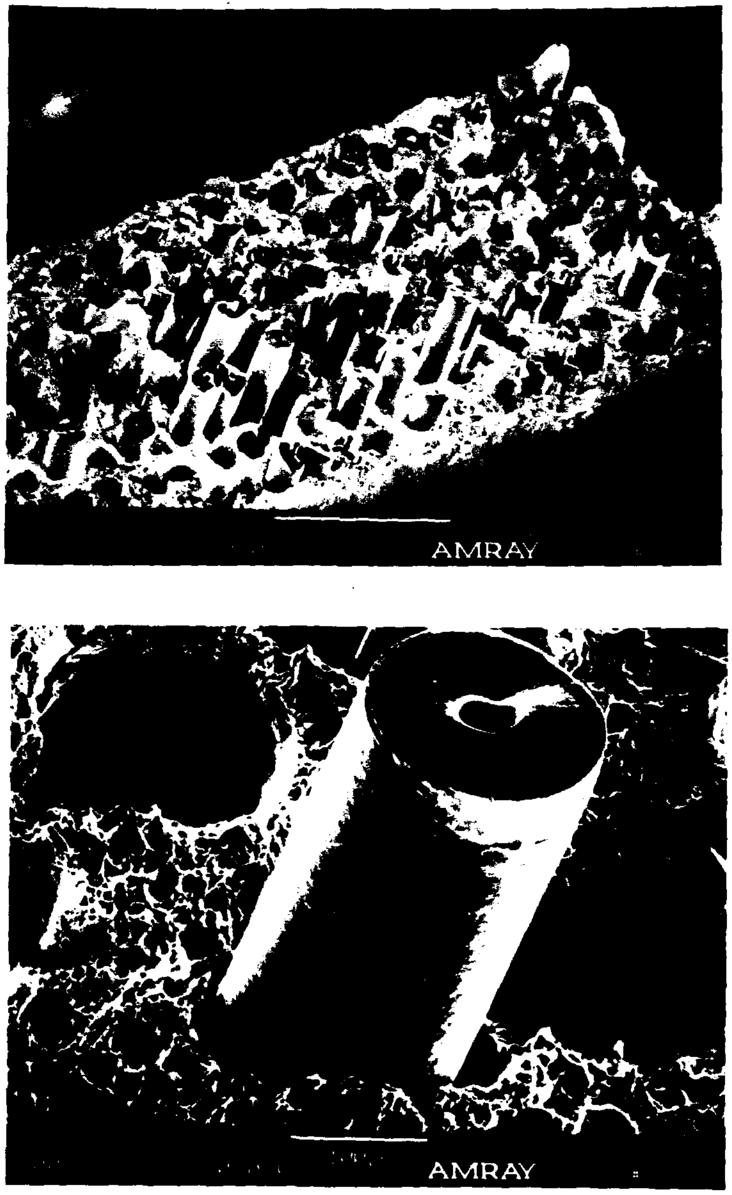

Figure 48. Fracture surface of notched [0°]$_8$ specimen away from hole.

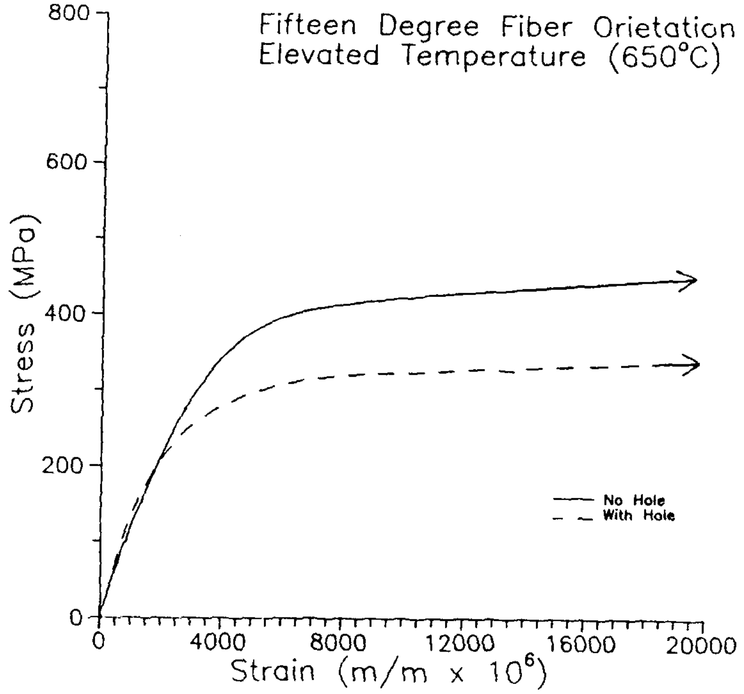

Figure 49. Stress-strain plot of $[15°]_8$ layup at 650°C.

Forty-five degree fiber orientation. The failure of the $[45°]_8$ layup is similar to the failure of the $[15°]_8$ layup. Again, the plastic strains of both specimens were large, but only the unnotched specimen's strain exceeded 20,000 μm/m. There is little increase in stress in the regions of extended deformation. See Figure 54. The stress strain plots show two distinct linear regions. The primary modulus has been reported earlier in Table 7. The secondary modulus is 20.6 GPa (calculated from the unnotched stress-strain plot). If this change in modulus is due to the failure of the fiber/matrix interface bond, then only the matrix is carrying the applied load. A macroscopic view of the notched and unnotched fractures is shown in Figure 55. Necking is clearly visible, but there is little fiber pull out. The matrix fracture followed a single column of fibers across

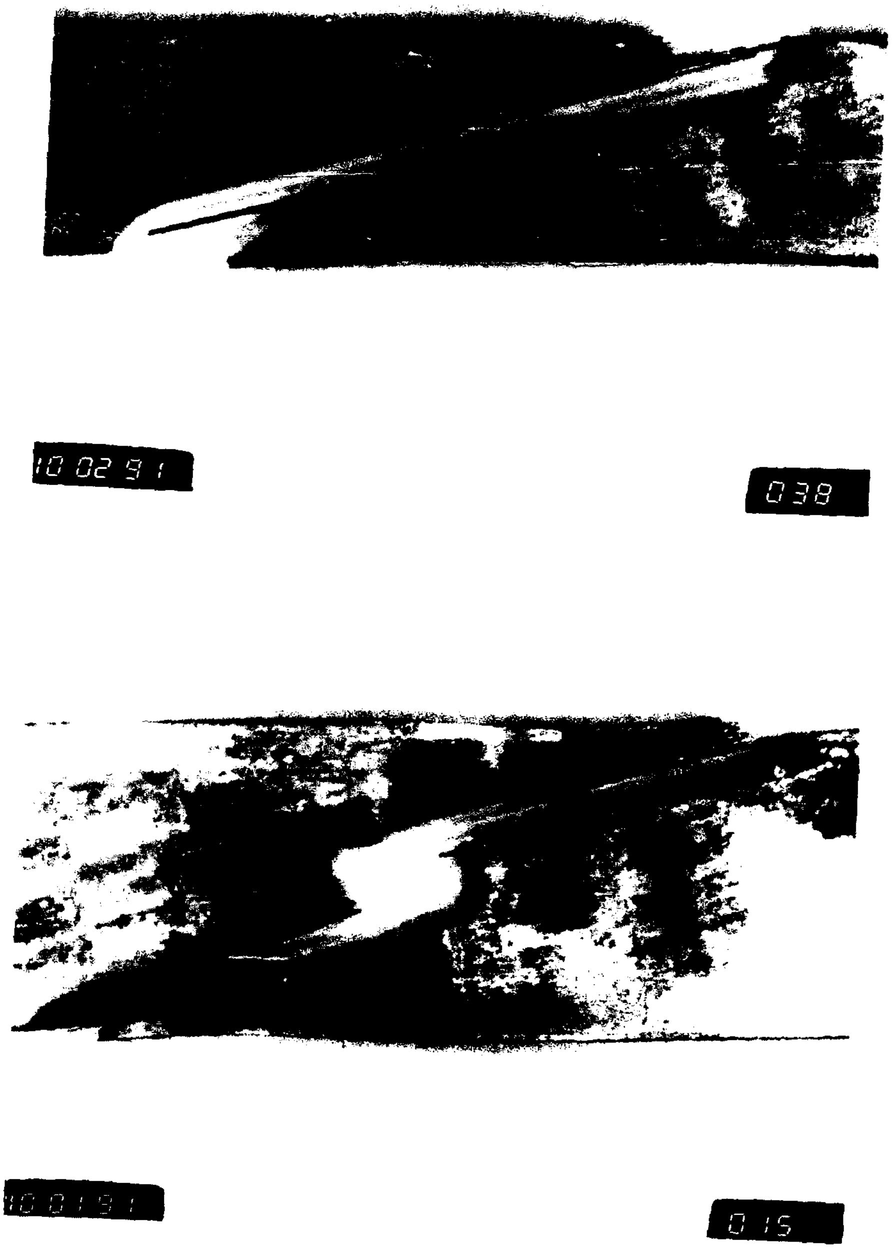

Figure 50. Fracture of $[15°]_8$ specimens (top) unnotched (bottom) notched.

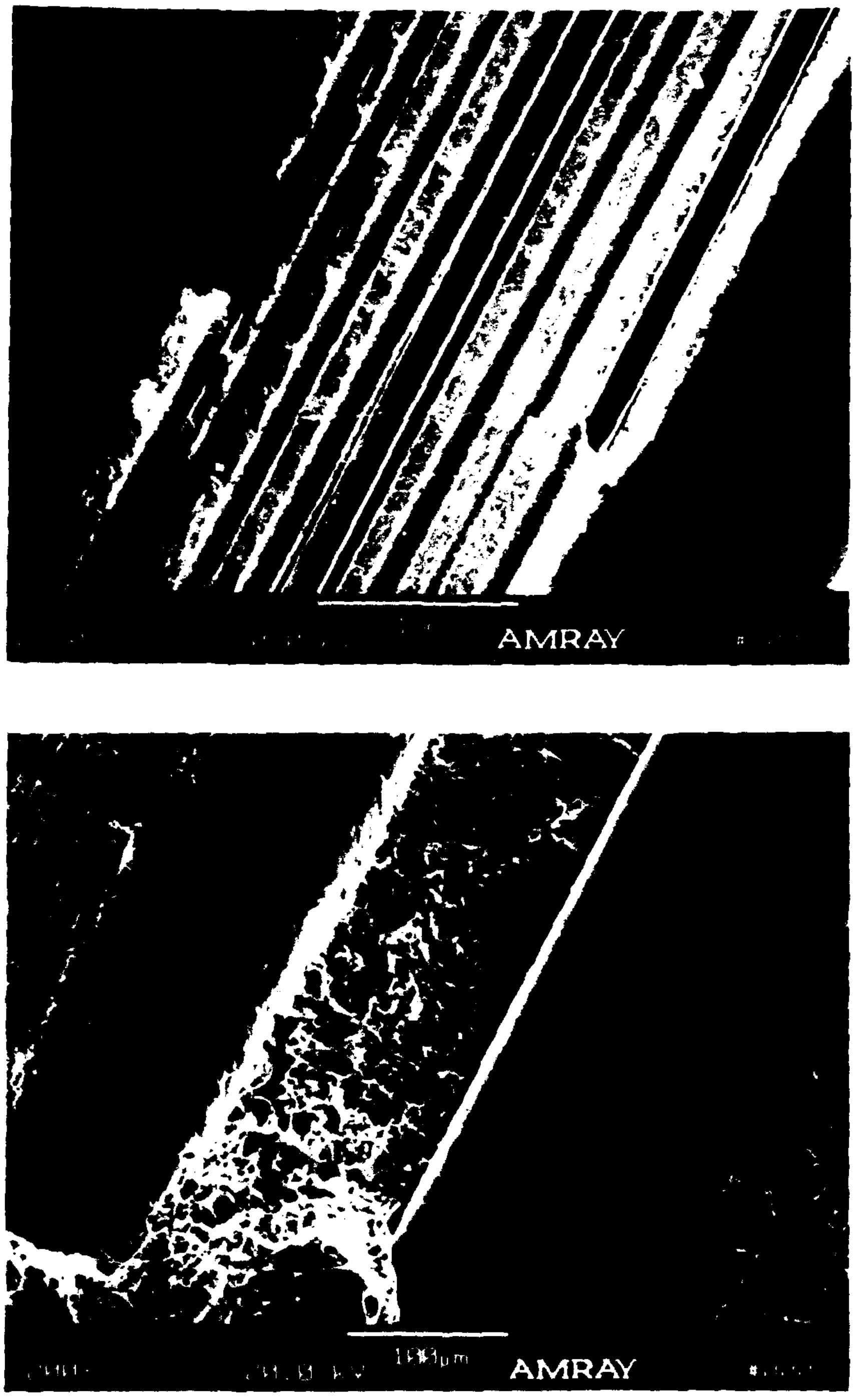

Figure 51. Fracture surface of unnotched $[15^\circ]_8$ specimen.

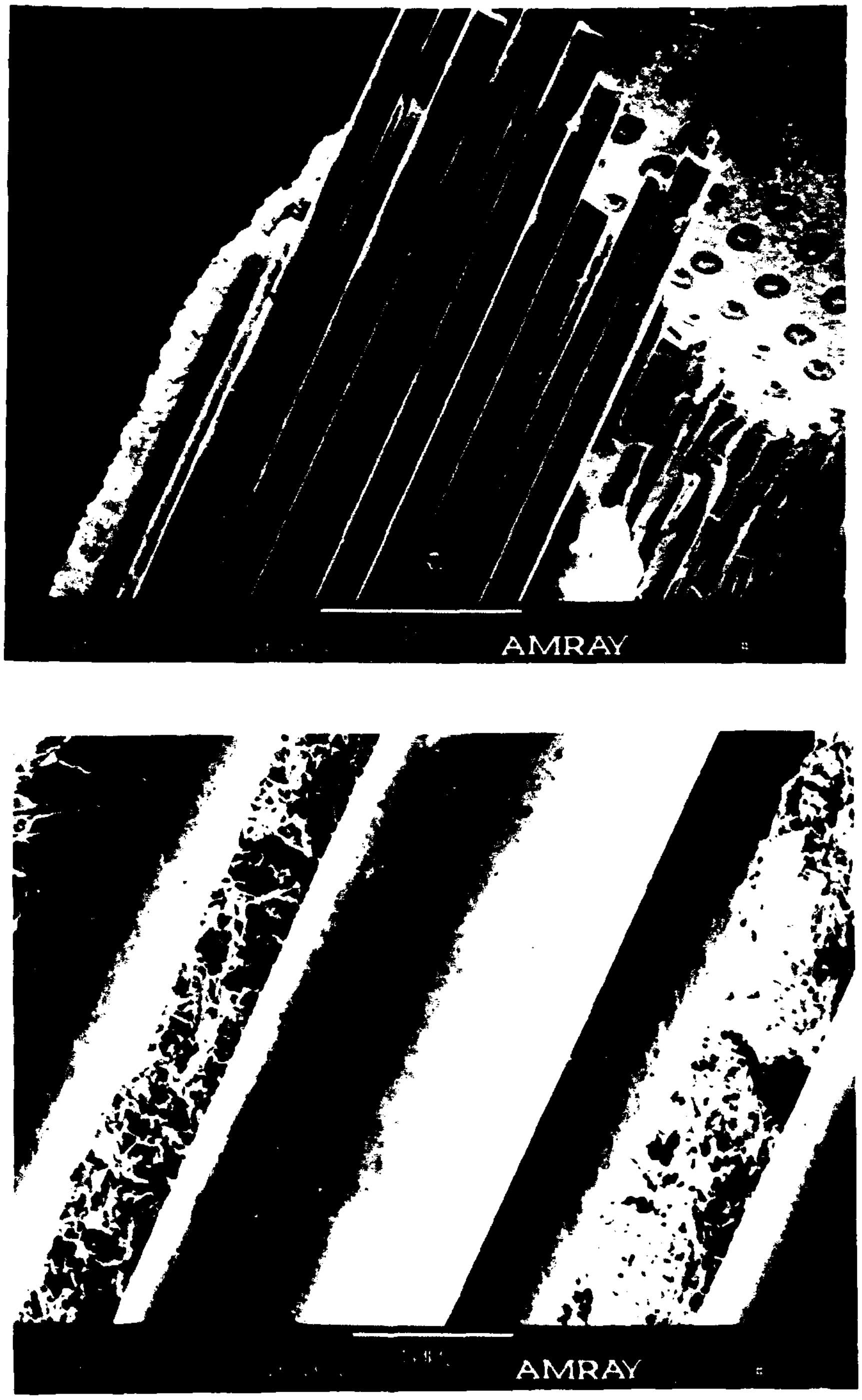

Figure 52. Fracture surface of notched $[15°]_8$ specimen near hole.

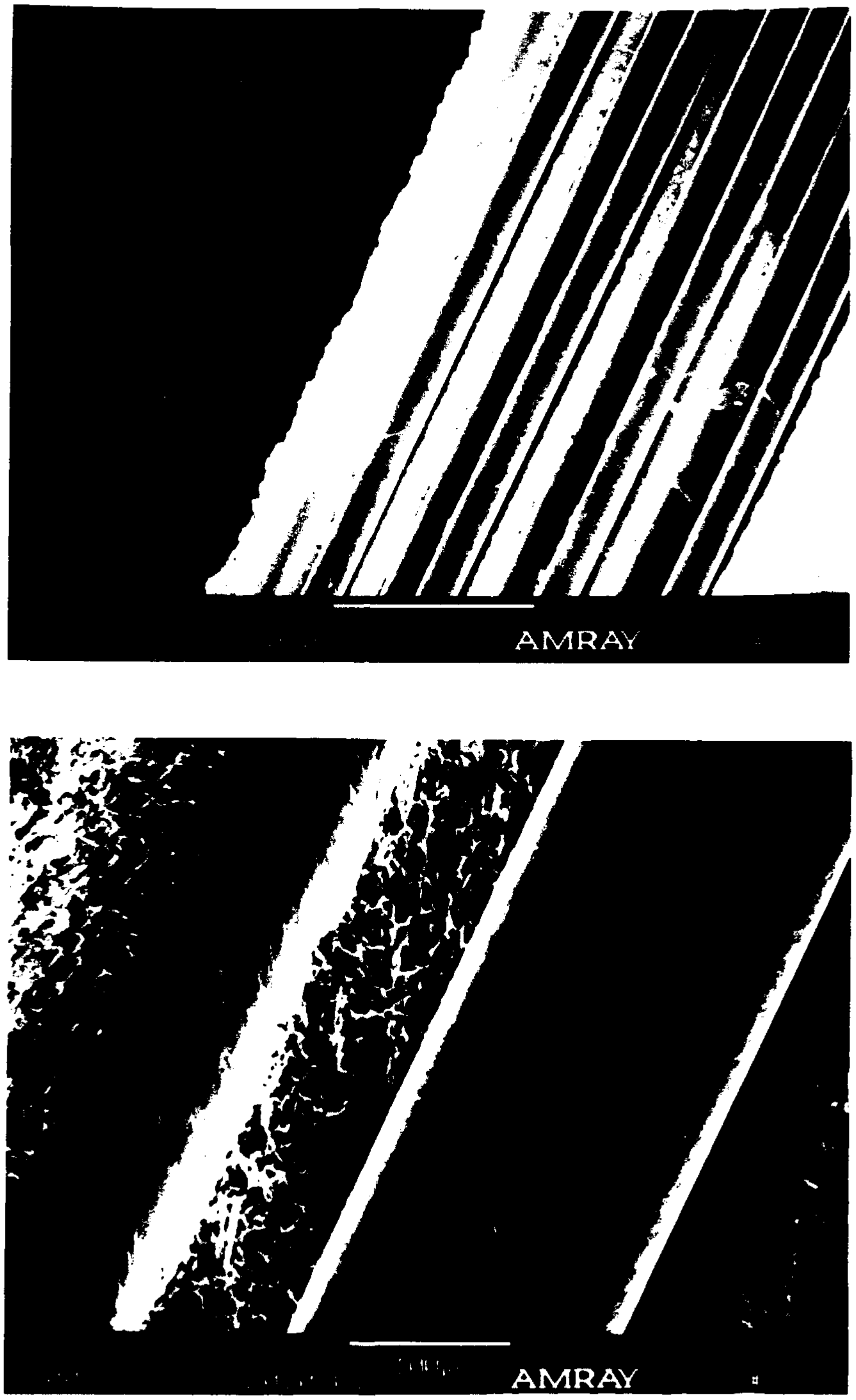

Figure 53. Fracture surface of notched [15°]$_8$ specimen away from hole.

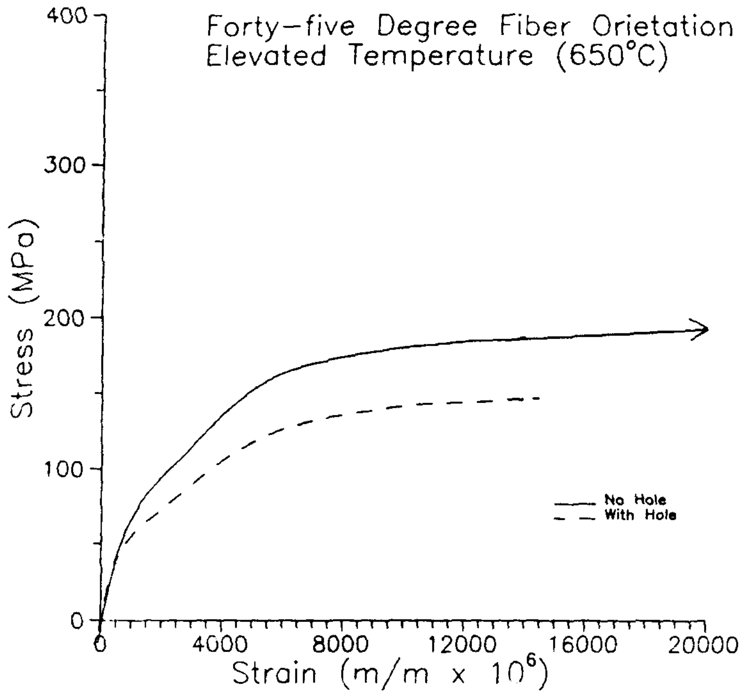

Figure 54. Stress-strain plot of $[45°]_8$ layup of 650°C.

the width of the specimen except at the edge where some delamination occurred. The magnified views of the fracture surfaces, Figures 56, 57, and 58, show extensive separation of the fibers and matrix at the fracture and ductile fracture of the matrix. As with the $[15°]_8$ specimens, the fiber surfaces are clean and undamaged indicating a weak fiber/matrix interface bond. The fiber channels of the $[45°]_8$ layup are less cracked than those of the $[15°]_8$ layup, but there was less plastic deformation of the $[45°]_8$ specimens prior to failure. The notched and unnotched fracture surfaces are the same except for the evidence of greater plastic deformation of the unnotched specimen.

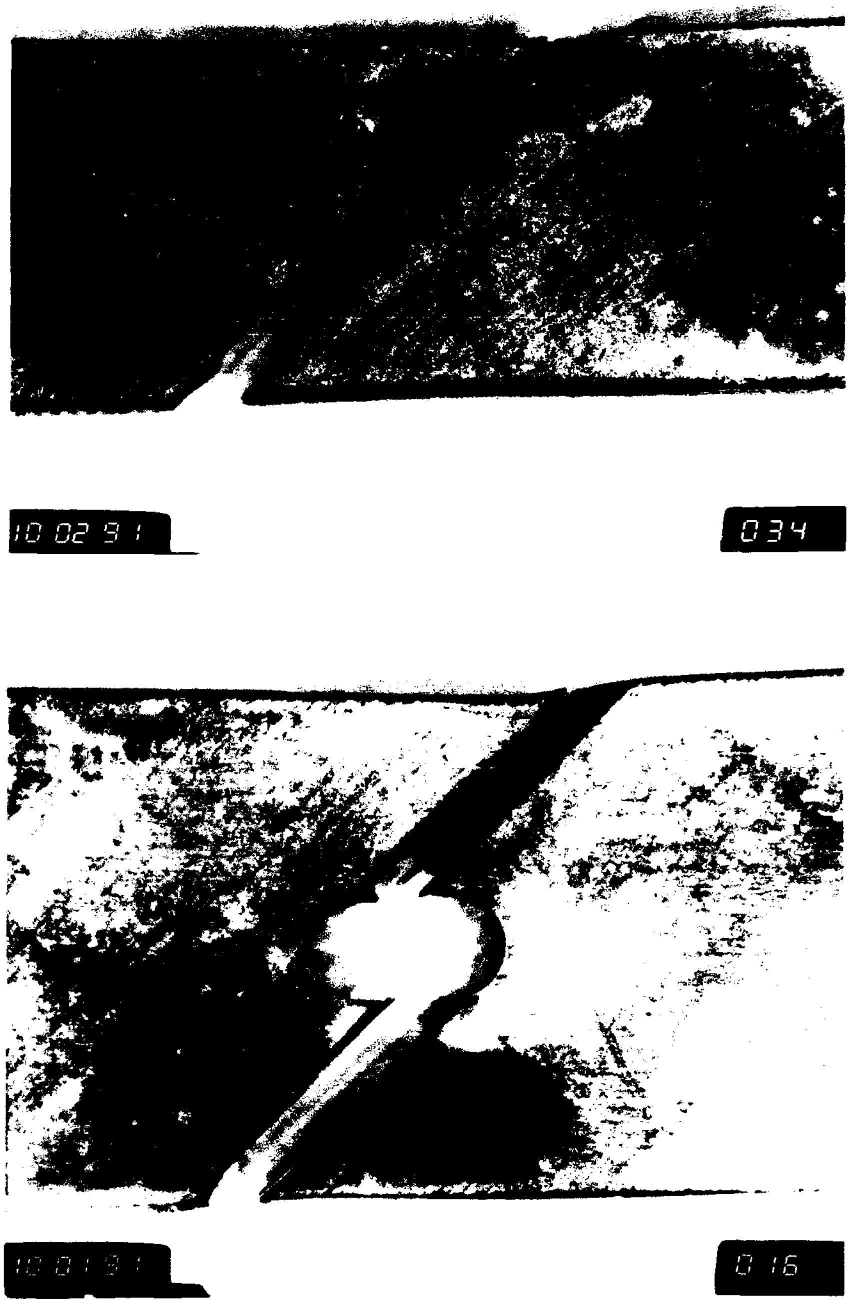

Figure 55. Fracture of $[45°]_8$ specimens (top) unnotched (bottom) notched.

Figure 43. Fracture surface of notched $[45^\circ]_8$ specimen away from hole.

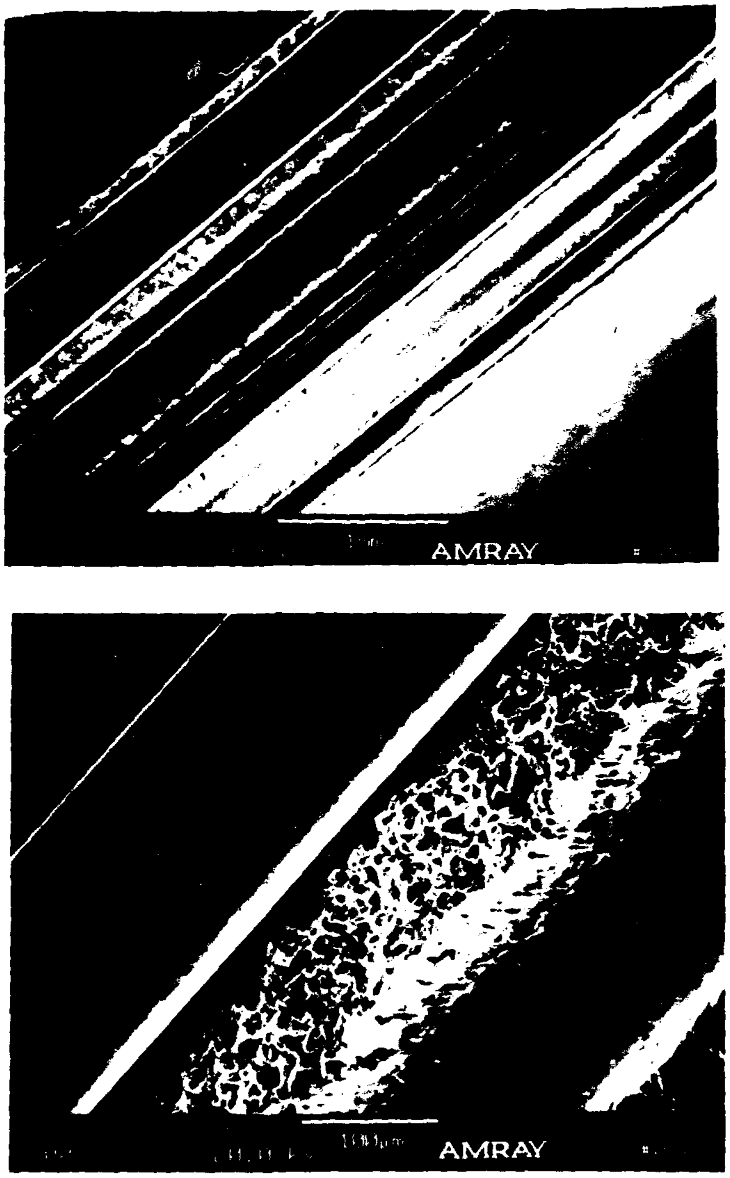

Figure 56. Fracture surface of unnotched $[45^\circ]_8$ specimen.

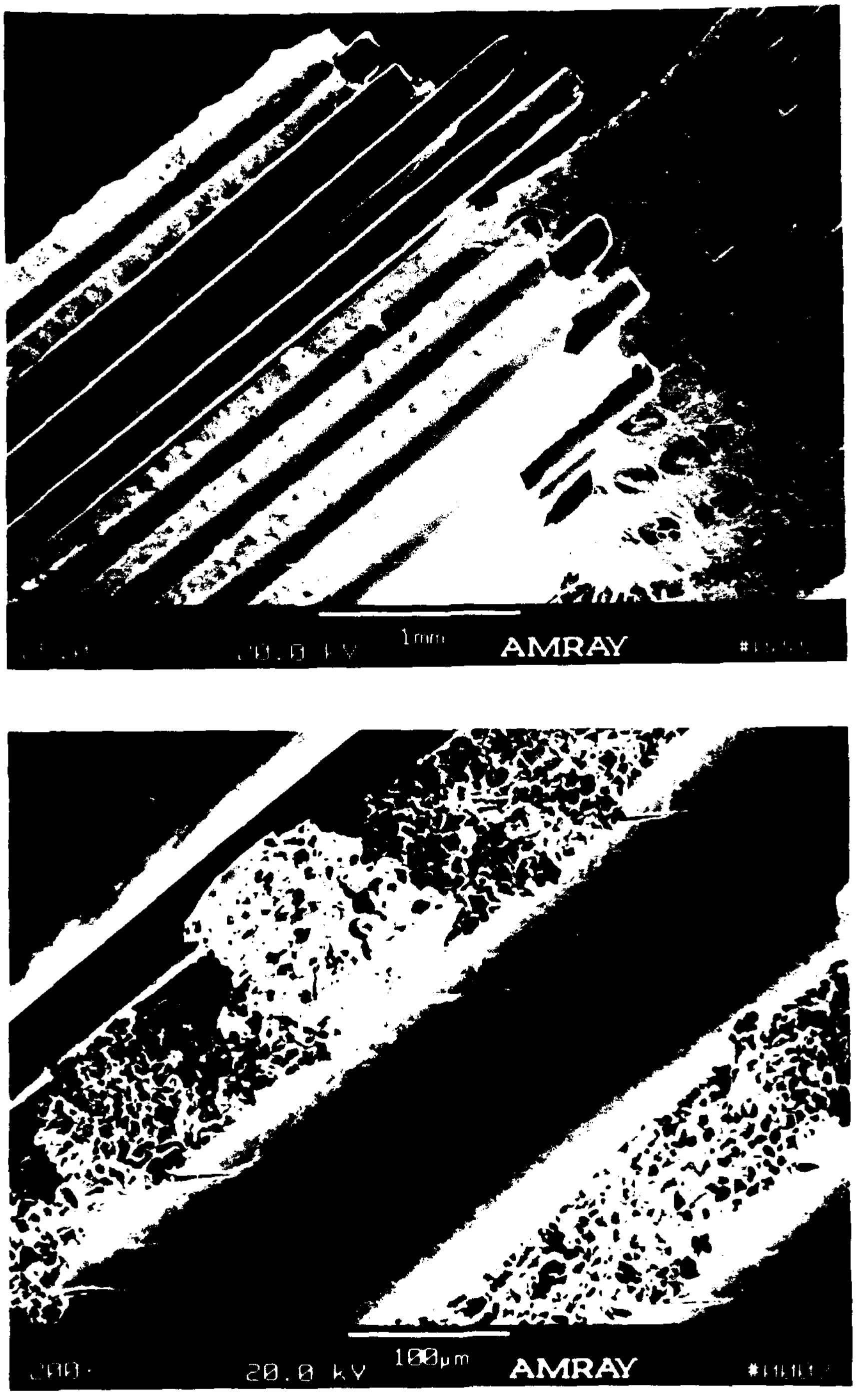

Figure 57. Fracture surface of notched [45°]$_8$ specimen near hole.

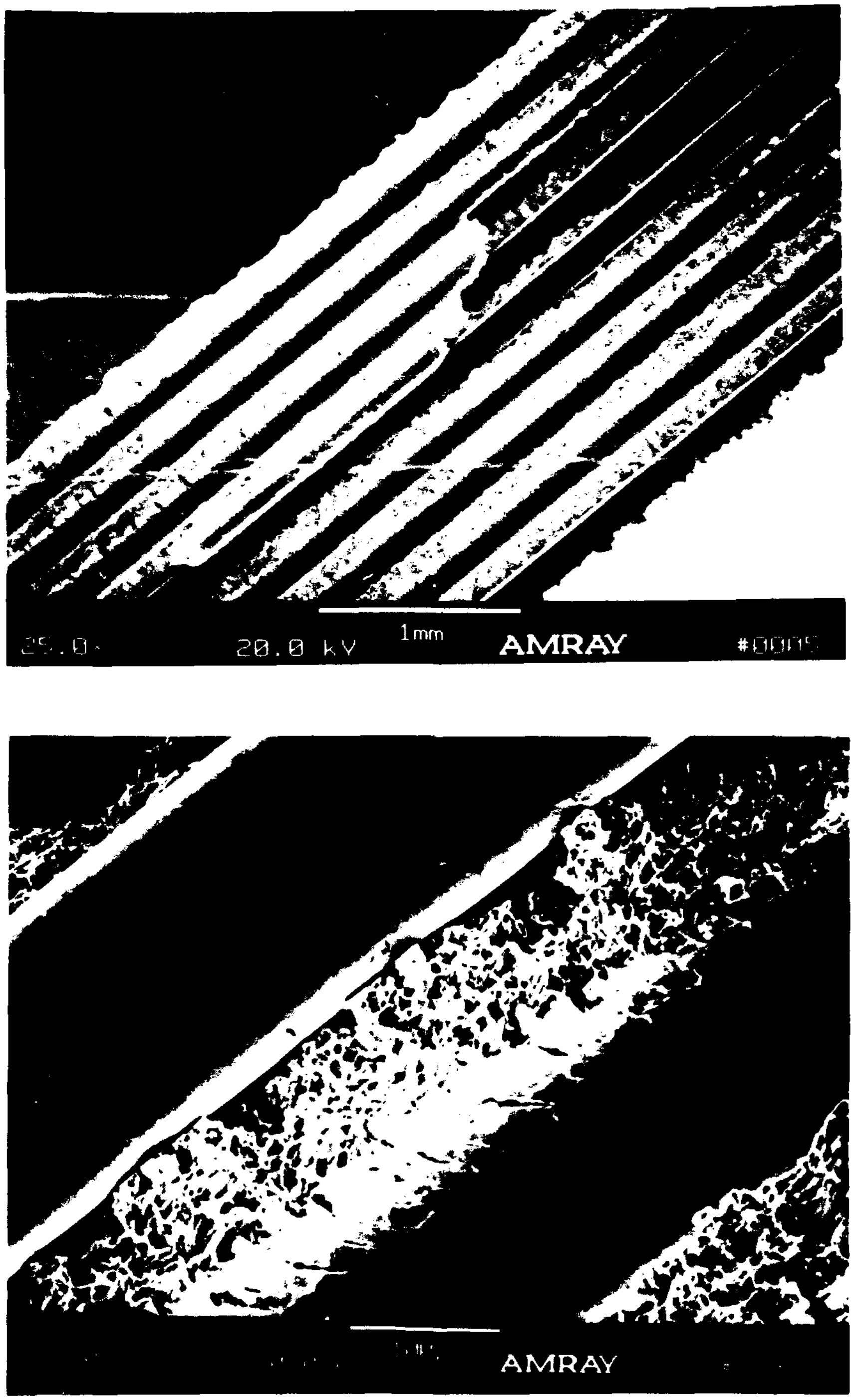

Figure 58. Fracture surface of notched $[45^\circ]_8$ specimen away from hole.

VI. Conclusion and Recommendations

This study investigated the ultimate tensile strengths of $[0°]_8$, $[15°]_8$, $[45°]_8$ layups of SCS-6/Ti-24Al-11Nb metal matrix composite containing a circular hole. Uniaxial tensile tests were conducted at room temperature (25°) and elevated temperature (650°C) with each fiber orientation. Unnotched specimens were also tested for comparison. In addition to finding the tensile strength of different composite layups, this study attempted to find prefailure damage in the notched specimens through visual observation and radiography, and it attempted to describe the failure mechanism of the material.

The experimentally determined Young's moduli, E_x, of the fiber orientations tested in this study were close to the rule of mixtures predicted properties, and they were very close to the moduli predicted from the Allison experimental data. The composite was consolidated well, and Textron has good quality control of its manufacturing process. The simplified Tsai-Wu failure theory predictions of ultimate tensile strength closely match the failure strengths found experimentally for this study. Determining the actual value of the coefficient F_{12} through biaxial loading failure tests may reduce the small differences between predicted and actual values even more.

A finite element model was developed as an aid in predicting stress concentration factors and high stress areas where damage might begin. Limitations of MSC/NASTRAN version 66A permitted only linear analysis of the orthtropic material examined in this investigation. No specific stresses parallel or perpendicular to the fiber direction, consistent among the various fiber orientations of the model and consistent with a given layup's yield strength, could be found to indicate the strength of the fiber/matrix interface bond.

The SCS-6/Ti-24Al-11Nb composite is not notch sensitive at the hole diameter tested. Stress concentration theory, even when modified for orthotropic materials, does not seem to apply to the small diameter hole tested for this investigation. Maximum stress or maximum strain criteria can be used to find notched tensile strength. Testing a variety of larger hole sizes is recommended to determine the true extent of the composite's notch insensitivity.

Very little damage can be detected in the SCS-6/Ti-24Al-11Nb prior to its failure at room temperature. Radiography discovered no internal damage prior to failure. Damage such as fiber/matrix separation and delamination developing at elevated temperature might be detectable through some form of nondestructive inspection, but high temperature NDI could not be applied during this study.

The failure surfaces of the tested composite layups can be divided into two groups by temperature. Within each thermal group, the off-axis specimens show similarities not found in the specimens loaded parallel to the fibers. In general, the room temperature fracture surfaces display brittle fracture of the matrix with little fiber pull out and a slight amount of necking. The elevated temperature fracture surfaces, on the other hand, display a ductile fracture of the matrix, with extensive fiber pull out, fiber matrix separation, and obvious necking. At both temperatures, the $[0°]_8$ specimens' fracture surface is perpendicular to the fibers, while the $[15°]_8$ and $[45°]_8$ specimens' fracture surface is parallel to the fibers. Future studies could investigate the strength of the fiber/matrix interface bond and compare the experimental results to those predicted by available models.

Appendix A: Stress-strain plots

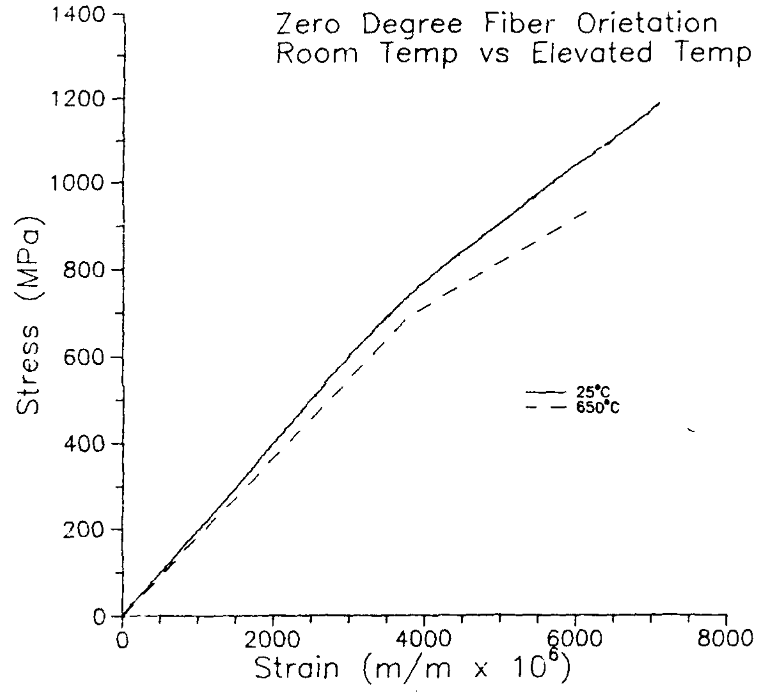

Figure A1. Stress-strain plot, unnotched $[0°]_8$ specimen.

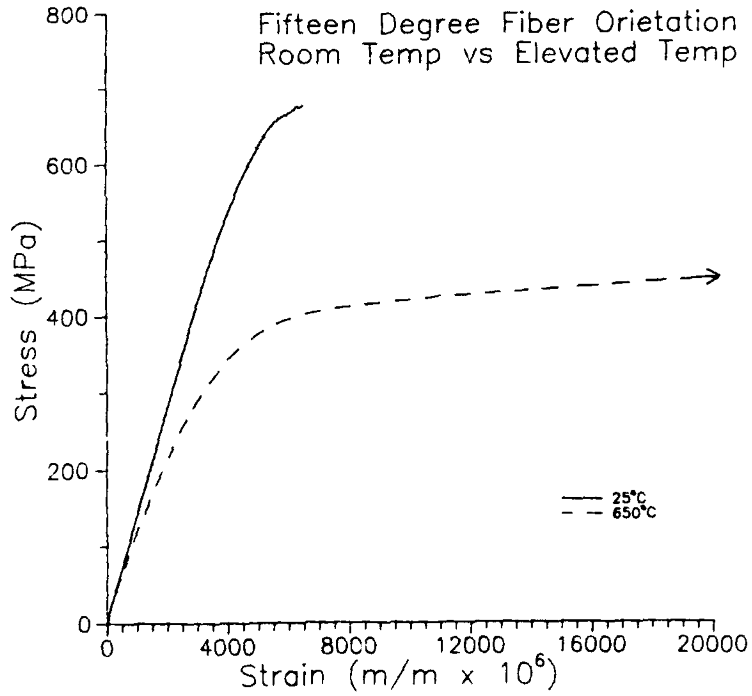

Figure A2. Stress-strain plot, unnotched $[15°]_8$ specimen.

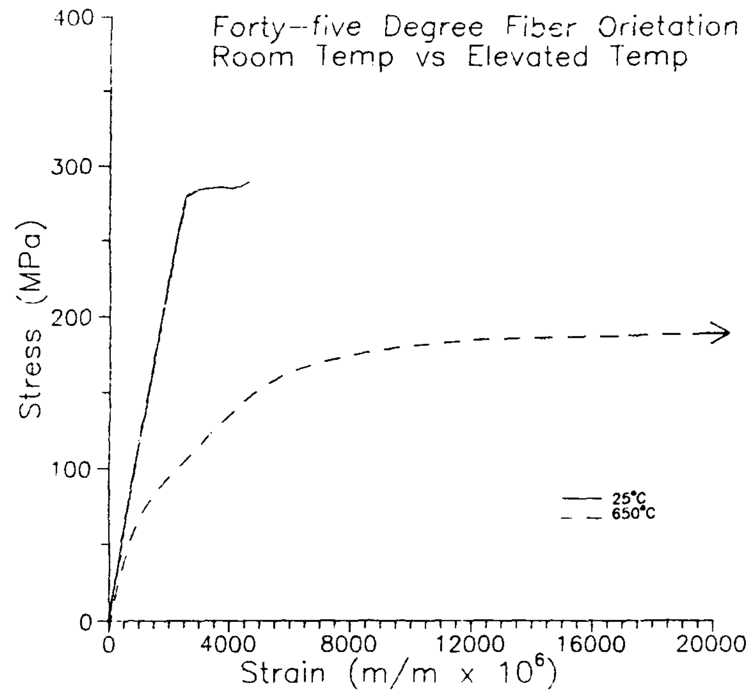

Figure A3. Stress-strain plot, unnotched $[45°]_8$ specimen.

Appendix B: Finite element model strain results

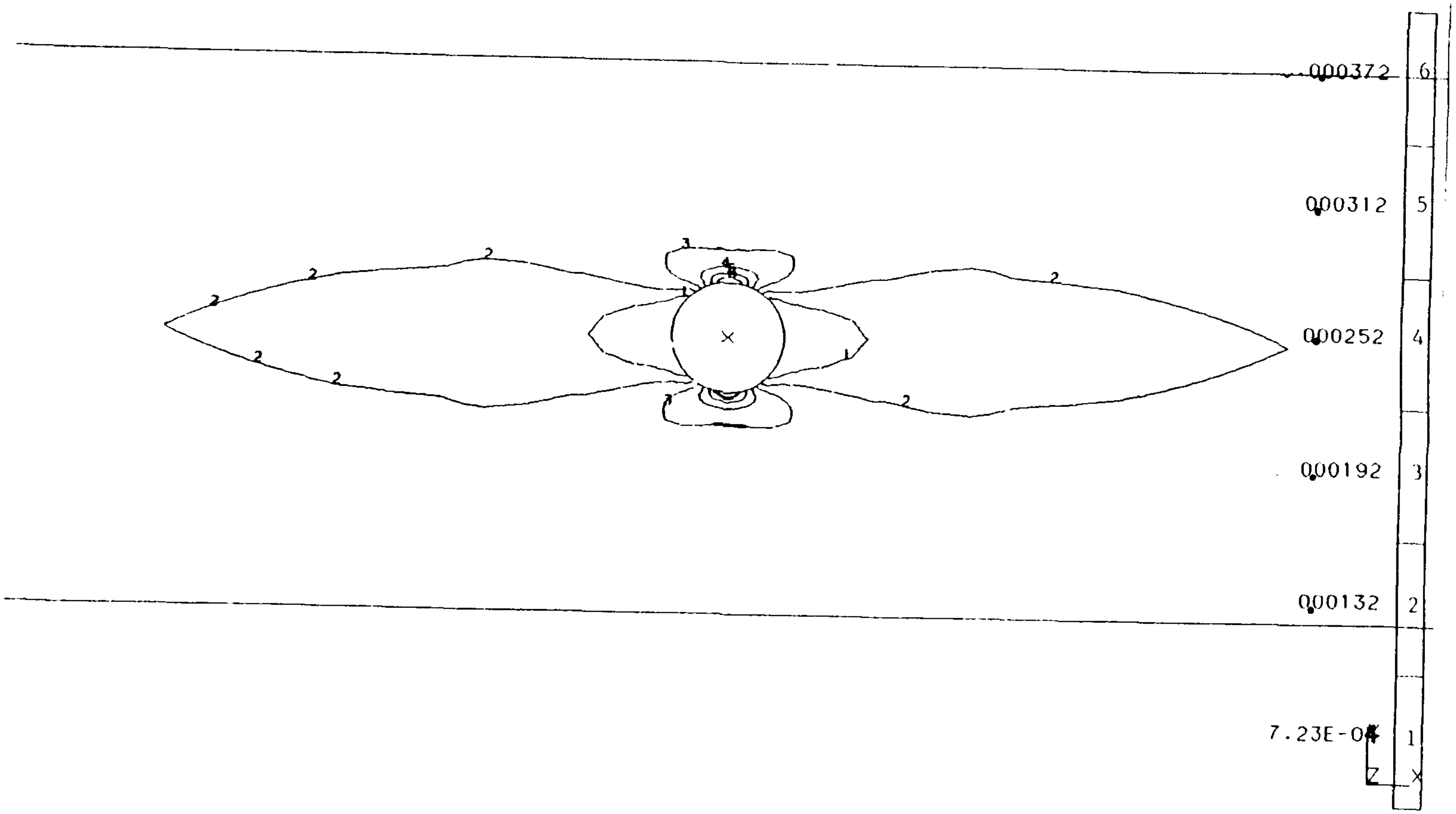

Figure B1. Strain at predicted yielding. Room temperature, $[0°]_8$ layup.

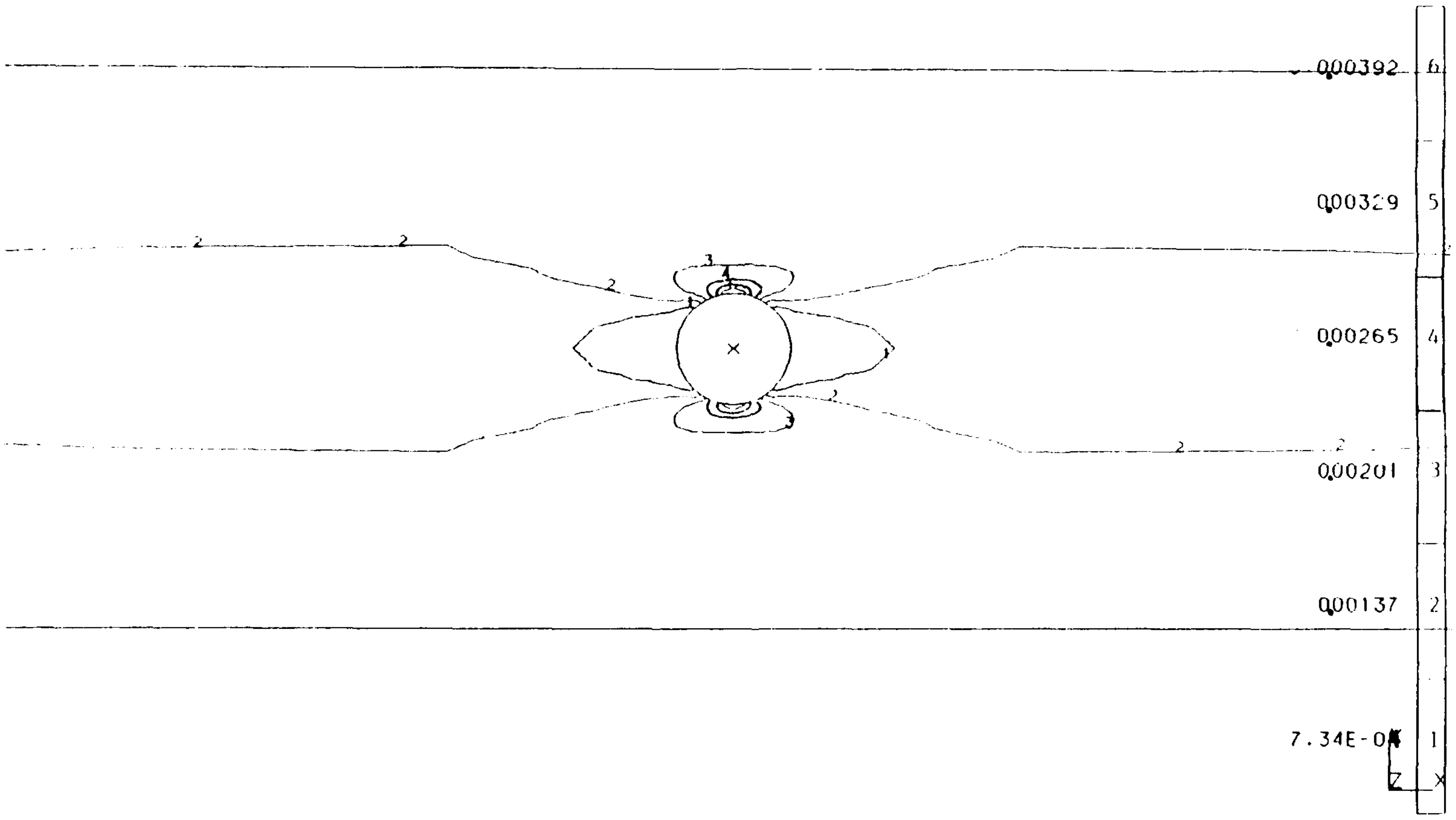

Figure B2. Strain at predicted yielding. Elevated temperature, $[0°]_8$ layup.

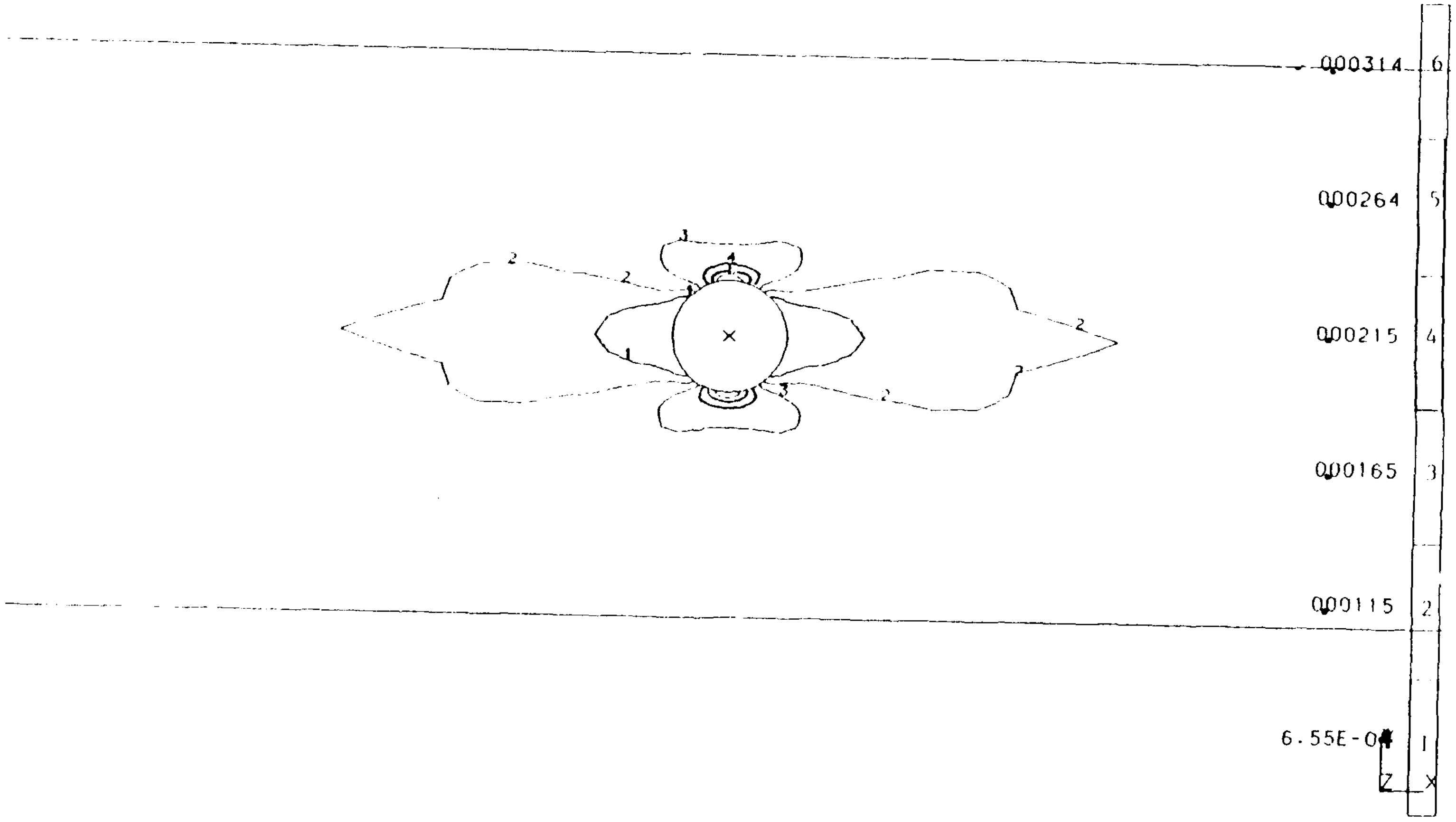

Figure B3. Strain at predicted yielding. Room temperature, $[15°]_8$ layup.

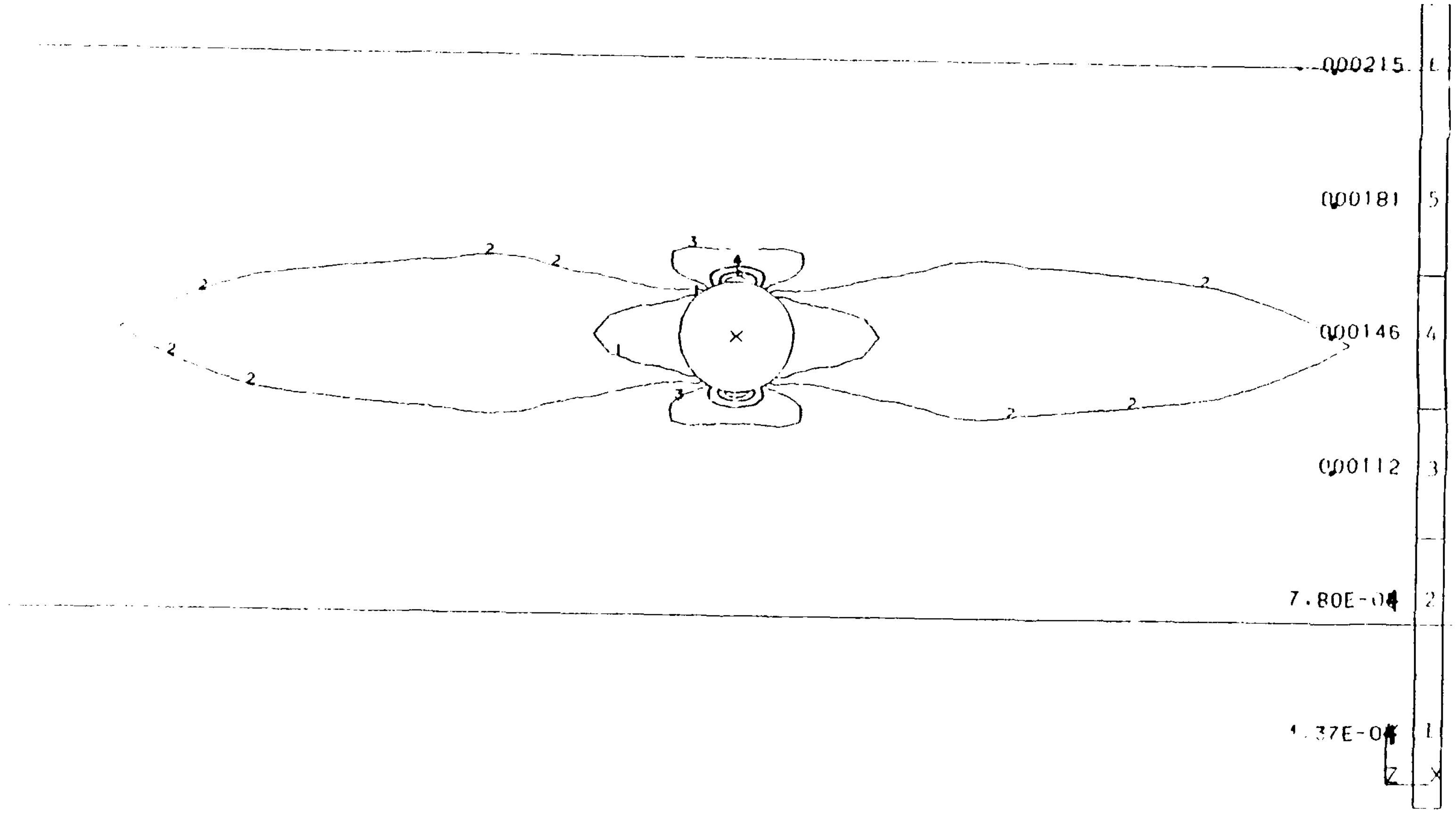

Figure B4. Strain at predicted yielding. Elevated temperature, $[15°]_8$ layup.

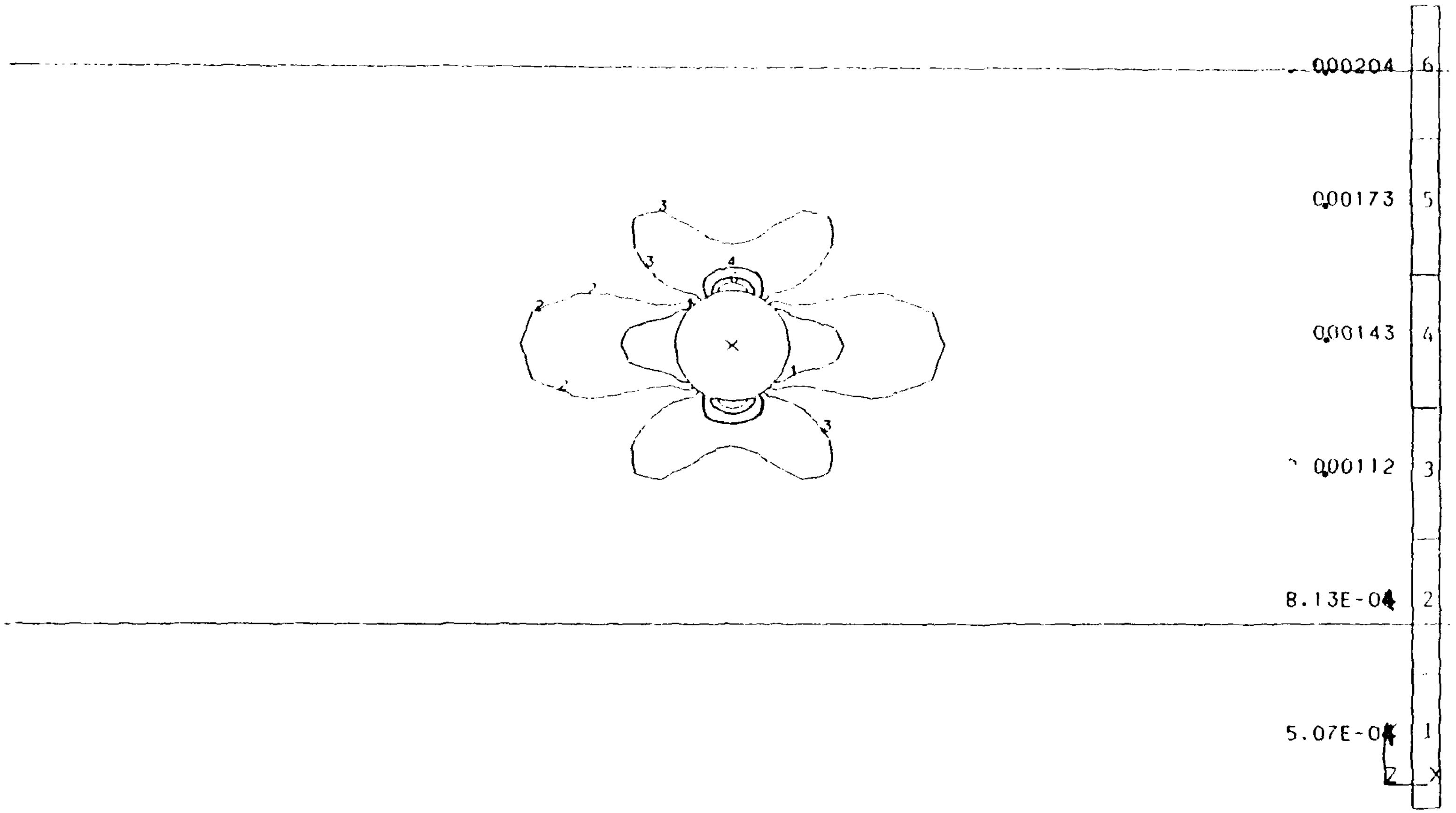

Figure B5. Strain at predicted yielding. Room temperature, $[45°]_8$ layup.

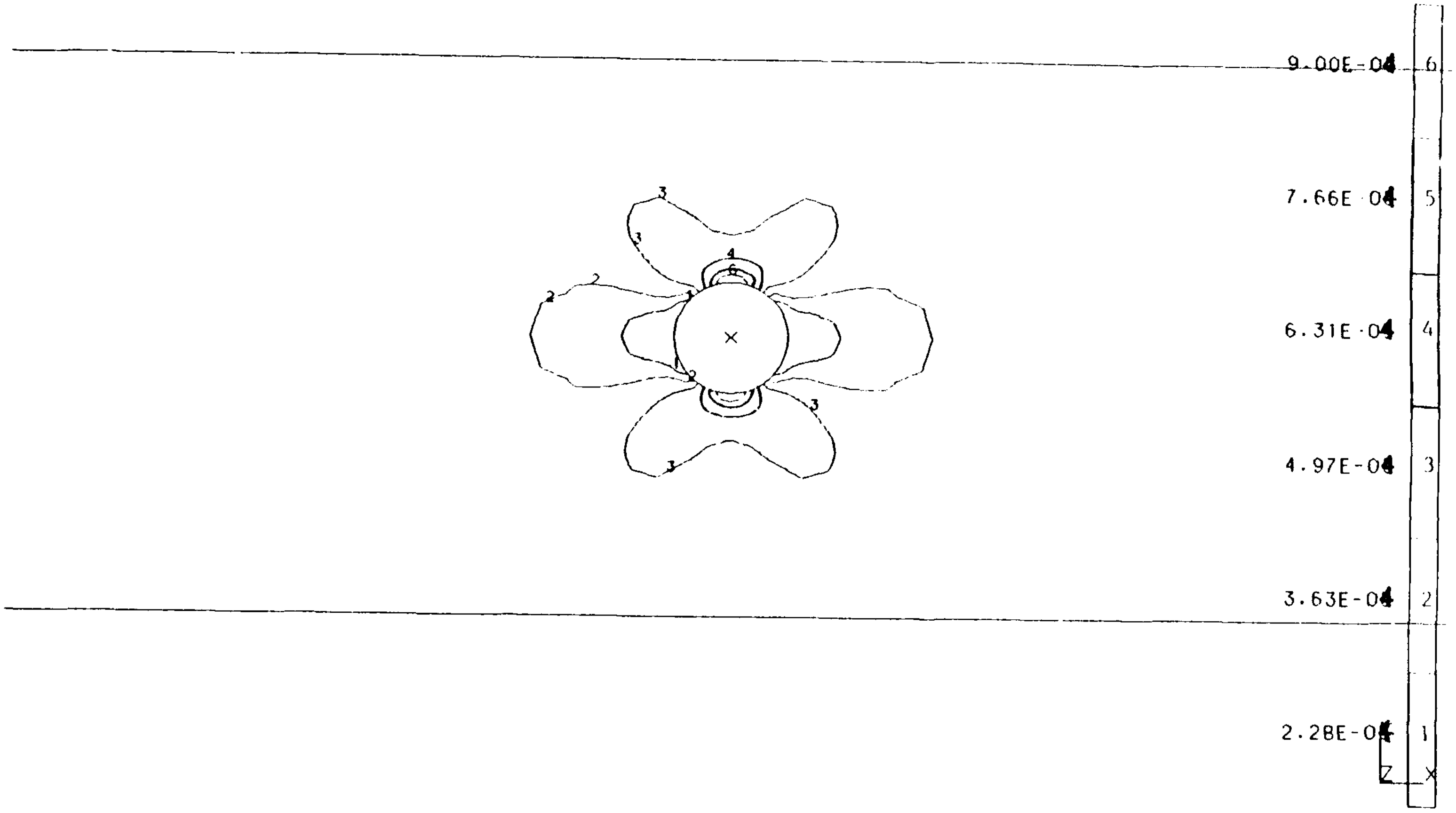

Figure B6. Strain at predicted yielding. Elevated temperature, $[45°]_8$ layup.

Appendix C: Specimen dimensions and failure loads

Specimen Layup	Test Temp	Width (mm)	Thickness (mm)	Failure Load (kN)
$[0°]_8$	25°C	12.91	2.16	25.16
	25°C	12.98	2.11	26.60
	650°C	12.78	1.99	16.96
	650°C	12.78	2.00	17.20
$[15°]_8$	25°C	12.92	2.03	13.39
	25°C	12.88	2.03	12.86
	650°C	12.78	1.99	8.31
	650°C	12.78	2.00	8.35
$[45°]_8$	25°C	12.75	2.01	6.25
	25°C	12.80	2.01	6.01
	650°C	12.78	1.99	3.66
	650°C	12.78	2.00	3.59

Table C1. Notched specimen dimensions and failure loads.

Specimen Layup	Test Temp	Width (mm)	Thickness (mm)	Failure Load (kN)
$[0^\circ]_8$	25°C	5.60	1.98	13.14
	650°C	6.36	2.03	11.98
$[15^\circ]_8$	25°C	6.33	2.04	7.92
	25°C	6.36	2.01	8.68
	650°C	6.35	2.01	Failed Test
	650°C	6.33	2.03	6.91
$[45^\circ]_8$	25°C	6.35	2.03	3.84
	25°C	6.37	2.00	3.68
	650°C	6.33	2.02	2.57
	650°C	6.35	2.02	2.67

Table C2. Unnotched specimen dimensions and failure loads.

Bibliography

1. Bartolotta, P.A., and Brindley, P.K., High Temperature Fatigue Behavior of a SCS-6/Ti-24Al-11Nb Composite, NASA TM-103157, April 1990.

2. Coker, D., FDMAT computer program material data base, Materials Directorate, Wright Laboratories, Wright-Patterson AFB, OH, April 1991.

3. Dally, J.W., and Riley, W.F., Experimental Stress Analysis, McGraw-Hill Book Company, 1978.

4. Gambone, M.L. Fatigue and Fracture of Titanium Aluminides, Volume I, Technical report no. WRDC-TR-89-4145, Wright-Patterson AFB, OH February 1990.

5. Gambone, M.L., Fatigue and Fracture of Titanium Aluminides, Volume II, Technical report no. WRDC-TR-89-4145, Wright-Patterson AFB, OH, Febrary 1990.

6. General Electric staff, Titanium Aluminide Composites, Interim Technical Report No. 4, NASP Contractor Report 1112, January 1991.

7. Greszczuk, L.B., "Stress Concentrations and Failure Criteria for Orthotropic and Anisotropic Plates with Circular Openings," Composite Materials: Testing and Design (Second Conference), ASTM STP 497, 1972.

8. Johnson, S., Experimental and Analytical Investigation of the Fracture Processes of Boron/Aluminum Laminates Containing Notches, NASA Technical Paper 2187, 1983.

9. Johnson, W.S., Lubowinski, S.J., and Highsmith, A.L., "Mechanical Characterization of Unnotched SCS-6/Ti-15-3 Metal Matrix Composites at Room Temperature," Thermal and Mechanical Behavior of Metal Matrix and Ceramic Matrix Composites, ASTM STP 1080, 1990.

10. Jones, R.M., Mechanics of Composite Materials, Hemisphere Publishing Corporation, 1975.

11. Kortyna, B.R., and Ashbaugh, N.E., "Fatigue Characteristics of a Titanium Aluminide Composite," Titanium Aluminide Composites, Technical report no. WL-TR-91-4020, February 1991.

12. Larson, J.M., and others, "Titanium Aluminides fo Aerospace Applications," Titanium Aluminide Composites, Technical report no. WWL-TR-91-4020, Wright-Patterson AFB, OH, February 1991.

13. MSC/NASTRAN, Demonstration Problem Manual, MacNeil-Schwendler Corporation, 1985.

14. Naik, R.A., and Johnson, .S., Observations of Fatigue Crack Initiation and Damage Growth in Notched Titanium Matrix Composites, paper presented at the ASTM Third Symposium on Composite Materials: Fatigue and Fracture, November 1989.

15. Peterson, R.E., Stress Concentration Factors, John Wiley and Sons, 1974.

16. Russ, S.M., and Nicholas, T., "Thermal and Mechanical Fatigue of Titanium Aluminide Metal Matrix Composite," Titanium Aluminide Composites, Technical report no. WL-TR-91-4020, February 1991.

17. Sova, J.A., Tensile Stress-Strain Behavior of Boron/Aluminum Laminates, NASA Technical Paper 1117, 1978.

18. Tan, S.C., "Finite Width Correction Factors for Anisotropic Plates Containing a Central Opening," Journal of Composite Materials, Vol. 22, November 1988.

19. Tan, S.C., "Laminated Composites Containing an Elliptical Opening," Journal of Composite Materials, Vol. 21, October 1987.

20. Whitney, J.M., and Nuismer, R.J., "Stress Fracture Criteria for Laminated Composites Containing Stress Concentrations, Journal of Composite Materials, Vol. 8, July 1974.